Microfluidic Approaches for Investigating Aggregated Forms of Disease-Related Proteins

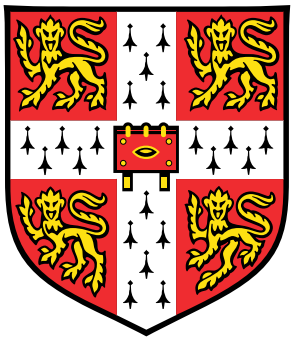

Itzel Condado Morales

Department of Chemistry

University of Cambridge

This dissertation is submitted for the degree of

Doctor of Philosophy

St John's College September 2018

I would like to dedicate this thesis to the two women that have inspired and encouraged me throughout my life: my mother and my granny. Thank you for your support, hard work, and specially your love. All that I am, or hope to be, I owe to you.

Quiero dedicar esta tesis a las dos mujeres que me han inspirado e impulsado toda la vida: mi madre y mi abuelita. Gracias por su apoyo, esfuerzo, y especialmente por su amor. Todo lo que soy, o espero ser, se lo debo a ustedes.

Declaration

I hereby declare that, except where specific reference is made to the work of others, the contents of this dissertation are original and have not been submitted, in whole or in part, for consideration for any other degree or qualification in this, or any other university. This dissertation is my own work and contains nothing which is the outcome of work done in collaboration with others, except as specified in the text and acknowledgements. This dissertation contains fewer than 60,000 words including appendices, bibliography, footnotes, tables and equations.

Itzel Condado Morales
September 2018

Acknowledgements

I would like to thank Professor Tuomas Knowles for his invaluable guidance and insightful discussions, and for giving me this opportunity to participate in such exciting work. I would also like to thank Dr. Thomas Müller, who has been an amazing mentor and friend to me, thank you for your guidance and feedback. I must also thank Professor Chris Dobson for allowing me to work in the Centre for Misfolding Diseases. Finally, I also thank Professor Adriano Aguzzi for welcoming me in his lab.

I have collaborated with a huge amount of talented people during my PhD, and I am really grateful to Dr. Manuela Pfammatter, Dr. Simone Hornemann and Rita Moos, for the collaborative work in the prion project, and all your feedback. Catherine Xu, Sean Chia and Dr. Benedetta Maninni, for collaborating with me and allowed me to expand the applications of my project. Dr. Pavan Challa for being instructive with the optics for FRET. Dr. Christopher Taylor and Dr. Maria Andreasen, for the nice collaboration and feedback with microdroplets experiments. Sam Ness, for his advice in protein purification. Raphaël Jacquat and Quentin Peter, your coding efforts are highly appreciated for me and many others. I would also like to thank all the CMD members, especially the Knowles group, for making the lab such a nice place to work in. This piece of work would have not been possible without the financial support of CONACYT and Cambridge Trust.

I would like to thank the rigorous proofreading and feedback of Dr. Thomas Müller, Dr. Aviad Levin, Dr. Janet Kumita, Sam Ness and Tom Scheidt. Thank you all. I am also very grateful to my examiners, Dr. Francesco Aprile and Dr. Lisa Cabrita, for the valuable discussion and comments about the content of this thesis.

I could not have completed this work without the support of my family and friends in and outside Cambridge. Thank you Ana, for being there for me in my best and worst moments. Thank you Oscar, Sam, Mathias, Maya, Ula, Tom, Tadas, and many others, for our great friendship. Nelly and Jose Manuel, who have been great friends to me despite the distance. To my brother and my father for supporting me always. To Raphaël, for your emotional support over this period: thank you for being you and for making me happy, you are amazing.

Abstract

The self-assembly of soluble proteins is a common phenomenon observed in nature. It ranges from the formation of functional biomaterials, such as actin filaments and tubulin microtubules that form the cytoeskeleton, to the abnormal deposition of aberrant aggregates that lead to disease. There are nearly 50 diseases currently associated with protein misfolding and amyloid formation, among them several neurodegenerative disorders such as Alzheimer's, Parkinson's and prion diseases. Recent evidence indicates that the most toxic species are the low molecular weight oligomers formed during the onset of the aggregation process. These oligomeric species are commonly difficult to analyse due to their low abundance, transient nature and heterogeneity in their structure. In fact, prions, known to be associated with transmissible spongiform encephalopathies, have not yet been fully characterised as parts of the prion composition seem to lose infectivity through various *in vitro* purification and isolation procedures.

In nature, non-homogeneous solution conditions and molecular crowding are key factors as there might be multiple species associated with the disease. However, traditional biophysical techniques allow the study of biomolecules under ideal conditions, such as high concentrations and monodisperse size distribution. Furthermore, among the limitations of the traditional methods are the sensitivity as well as the sample preparation, which in some cases may require to chemically modify the molecule. In this thesis, I describe the development of a sensitive label-free method to enable the study of protein complexes and proteins under biologically relevant environment, such as brain homogenates, by combining immunochemistry with microfluidic strategies.

In this thesis I describe the development of Immuno Diffusional Sizing (IDS), a method that combines diffusional sizing with the sensitivity and specificity of immunoassay detection. In Chapter 3, I explain the optimisation of the devices developed to size a range of particle sizes in heterogeneous mixtures, from small protein monomers to large aggregates. IDS is a label-free method capable of sizing proteins down to the nano- and picomolar concentrations, in complex solutions. The applications of this method to monomeric and aggregated forms of disease-related proteins are described in Chapter 4.

IDS has been applied to study the Prion Protein (PrP) in its native and infectious forms. Furthermore, I studied of the proteinase resistant form (PrP^{res}) extracted from the brains of infected mice specimens. IDS was applied for studying disease-relevant species, such as intrinsically disordered proteins, e.g. α-Synuclein (aSyn) and Aβ40, and their respective oligomers. Another advantage of this method is its applicability for studies of brain aSyn from transgenic overexpressing mice (OVX). Furthermore, I explore the potential of IDS for the study of post-translational modifications (PTMs) of specific proteins, such as the ubiquitination of aSyn *in vitro*.

The efforts performed during this work to achieve TR-FRET detection on-chip are described in Chapter 5. A comparison of two commercial immunoassays was performed in order to determine the suitability for its adaptation from a platereader to a microfluidic device. The design and adaptation of an optics platform for FRET detection on-chip is also discussed.

My research on the mechanisms of the molecular chaperone αB-Crystallin (aBC) is described in Chapter 6. I investigated the aggregation process of insulin in the presence of aBC. I have used a combination of bulk techniques to study the kinetics of the systems, as well as microfluidics to generate microdroplets that allow the direct observation of rare nucleation events leading to protein aggregation.

Overall, in this work I describe the development of a novel microfluidic technique, its optimisation and application to multiple systems related to protein misfolding diseases, including prions and intrinsically disordered proteins. Purification of the sample is not necessary to study the target protein because the detection of the target protein after diffusional separation is made with a sandwich immunoassay, which allows to study disease-related proteins under native conditions in a label-free manner, which is usually difficult with traditional sizing techniques. The applications of this technology could be expanded to characterise other antigens in body fluids, like cerebrospinal fluid (CSF) of blood serum.

Table of contents

List of figures

Chapter 1

Introduction

1.1 Protein folding and misfolding

Proteins are one of the four main macromolecular constituents of cells, together with carbohydrates, lipids and nucleic acids. They are long polymer chains formed by amino acids. The long chain alone is not functional unless it acquires the correct, three-dimensional structure. The protein folding problem is the question of how these amino acid chains fold to acquire their native tertiary structure [1]. The number of possible configurations grows exponentially with chain length [2]. Nevertheless, as described by the Levinthal paradox [3], protein folding is not a random search of configurations until the protein reaches the correct one, as this path would take a long time and protein folding occurs typically in the order of 10^{-2} seconds [4]. It is thought to be rather via a restricted folding pathway, that leads to a state of minimal energy. All the possible pathways with their respective energies for a given protein, can be described in a funnel shaped energy landscape (Figure 1.1) which maps all possible conformations with their corresponding energy levels [5].

The correct protein folding is even more difficult *in vivo* due to the crowded environment in the cell, in which the macromolecule concentrations can be around 0.3-0.4 g/ml [6]. Despite this harsh conditions, the cell has its own mechanisms to prevent protein misfolding, such as chaperone activity, proteasome clearance and transcriptional/translational regulation [7]. On the other hand, these protective mechanisms may become deficient with aging, oxidative or metabolic stress, or even the presence of genetic mutations. Malfunction of the protein homeostasis can lead to diseases. Usually, the standard free energy associated with the amyloid state is comparable or even more negative than the one of the native state, as shown in Figure 1.1, but this is only true at protein concentrations above a critital value (critical concentration) and depends also on activation barriers [8].

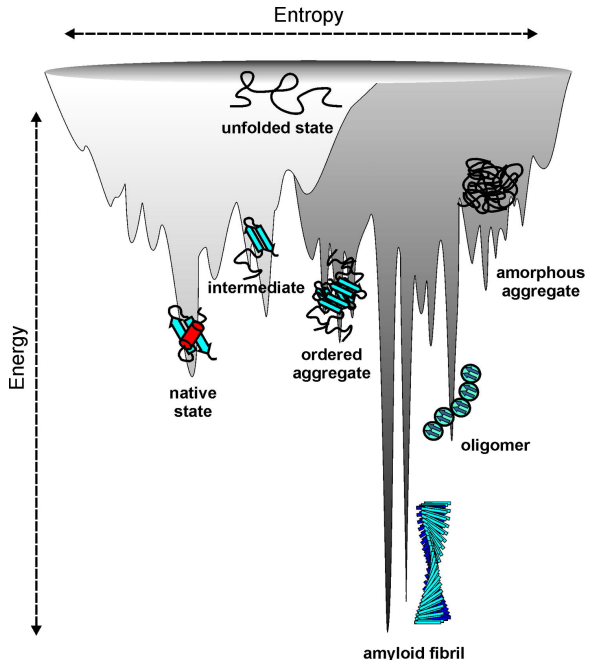

Fig. 1.1 Schematic representation of an energy landscape for protein folding and aggregation, showing the multiple states available for a polypeptide chain. The folding funnels are indicated in light gray and are caused by intramolecular interactions, while the aggregation pathways are indicated in dark gray and are determined by intermolecular protein interactions. The amyloid state might be thermodinamically more stable compared to the native state even under physiological conditions [8]. Reproduced from [5].

The maintenance of proteome homeostasis (proteostasis) are key for a healthy cellular environment. An integrated network of several hundred proteins formed mostly by molecular chaperones, the ubiquitin-proteasome system (UPS) and autophagy system, are the responsible of proteostasis [9]. The main roles of molecular chaperones include assisting the nascent polypeptide chains to fold into their native state, assisting proteins to prevent misfolding under cellular stress, aggregate dissociation and refolding of denatured proteins [10]. Chaperones are also responsible to accompany terminally misfolded proteins to their protein degradation system, composed by the UPS and autophagy driven vacuolar (lysosomal) proteolysis [11]. The degradation system is also crucial for identifying misfolded proteins which are targets of the UPS. The greatest risk factor for proteostasis capacity is ageing, which may facilitate the pathogenesis of several diseases, among them neurodegenerative disorders, type 2 diabetes, amyloidosis, cancer and vascular disease [9].

Although the self assembly of soluble proteins or peptides to insoluble fibres is often associated with disease, it is also a key process to some functioning biological systems. Examples are the formation of silk produced by spiders [12] and cytoskeleton formation as known from

actin biofilaments and tubulin microtubules. In this case, the functional aggregation process leads to the formation of biomaterials and nanostructures, a polymerisation process described as a simple nucleation and growth, like crystallisation [13]. In other cases, however, when proteins undergo unregulated aggregation, the process can lead to disease. Nowadays, nearly 50 diseases are known to be associated with aberrant protein self-assembly, which can be broadly classified into a) neurodegenerative conditions, like Alzheimer's and Parkinson's disease, b) non-neuropathic localised amyloidosis (e.g. type II diabetes and cataracts) and c) non-neuropathic systemic amyloidosis, like lysozyme amyloidosis [8, 14].

The first inherited human disease whose molecular mechanism was associated with protein misfolding was sickle cell anaemia, which is caused by a single mutation that changes a glutamic acid into a valine in the haemoglobin polypeptide chain [15]. This mutation gives rise to the formation of abnormal filaments that deform the erythrocytes and leads to sickling [16]. In 1907, Alois Alzheimer described the presence of aggregates in the post-mortem tissue of his patient, Auguste Deter [17]. Nevertheless, it was not until 1985 that the components of these plaques and tangles were characterised, and they were found to consist mostly of amyloid-beta peptide (Aβ) and hyperphosphorilated tau, respectively [18].

According to the Alzheimer's association, in 2018 around 50 million people are affected with Alzheimer's disease worldwide. The impact of the disease in society is not only economic, but also emotional, as the patient's family has to deal with their loss of cognitive function as the disease progresses [19]. Hence, the search for an effective diagnosis and treatment for Alzheimer's, and other protein misfolding disorders (PMDs) is arguably just as important as other kinds of disease such as cancer or viral infections. As increasing evidence implicates specific forms of Aβ are associated with neurotoxicity, some therapeutics aim to target the disease by depleting cerebral Aβ levels [20]. Alternatively, some others aim to slow-down the aggregation process by targeting the nucleation events and delaying the formation of cytotoxic species [21].

Parkinson's disease (PD) is the second most prevalent neurodegenerative disease just after Alzheimer's [22]. The hallmark of PD is the presence of Lewy bodies (LBs) and Lewy neurites (LNs), which are intraneuronal inclusions mainly composed of α-Synuclein (aSyn). Although the association of aSyn to PD was originally made because it is the major constituent of LBs in the PD brains, its direct role in the disease was demonstrated by genetic evidence that links several mutations in the gene encoding aSyn that can result in familial forms of PD [23]. aSyn is a largely unstructured protein in solution, like many others in the context of PMDs, which are often described as natively unfolded or intrinsically disordered proteins (IDPs) [14].

IDPs lack stable secondary and/or tertiary structures under physiologycal conditions *in vitro*. This feature enables IDPs to participate in many signaling, regulation and control roles, by binding to multiple partners [24]. Several IDPs are associated not only with PMDs but also with other types of human disease, like cancer, cardiovascular disease and diabetes. The protein conformational diseases of IDPs result from protein aggregation as well as misidentification, missignaling and nonnative folding. IDPs, such as aSyn, the Aβ peptide and tau protein are therefore the target for drugs to modulate protein-protein interactions. However, PMDs are linked to both IDPs and globular proteins, as it is the case of lysozyme and insulin, and in some cases to proteins with highly disordered regions, for example the mammalian cellular prion protein (PrP^{C}) [14].

Prion diseases or transmissible spongiform encephalopathies (TSEs) are fatal neurodegenerative disorders associated with a misfolded form (PrP^{Sc}) of the functional prion protein (PrP^{C}) [25]. Although the prevalence of TSEs is exceedingly rare compared to other neurodegenerative disorders, they represent a fascinating challenge for science, medicine and the public health system due to the fact that they are infectious, rapidly progressive, and are always fatal [26]. The detailed structure of the infectious PrP^{Sc} remains to be solved [27], mainly due to its lack of solubility and the loss of infectivity caused by the addition of denaturants used to solubilise the aggregates [28]. This has made the study of prion replication ($PrP^{C} \rightarrow PrP^{Sc}$) quite challenging. The lack of detailed structure of PrP^{Sc} and a precise understanding of prion replication has limited the development of both, a very sensitive diagnostic procedure for TSEs, and an effective therapeutic approach which reliably overcomes the disease [29].

Another subtype of PMDs are the so-called amyloidosis. Some examples of these human diseases are the systemic amyloidosis associated to lysozyme and injection-localised amyloidosis induced by the subcutaneous administration of insulin. Unlike neurodegenerative disorders associated to protein misfolding where the exact cause of the disease is poorly understood, amyloidosis is a disease in which the protein aggregates are the direct agent that impairs tissue function [30]. Both lysozyme and insulin are highly structured under physiological conditions, with a low propensity to aggregate. However, the fibrillation process of globular proteins occurs under conditions that may promote partial unfolding (e.g. low pH and high temperature) as well as the presence of mutations that destabilises the native state [31].

The common feature of PMDs is the accumulation of amyloids, a term that is now used to describe aggregates that share a set of common biophysical properties, such as low solubility of mainly highly ordered filamentous structures and the predominant cross

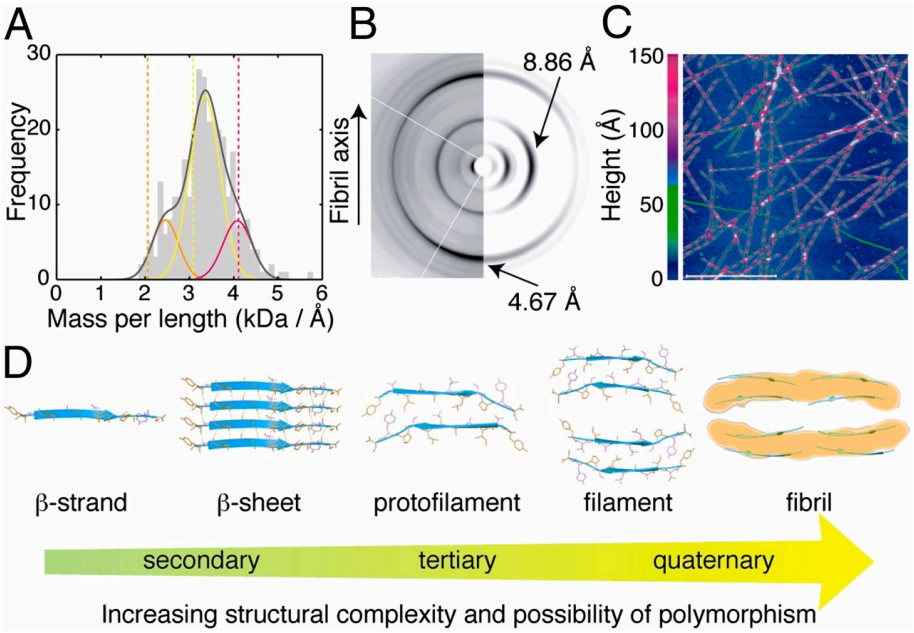

Fig. 1.2 The structure of transthyretin (TTR) studied with five different biophysical techniques: a) Histogram of STEM measurements, b) experimental (left) and simulated (right) X-Ray diffraction pattern, c) AFM of the fibrils, d) the different atomic substructures of amyloid fibrils ordered by hierarchy. Reproduced from [32]

beta-sheet quaternary structure [33, 34]. Amyloid structure is depicted in Figure 1.2 which shows the structure of transthyretin (TTR) fibrils and the atomic substructures studied by different biophysical techniques [32]. In some cases, the accummulation of fibrils is the direct cause of the disease, like the case of cataract in the eye lens [35] but in the case of neurodegenerative disorders the actual cause is less clear as well as the precise pathological agents. However, increasing evidence shows that the oligomers/protofibrils may be the most cytotoxic species that lead to neurodegeneration [36, 37]. Therefore, a good way to understand the onset and development of the disease is to describe the mechanisms involved in the aggregation process on a molecular level. Even though the fibrils are formed by one protein component [38], analysis is complex due to the number of simultaneous processes with multiple species involved.

1.2 The kinetics of amyloid formation

The Oosawa model was the first approach that described the protein aggregation process in two steps, by using an analogy to the formation of crystals [39, 40]. The first step is the

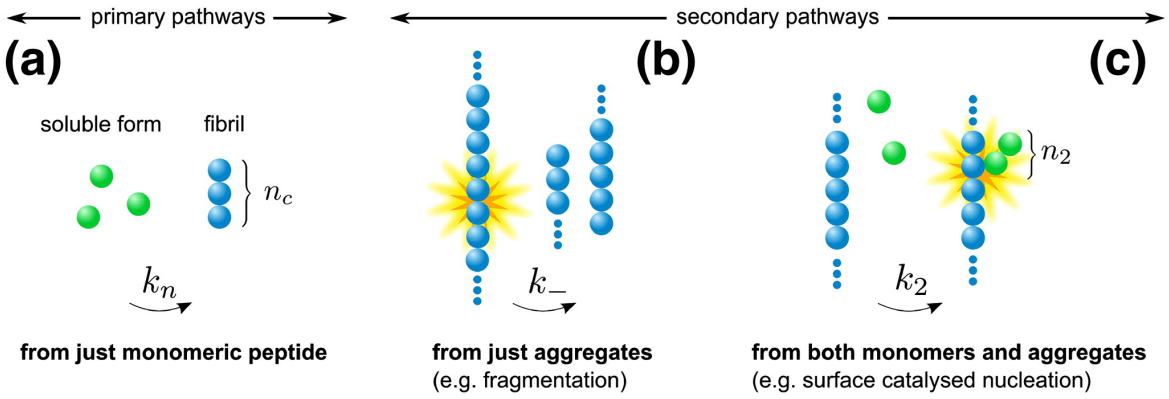

Fig. 1.3 The general mechanisms that describe the protein aggregation process. a) Primary nucleation is the spontaneous formation of nuclei from soluble monomers. b) Secondary pathways are either monomer-independent processes like fragmentation or c) monomer-dependent such as surface catalysed nucleation. Reproduced from [43].

formation of nuclei (primary nucleation) followed by fibril/oligomer growth through filament elongation. While this model describes an analytical solution to the formation of functional amyloids, it does not explain the formation of pathogenic aggregates. A heterogeneous (secondary) nucleation mechanism, in which the surface of a polymer catalyses the formation of new nuclei, was suggested to describe the aggregation of haemoglobin in sickle cell disease with an analytical solution for the early-time approximation [41].

The main difference between functional and aberrant amyloid growth, is the presence of the secondary processes. In functional amyloid growth, the rate of nuclei formation is directly proportional to the concentration of monomer in solution. However, the pathways for aberrant aggregation of proteins are more complex. The presence of surface catalysed nucleation as well as fibril fragmentation, generates more nuclei and duplicates the number of fibril ends for fibril elongation respectively, and complicates the analytical solution of these systems. It was not until 2009 that a complete solution to the kinetic equations that describe amyloid formation was formulated [42]. Overall, the mechanism can be described with the following molecular steps as shown in Figure 1.3:

1. Primary nucleation: spontaneous formation of nuclei from soluble monomers.

2. Elongation: filament growth by addition of soluble monomers to the fibril's ends.

3. Secondary nucleation: surface-catalysed formation of nuclei on pre-existing fibrils.

4. Fragmentation: formation of new fibrils by breakage of fibrils.

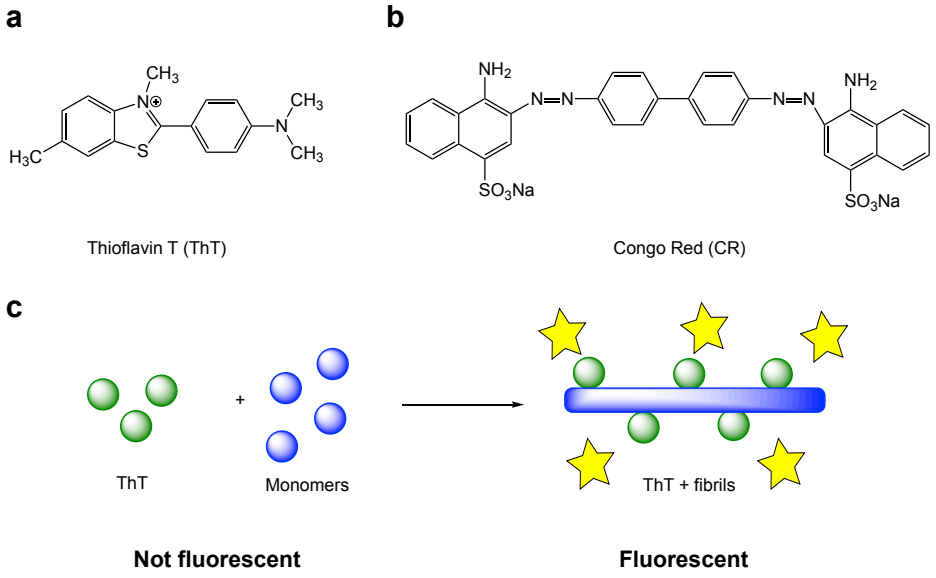

Fig. 1.4 a) Structure of ThT and b) Congo Red dyes. c) Upon binding to amyloid fibrils, ThT emits a fluorescent signal.

The mechanism describes the aggregation of the Aβ42 peptide, the protein involved in Alzheimer's disease [44]. It has also made it possible to study the kinetics of Aβ aggregation in the presence of inhibitors such as molecular chaperones [45] and small molecules [21, 46]. The analysis of the experimental data is performed by determining the change in fibril mass concentration, normally with the addition of dyes like thioflavin T (ThT) [47] or congo red (Figure 1.4), but the latter is used less often as it has been shown to bind not only to amyloid fibrils but native proteins too [48]. Intrinsic protein fluorescence derived from the fluorescent amino acids phenylalanine, trypthophan, and tyrosine, can also be used to study the changes in conformation of proteins [49, 50]. However, the use of intrinsic fluorescence is limited by the requirement of high concentrations of the respective protein.

ThT fluorescence is triggered upon binding to beta-sheet structures (amyloid fibrils) as shown in Figure 1.4. The mechanism of ThT binding is not totally understood but it has been suggested that ThT can form micelles which adhere to the hydrophobic surface of fibrils, and therefore enhances its fluorescence which can be detected by excitation at 450 nm and emission with a maximum at 482 nm [47]. Since the dye binds specifically to amyloid fibrils, it cannot detect the early formation of nuclei in the aggregation process or the presence of pre-fibrillar aggregates.

1.2.1 The toxic oligomers

In the past decade, research indicates that pre-fibrillar aggregates are the main cytotoxic agents for several human amyloidogenic systems [51], for instance Aβ [52], aSyn [37], and the prion protein [53]. It is clear that these species are transient and structurally heterogeneous, making it difficult to study the relation between their structure and toxicity [54]. The main problem in studying the most toxic species lies in the ability to isolate and stabilise them. Therefore, their proper analysis would require a sensitive detection in real-time [55].

The heterogeneous structure and composition of the oligomers may be due to the different pathways that lead to the formation of these pre-fibrillar species [56]. In some cases the pathways are enhanced by solution conditions such as pH and protein concentration or even certain mutations, whereas in others aggregation may proceed via competing pathways. The oligomers can be on-pathway species that lead to fibril formation, or off-pathway particles that work only as a reservoir of monomers.

The toxicity of oligomeric species is determined by both hydrophobicity and size, with the most toxic ones having small size and high hydrophobicity [57]. The mechanisms of toxicity are poorly understood but some studies suggest that the hydrophobic surface of the oligomers can mediate aberrant interactions with other proteins which would result in their functional impairment and sequestration [58]. Furthermore, the oligomers can disrupt artificial as well as biological lipid membranes, compromising the integrity of the cell [59]. Although there is evidence that in some cases mature fibrils are toxic, the toxicity of pre-fibrillar aggregates makes them the primary pathogenic species responsible for the onset of disease [60]. Although there is a debate whether amyloid formation is in fact a mechanism of protection against more toxic species [61], in some diseases like systemic amyloidosis the accumulation of fibrils is the direct cause of organ dysfunction [62], hence protein aggregation is a process that should be avoided for the preservation of biological function [60].

The oligomers that form during the amyloid formation process can be formed either during primary nucleation or secondary nucleation processes. Kinetic measurements carried out with computer simulations indicate that the amyloid formation follows a two-step mechanism that involves oligomers [63]. The primary nucleation occurs through an oligomer with the correct size born during rare fluctuations and thus most oligomers are not of the right size to produce fibrils and will eventually dissociate to monomers. The formation of oligomers through secondary nucleation is determined by the amount of fibrils formed, which grows exponentially with time during the early times of aggregation [64]. The oligomers generated through secondary nucleation are similar to those by primary nucleation, with a highly

disordered structure and low growth rate. Since the toxicity is linked to protein oligomers or their generation process, over the time course of an aggregation reaction the secondary nucleation generates many orders of magnitude more oligomers than primary nucleation. This may suggest that in order to interfere with the aggregation process in a disease context, it would be necessary to derive inhibitors that supress the adsorption of monomers onto the surface of protein fibrils (secondary nucleation) [63].

The structural characterisation of oligomeric species during amyloid formation has been particularly challenging due to their transient, low abundant and heterogeneous nature. Their identification has been made by means of indirect experimental data, enriching the samples with other stable oligomers, fluorescence-based techniques, AFM in combination with FT-IR and single-molecule fluorescence approaches [65]. However, it would be desirable to have a highly sensitive technique that could provide structural information of the oligomers in the biologically-relevant state.

1.3 Structural techniques

NMR and X-Ray crystallography are among the most powerful techniques to characterise macromolecular structures with high-resolution. Nevertheless, they both have some drawbacks. X-Ray needs the isolation of pure crystals to obtain the detailed information of the structure, and the crystalline structure may not resemble completely the one in solution [66]. NMR has the potential to determine structures at the atomic level, as well as molecular dynamics, but it is limited to proteins of up to 35 kDa, mostly because of sensitivity loss and increasing complexity of spectras of bigger structures [67]. Recent advances in solid-state NMR have made it possible to study large monomeric proteins and protein complexes, but its applicability is limited by the ambiguous assignment of the NMR signals in large systems [68].

Mass spectrometry is also one of the fundamental tools used for proteomics in molecular and cell biology. In combination with other separation techniques, such as liquid or gas chromatography, it can be used to study protein-protein interactions as well as to provide a full description of the protein composition of multiple organisms [69]. The main limitation of the technique is that for some samples, an additional separation step prior to analysis is required, and the time-scale of the experiment. Therefore, studying transient samples in biologically relevant environment is difficult with mass spectrometry.

Cryo-electron microscopy (CryoEM) has emerged as a powerful technique for structural biology. In comparison with NMR and X-Ray crystallography, it has less limitations for

the amount and purity of sample required. Despite the fact that the technique is close to atomic resolution for large complexes, solving small specimens remains challenging [70]. Furthermore, the samples have to be frozen and remain surrounded by water, this mantains biological conditions to a certain extent [71]. Another drawback of CryoEM is the long time required for data collection, which makes the throughput for screening slower than for X-Ray crystallography [72]. Despite its limitations, CryoEM has already made it possible to study amyloid fibrils from patient-derived material [73] as well as the structure of a protofibril formed by a fragment of the prion protein [74].

Some other traditional methods are performed to study protein- protein interactions on a daily basis in almost every biophysical research laboratory. The sodium dodecyl-sulphate polyacrylamide gel electrophoresis (SDS-PAGE) is one of the most commonly used techniques as it provides information on the molecular weight of proteins and protein complexes [75, 76]. By addition of antibodies after the gel separation (Western Blot analysis), it can be used to detect specific proteins in a complex mixture. However, the analysis of protein aggregates with SDS-PAGE has shown to be unreliable as there is evidence that oligomeric states can be affected by the denaturing process [77, 78]. An alternative to SDS-PAGE is to perform electrophoresis of proteins in the absence of SDS or other denaturing agents, i.e. under "native" conditions, method known as native PAGE [79]. Under such conditions the separation depends on the individual charge of the protein and the pH of the separation, and hence it requires to optimise the protocol for the respective sample. Size exclusion chromatography (SEC) coupled to multiple detection techniques can be used to study oligomeric states of proteins [80, 81]. SEC allows to determine the hydrodynamic radius of proteins as the molecules are retained in the column according pore size of the resin [82]. Nevertheless, the detection method should be sensitive enough to detect low concentration of samples, as it is the case of the on-pathway oligomers.

Other biophysical approaches can be used to study proteins in solution, such as Isothermal Titration Calorimetry (ITC) and Surface Plasmon Resonance (SPR). They can provide important information, such as binding constants, as well as kinetic and thermodynamic parameters [83]. However, they have a number of limitations such as interference from solution conditions, high levels of sample consumption (ITC) and potential surface artefacts (SPR) [84].

A traditional sizing technique is Analytical Ultra Centrifugation (AUC), which allows the determination of monomeric and oligomeric protein sizes [85]. However, the application of AUC to heterogeneous mixtures has its limitations, since deconvolution of the sedimentation equation of the mixture becomes quite complex [86]. Dynamic Light Scattering (DLS) is

a more rapid technique than AUC, and perhaps the most popular for determining particle size in solution. It measures the change in the light trajectory (scattering) after the incoming monochromatic light hits particles in Brownian motion [87]. Nevertheless, it can be problematic for heterogeneous mixtures. Since large particles scatter more light than the small ones, usually the result of a polydisperse mixture is biased towards the large particles. The preparation of the sample should therefore be made carefully in order to avoid dust particles or other contaminants, and the concentration should be adjusted so that the scattering intensity is at least 10 times that of the solvent (good signal-to-noise ratio). Therefore a poor sample preparation may lead to errors in the measurement.

An obvious alternative to the methods presented above is the use of microfluidics, mostly because of its potential to miniaturise different biological systems which enables high-throughput processes and a favourable scaling of physical forces.

1.4 Microfluidics

Microfluidics is the science and technology of manipulating fluids in channels with dimensions of tens of micrometres [88]. The use of microchannels allows the integration, miniaturisation and automation of various processes. However, the main characteristic of microfluidics is the physics that govern the processes at the microscale, such as the mass transport which is dominated by viscous forces rather than inertial ones, with a laminar flow behaviour. This laminar flow generates some advantages over macroscopic tools, such as faster diffusive heat and mass transfer at the microscale, as well as enhanced spatiotemporal resolution and subcellular resolution [89]. Overall, microfluidic technology presents many advantages for studying biological systems, among them [90]:

- Laminar flow. Enables the manipulation of fluids with high precision and a purely diffusive mixing.

- Small volumes. Small volume confinement not only reduces sample-consumption, but also it can effectively amplify the limits of detection of the biomolecules or cells under investigation.

- High throughput analysis. The miniaturisation of chemical and biological processes allows to integrate them in parallel in a single device, which is particularly useful for screening on-chip.

- Integration. The small size, planar geometry and transparency of microfluidic devices make them suitable to integrate with many other analysis techniques.

1.4.1 Origins and applications

Microfluidic technology has its origins back in the 1950s, with the development of ink-jet technology and the necessity to dispense volumes in the order of nano and sub-nanolitres [91]. With the development of genomics in the 80's and the need to develop a technology to integrate and parallelise multiple processes, microfluidics could provide the solution for these problems. A second driving force for the development of microfluidic systems came from the US Department of Defense, which in the 1990s aimed to develop microsystems for the detection of chemical and biological threats [88].

During the 80's and 90's most of the microfluidic fabrication was made with silicon substrates, but at the end of the 90's with the development of soft-lithography methods of poly-di-methyl-siloxane (PDMS) the technology enabled the fabrication of relatively cheap devices. This is the most popular procedure currently used [89].

The variety of microfluidics applications is quite broad, from its use in basic research in chemistry, biology and physics, to applications in diagnosis and biomedical devices. The main drawback of microfluidics was perhaps that the technology was limited to laboratory with the specific equipment to use these devices, mostly pumps and specialised optics equipment. However, nowadays efforts are done to make this technology more accessible to people outside the laboratory. Several companies sell microfluidic solutions in the form of benchtop equipment where the user does not have to do more than loading the sample. Another example is Point-Of-Care (POC) applications, which needs the development of diagnosis devices that are easy enough to use by the side of the patient by clinicians, nurses or by themselves, and not necessarily a microfluidic expert.

The use of microfluidics in the life sciences has become a crucial element, particularly in cell biology and protein biophysics. One of the advantages of microfluidics over other technologies is the low-volume of sample consumption and the enhancement of sensitivity. Advances in microtechnologies have supported areas as diverse as biomarkers in diagnostics, biomaterials and drug discovery [92]. The use of microdroplets, for example, has enabled key developments in cell biology as it allows quantitative analysis of single cells [93] as well as high throughput phenotyping and genotyping at the single cell level [94].

1.4.2 The fluid flow at the microscale

The physics in microfluidic channels is analogous to those in electronics, with a flow of fluid and a flow of electrons, respectively. But unlike with microelectronics, the laws of physics scale more dramatically in microfluidics. Perhaps the most important change is that in the mass transport in microfluidics inertial forces are negligible, and viscous forces are the predominant ones [91]. The relative importance of the various phenomena ocurring in fluidic physics can be expressed in a series of dimensionless numbers [95]. One of them, the Reynold's number, relates the inertial to viscous forces:

$$\mathrm{Re} = \frac{f_i}{f_v} = \frac{\rho U_0 L_0}{\eta} \tag{1.1}$$

where U_0 is the flow velocity of the fluid, ρ its density, L_0 a typical length scale (e.g. the channel width) and η the fluid viscosity. The Reynold's numbers in microfluidic devices are small, between the order of 10 to 10^{-6}. Under these conditions the flow is laminar, but as the Reynold's number increases, turbulence destabilises it.

The Péclet number relates advective and diffusive transport rates. If τ_D is the time it takes for particles to diffuse over a distance L_1, then

$$\tau_D = \frac{L_1^2}{D} \tag{1.2}$$

where D is the diffusivity $D = \frac{k_B T}{6\pi\eta R_H}$ for particles with hydrodynamic radius R_H, k_B the Boltzmann constant and T the temperature in Kelvin. The time τ_A for particles to advectively cross a distance L_2 is

$$\tau_A = \frac{L_2}{U_0} \tag{1.3}$$

and the Péclet number is the ratio between τ_D and τ_A:

$$\frac{\tau_D}{\tau_A} = \frac{\frac{L_1^2}{D}}{\frac{L_2}{U_0}} \tag{1.4}$$

In the case $L_1 = L_2 = L_0$, the Péclet number can be expressed as $\mathrm{Pe} = \frac{L_0 U_0}{D}$. But in the case of a diffusion channel, where L_1 is the channel width w and L_2 is the channel length L, the Péclet number can be expressed as

$$\mathrm{Pe} = \frac{U_0 w^2}{LD} \tag{1.5}$$

In the world of microfluidics, the low-Re results in mixing that depends on diffusion alone. This purely diffusive mixing may represent a problem when rapid mixing is required, for example in a chemical reaction, but may be desirable in some other cases, as it can be used for particle sizing among other applications.

1.5 Aims

The aim of this thesis is to develop a microfluidic platform that integrates the diffusional sizing method along with immunochemical assays that, due to their use of antibodies, provides specific and sensitive detection. The technique, which I named “Immuno Diffusional Sizing (IDS)", aims to be used as an alternative or a complement to the methods mentioned in the introduction. IDS is applicable to a range of disease-relevant proteins and proteins under a biologically relevant environment, including insulin, the Aβ peptide, aSyn and PrP. It enables the sizing of protein aggregates, such as oligomers, which as explained previously, are particularly challenging to study due to their low abundance and transient nature.

Chapter 2

Materials and Methods

2.1 Microfluidic device fabrication and flow control

2.1.1 Microfluidic device fabrication

All photomask devices were designed using the Autodesk AutoCAD software platform. The microchannels were printed on acetate masks (Micro Lithography Sevices, Essex, UK). Microfluidic channels were fabricated using standard soft-lithography techniques [96] as illustrated in Figure 2.1.

Masters were made by spin-coating a small volume ($\sim$3 ml) of SU-8 photoresist (MicroChem Corp., Rugby, UK) and placed onto the centre of a circular silicone wafer (3" diameter, Micro Chemicals, Germany). The spin speed was chosen based on the desired height and SU-8 used and, for these experiments, SU-8 3025 and 3050 were used to create 25 μm and 50 μm thick layers respectively, using a spin speed of 3000 rpm. After the coating, the wafer was a soft-baked at 90° C for 12 (SU-8 3025) to 25 (SU-8 3050) min. Following this, the photomask patterned with the desired design was fixed to the wafer using a press with a UV-transparent cover. The wafer was then exposed to a UV-light emitting diode (UV-LED) [97] at 1000 mW for 50 s. The resultant master was then baked again (90° C), this time for 5 min (for both SU-8 3025 and 3050). After this, the non-crosslinked SU-8 was removed using a developing agent (Propylene glycol methyl ether acetate, PGMEA) by placing the wafer in a glass evaporation dish, filled until the wafer is covered with PGMEA. The dish was then agitated for 3 (SU-8 3025) to 5 (SU-8 3050) min, before being rinsed with first PGMEA and then isopropyl alcohol (IPA). The wafer was then blown dry with nitrogen, before being stored in a covered petri dish. For all diffusional-sizing experiments, the height of the channels was measured with a Bruker Dektak® profilometer (Coventry, UK).

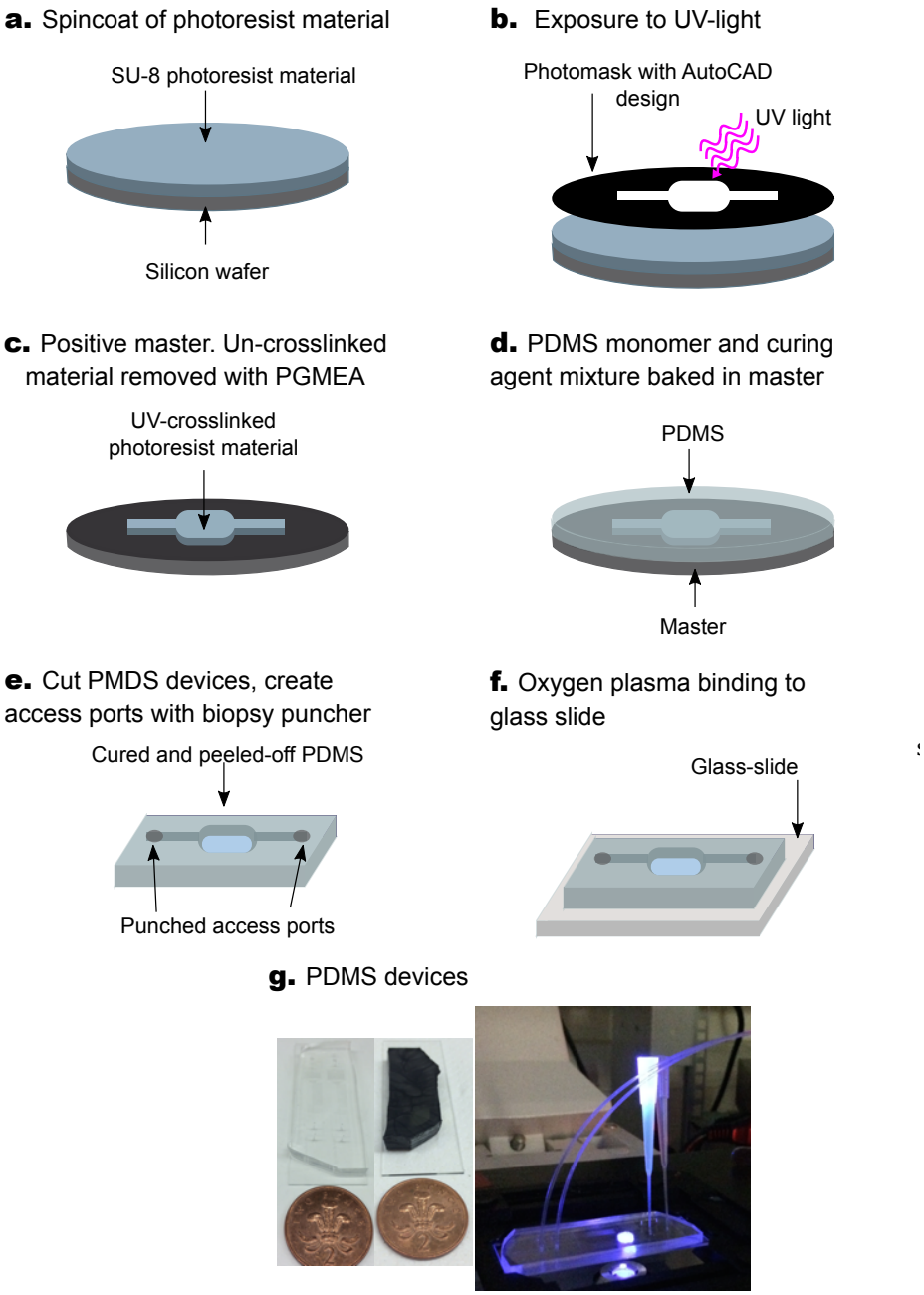

Fig. 2.1 Schematic description of microfluidic device fabrication with soft-lithography.

The master was then covered with a mixture of poly-di methyl siloxane PDMS (Dow, Corning) with crosslinker (Sylgard 184, Dow Corning) in a 10:1 (w/w) ratio, and degassed for 15 min. For black PDMS devices, a small amount of carbon nanopowder (Sigma Aldrich, UK) was added to the PDMS mixture and centrifuged for 15 min at 2000 rpm before pouring it into the master. The mixture in the master was baked for 1.5 h at 65° C. The set of PDMS

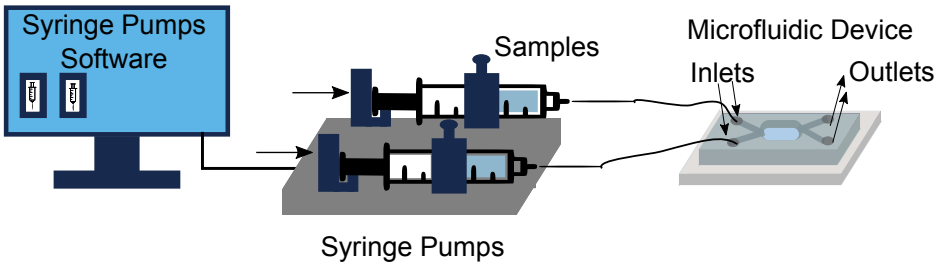

Fig. 2.2 Schematic description of flow rate controlled by syringe pumps. The flow rates are selected with the pumps software. The syringes are attached to the pumps. In this example, the samples are injected through the device inlets by positive displacement of the pumps.

devices was then removed from the master using a scalpel, connections were made with biopsy punches (0.75 mm diameter), and then the devices were plasma bonded to glass slides using oxygen plasma (Diener Electronic Femto plasma oven). In this case, the devices and glass slides were exposed to oxygen plasma for 10 s at a power of 40 mW and a pressure of 3 mbar. For binding PDMS devices to quartz slides instead, the exposure to oxygen plasma was for 30 s at a power of 40 mW.

In order to prevent protein-adsorption to the PDMS channels, extended plasma oxidation of the PDMS surface was conducted, which created a silanol-rich hydrophilic layer [98]. The treatment was performed after the devices were bound to glass/quartz slides, exposing to oxygen plasma for 500 s at a power of 80 mW and a pressure of 3 mbar.

2.1.2 Microfluidic flow control

The flow in the channel was controlled by applying positive displacement at both inlets (Figure 2.2), buffer and analyte, by using two syringe pumps (Cetoni neMESYS, Cetoni GmbH, Korbussen, Germany) at a flow rate of 60 μl/h insulin and 540 μl/h buffer for the first device designed. In the second generation device, H-filter, total flow rates in the range of 80-400 μl/h were used, with the analyte flow $\frac{19}{40}$ of the total flow rate. The buffer and protein solutions were injected through a 1 ml plastic syringe (HSW) connected with plastic tubing (0.38 mm ID, 1.09 mm OD) to the PDMS device. Both fractions, 1 and 2, were collected by connecting the device with a low-binding tube with plastic tubing. The collection time varied between 30 min and 3 h, according to the sample volume needed and flow rate used.

2.2 IDS calibration and testing protocols

2.2.1 Insulin immunodetection

Lyophilised human insulin was supplied by Sigma-Aldrich UK, and used without further purification. An insulin stock of 10 mg/ml was prepared in 50 mM HCl, filtered though a 22 μm filter and the concentration was measured in the NanoDrop 2000c (ThermoFisher Scientific) by UV-absorbance at 276 nm, using an extinction coefficient value of 1 for 1 mg ml^{-1} [99]. Insulin hexamer was prepared as described previously [100]. For the detection of human insulin, the commercial HTRF® immunoassay kit was used, purchased from Cisbio Bioassays (Codolet, France). Briefly, insulin samples (2 μl per well) were mixed with the antibody-pair (18 μl per well) and incubated for 30 min at room temperature. The TR-FRET readings were performed in Clariostar® (BMG Labtech) always simultaneously with a standard curve, made of 1:2 serial dilutions starting from 2 nM insulin.

2.2.2 Calibration measurements of the diffusional separation device

Different flow rates were measured by injection of mQ water with positive displacement with two syringe pumps (Cetoni neMESYS, Cetoni GmbH, Korbussen, Germany), with microfluidic flow sensors (Elveflow® Elvesys Innovation Centre, Paris, France) connected at the outlets of the device. Colloids with 25 nm radius were bought pre-labelled with fluorescein from ThermoFisher as 2.5% by volume suspensions. They were diluted to 0.1% by volume in mQ water solutions for measurement. Images were acquired every 5 min, at a flow rate of 80 μl/h for each device, with colloids at 38 μl/h and water at 42 μl/h.

2.3 IDS of Prion Proteins

Experiments with PrP were carried out at the facilities of the Institute of Neuropathology, University of Zürich, Switzerland.

2.3.1 Recombinant mPrP

Full length murine prion protein ($mPrP_{23-231}$) was recombinantly expressed and purified as previously described [101–103]. The PrP^C monoclonal POM antibodies were purified as previously described [104]. POM19 was labelled with the donor fluorophore (Eu-chelate) and POM1 was labelled with the acceptor fluorophore allophycocyanin (APC) acceptor as

previously reported [105]. The TR-FRET measurements were performed in a platereader at 620 and 665 nm after a 1 h incubation (37°C) and after overnight incubation (4°C) for better signal stabilisation.

2.3.2 Prion inoculation

30 μl of 0.1% of RML6 (passage 6 of Rocky Mountain Laboratory strain mouse-adapted scrapie prions) BH was injected intracerebrally into PrP^C overexpressing Tg20 mice [106]. Mice were monitored three times per week, and daily close to terminal stage. Mice had unrestricted access to food and water. Prion-infected mice were sacrificed at the terminal stage of prion disease. All animal experiments were conducted in strict accordance with the Rules and Regulations for the Protection of Animal Rights (Tierschutzgesetz and Tierschutzverordnung) of the Swiss Bundesamt für Lebensmittelsicherheit und Veterinärwessen BLV. All animal protocols and experiments performed were specifically approved for this study by the responsible institutional animal care committee, namely the Animal Welfare Committee of the Canton of Zurich (permit numbers ZH040/15). All efforts were done to minimise animal discomfort and suffering.

2.3.3 Mouse brain homogenates preparation: ZH1, Tg20 and RML-infected Tg20.

Brains were prepared by Petra Schwarz, homogenisation was performed by myself.

The mouse brains from ZH1 $PrP^{0/0}$ and Tg20 mice were washed with ethanol (2x, 70%) and sterile PBS (4x). Then they were homogenised in an eight-fold amount of sucrose (0.32 M) to prepare a 10% wt. solution with the Ribolyzer tube (speed 6.5, 4x 35s). After the first homogenisation step the tubes were cooled down on ice and the step was repeated 2 more times. The Tg20 and RML-infected Tg20 brains used for subsequent PK-digestion were homogenised in PBS only because the sucrose interfered with the PK-digestion. The homogenates were centrifuged (700g, 3 min). The supernatant was collected for further use and the pellet was discarded. Before injection into the microfluidic device, the BH samples were diluted to 1% on tris buffer (50 mM, pH 7.4, 1% wt. BSA).

2.3.4 PK-digestion of RML-infected Tg20 brain homogenate

Conducted by Riita Moos.

Uninfected and RML-infected Tg20 10% BH were diluted to 2% in PBS. 10 μl of proteinase K (1000 μg/ml, C_f= 50 μg/ml) was added to 190 μl of 2% BH. The mixture was incubated for 2 h at 37°C under continuous shaking at 650 rpm. The digestion was stopped by addition of PMSF to a final concentration of 3 mM and incubation was performed for 15 min with continuous shaking at 750 rpm. The samples were analysed by Western Blot (Appendix A). For better results, the sample was injected freshly after PK-digestion directly into the microfluidic device. See Appendix A for details on the digestion conditions.

2.3.5 Details of the microfluidics experiments

The flow in the channel was controlled by applying positive pressure at both inlets, buffer and analyte, by using two syringe pumps (Cetoni neMESYS, Cetoni GmbH, Korbussen, Germany) at total flow rates in the range of 80-400 μl/h, the analyte flow being $\frac{19}{40}$ of the total flow rate. For recombinant mPrP, a flow rate of 200 μl/h was used with the 200 μm width device. For all brain PrP samples, tests with both devices (200μm and 80μm width) were conducted, at flow rates of 200μl/h and 80μl/h, respectively. The buffer and protein solutions were injected through a 1 ml syringe (HSW) connected with plastic tubing (0.38 ID, 1.09 OD) to the PDMS device. Both fractions, 1 and 2, were collected by connecting the device to a low-binding tube with plastic tubing. The collection time varied between 30 min and 3 h, according to the sample volume needed and flow rate used. The auxiliary stream was the tris buffer with BSA (0.1%), which prevents the proteins sticking to the PDMS channels.

2.3.6 Detection of PrP^C with TR-FRET

Recombinant mPrP and Tg20 BH TR-FRET: aliquots of the samples extracted from the outlets (25 μl) were mixed with the antibody-pair, Eu-labelled POM1 and APC-POM19 (5 μl each) in a 384-well plate. After 10 min shaking (300 rpm, RT) the sample was incubated at RT for another 50 min before measuring in a Paradigm® platereader (Molecular devices, San Jose, CA, USA). The labelled antibodies and protein were diluted in Tris (50 mM, pH 7.43) with BSA (1%).

RML-infected Tg20 non-digested and digested BH treatment for ELISA: in order to disassemble the fibrils before detection with ELISA, aliquots of the samples extracted from the outlets (162 μl) were mixed with 21 μl NaOH (0.5M, C_f=57.9 mM) and incubated for 10 min at RT under continuous shaking (700 rpm). 24 μl of neutralising buffer (NaH_2PO_4) was then added and incubated for 10 min at RT under continuous shaking (700 rpm).

2.3.7 Sandwich ELISA protocol for PrP

This protocol was developed by Daniel Heinzer (Institute of Neuropathology, University Hospital Zürich, Switzerland). Experiments carried out by myself.

The desired wells of a 384-well high binding transparent plate were coated overnight at 4°C with 50 μl of the capture antibody POM1 (400 ng/ml) in coating buffer (0.1M Na_2CO_3/$NaHCO_3$). The plate was aspirated 4 times in washing buffer (PBS, 1% Tween) before addition of 100 μl/well of blocking buffer (5% TopBlock in PBS-T) and incubated for 2 h at RT. The plate was aspirated four times in washing buffer before addition of the samples. A standard curve of recombinant mPrP was prepared by 1:2 serial dilutions starting with 5 ng/ml of mPrP. PrP samples were added (50μl) to the desired wells. After incubation of the samples for 1.5 h at RT, the plate was washed four times with PBS-T buffer. 50 μl of the detection antibody, biotin-labelled POM19, was added in sample buffer (1% TopBlock in PBS-T) at a concentration of 1:5000 and incubated for 1 h at RT. The plate was washed four times with the washing buffer and 50 μl of avidin-HRP was added (1:1000 in sample buffer) and incubated for 1 h at RT. The plate was again washed four times with the washing buffer before addition of 50 μl/well of stabilised TMB. After a 15 min incubation the reaction was stopped by addition of 1 N H_2SO_4 and the absorbance read at a wavelength of 450 nm.

2.4 IDS of amyloidogenic oligomers

2.4.1 Amyloid beta monomer expression and purification

Conducted by Sean Chia and Ewa Klimont.

Expression and purification of the recombinant Aβ40 were carried out as previously described for Aβ42 [21]. In brief, Aβ40 was expressed in the *E. Coli* B21Gold (DE3) strain (Stratagene, La Jolla, CA) and purified by sonicating the bacterial cells and dissolving the inclusion bodies in urea (8M), followed by ion exchange in batch mode on a diethylaminoethyl cellulose resin. The fractions were lyophilised and further purified using a Superdex 75HR 26/60 column (GE Healthcare, Chicago, IL) and eluates were analysed using SDS-PAGE for the presence of Aβ40. The fractions containing the recombinant protein were combined, frozen using liquid nitrogen, lyophilised in either sodium phosphate buffer (20 mM, pH 8.0) for preparing Aβ40 monomers or ammonium acetate (50 mM, pH 8.5) for producing Aβ40 oligomers, and stored at -80°C.

Before injection into the microfluidic device, solutions of the monomeric peptide were prepared by re-dissolving the lyophilised Aβ40 peptide in guanidinium hydrochloride (6M).

The monomers were purified from any oligomeric species and salts using a Superdex 75 10/300 GL column (GE Healthcare, Chicago IL) at a flow rate of 0.5 ml/min, and eluted in sodium phosphate buffer (20 mM, pH 8). The centre of the peak was collected and the concentration of the peptide determined from the absorbance of the integrated peak area (ε_{280}=1490$M^{-1}cm^{-1}$).

2.4.2 Amyloid beta oligomers preparation

Performed by Dr Benedetta Mannini and Sean Chia.

The preparation of Aβ40 oligomers was carried out as previously described [107]. In brief, lyophilysed Aβ40 peptide (1 mg) was dissolved in hexafluoroisopropanol, HFIP (300 μl, 100%) overnight at 4°C and the solvent was then allowed to evaporate under a gentle flow of N_2. The peptide was resuspended in DMSO (100 μl/mg) and sonicated twice (10 min, RT). The Aβ40 peptide in DMSO was then diluted in sodium phosphate buffer (20 mM, pH 6.9) with $ZnCl_2$ to a final concentration of 100 μM of Aβ40, incubated at 20°C for 20 h and centrifuged (15000xg, 15 min, 20°C). The pellet containing the oligomers was resuspended in phosphate buffer (20 mM, pH 6.9) with $ZnCl_2$ (200 μM).

2.4.3 Immunodetection assay of Amyloid beta monomers and oligomers

The samples were collected separately from both outlets of the device and treated as indicated in the protocols of Cisbio Bioassays Inc.(Codolet, France). The immunoassays readings were performed on a CLARIOstar® platereader system (BMG Labtech GmbH, Ortenbeg, Germany) in white polystyrene plates with volumes of 20 μl per well. The incubation time before reading was 90 min (RT) for the Aβ40 (monomer and oligomers) at RT. The labelled antibodies, as well as the proteins, were diluted in the buffer: NaH_2PO_4 (50 mM) pH 7.4, BSA (0.1%). Monomeric Aβ40 was used for the standard curve of the Aβ40 monomer experiment and the respective oligomer for the sizing of each of them, in serial 1:2 dilutions with a starting concentration of 2 nM.

2.4.4 Isolation of on-pathway Amyloid beta oligomers by SEC

Performed by Sean Chia.

Aggregation of Aβ40 (60 μM) in phosphate buffer (20 mM, pH 7.4) was carried out by placing the 96-well plate at 37 °C under quiescent conditions in a plate reader (Fluostar Optima, BMGLabtech, Offenburg, Germany). The aggregation process was followed with a

sample with ThT. The control fluorescence was measured through the bottom of the plate with a 440 nm excitation filter and a 480 nm emission filter. A sample was taken after 1.6 h incubation and run again through a Superdex 75 10/300 GL column (GE Healthcare, Chicago IL) at a flow rate of 0.5 ml/min, and eluted in sodium phosphate buffer (20 mM, pH 7.4) to separate the oligomeric fraction from the monomer, as previously described [44].

2.4.5 aSyn expression and purification

Performed by Catherine Xu.

Wild-type (WT) aSyn was purified from *Escherichia coli* BL21 cells, transformed with the pT7-7 plasmid encoding the protein. Point mutations of the original plasmid were used for the mutants (G51D and H50Q). Cells were grown in 2xYT (37 °C, 180 rpm) with ampicillin (100 μg/ml), induced with IPTG (1 mM), incubated overnight (28 °C, 180 rpm), and harvested by centrifugation in a Beckman Avanti J25 centrifuge with a JLA-8.1000 rotor for 30 min at 6238 x g (Beckman Coulter UK Ltd., High Wycombe, UK). The cell pellet was resuspended in 10 mM Tris-HCl (pH 7.7), 1 mM EDTA, complete protease inhibitor cocktail (1 tablet/40 ml; Roche, West Sussex, UK), and lysed by sonication. Following centrifugation (JA-25.50 rotor, 39191 x g, 30 min), the supernatant was boiled for 20 min and centrifuged (39191 x g, 30 min). Streptomycin sulphate was added to the supernatant to a final concentration of 10 mg/ml (30 min incubation at 14 °C and centrifuged (39191 x g, 30 min). Ammonium sulphate was added to the supernatant to 361 mg/ml and stirred at 4 °C for 30 min. The mixture was centrifuged (39191 x g, 30 min), and the pellet resuspended in 25 mM Tris-HCl (pH 7.7), dialysed overnight, and loaded onto a HiLoadTM (TM in superscript) 26/10 Q sepharose high performance column (GE Healthcare Ltd., Little Chalfont, UK) and eluted at $\tilde{3}$50 mM NaCl with a salt gradient from 0 M to 1.5 M NaCl over 600 ml. Selected fractions were subsequently loaded onto a Superdex 75 26/60 (GE Healthcare Ltd.) and eluted in PBS. Protein concentration was determined by absorbance at 275 nm, using an extinction coefficient of 5600 $M^{-1}cm^{-1}$.

2.4.6 aSyn oligomer preparation

Conducted by Catherine Xu.

The preparation of oligomeric aSyn, for WT and mutants (G51D, H50Q), was carried out as previously described [108]. In brief, lyophilised wildtype aSyn was resuspended in PBS buffer (pH 7.4) to a final concentration of 12mg/ml and filtered (0.22 μm cut-off) immediately before incubation at 37 °C for 20-24 h without shaking to avoid the conversion

into fibrils. The fibrillar species were removed by ultracentrifugation (1 h, 90 000 rpm) and the excess of monomer was removed by filtration (with 100-kDa cutoff membranes). The concentration was determined from the absorbance (ε_{275}=5600$M^{-1}cm^{-1}$) given in monomer equivalents (mass concentration). The oligomers were stable for days at RT and were used for injection into the device at a maximum of 2 days after their production.

2.4.7 OVX Brain homogenates preparation

Brain homogeneate samples were prepared by Dr Sarah Threllfel at the University of Oxford facilities (Oxford Parkinson's Disease Centre, Department of Physiology, Anatomy and Genetics, Oxford, UK).

Brains (aSyn overexpresser (SNCA-OVX), WT aSyn and knockout ($Snca^{-/-}$)), were washed 2x in ethanol 70% and 4x in sterile phosphate buffer saline (PBS) in the original falcon tubes. Brains were homogenised in 0.32 M Sucrose (prepared in distilled water), or lysis buffer (from the Cisbio HTRF aggregated aSyn kit), with the Ribolyser. 2 brains and the eight-fold amount of sucrose (or lysis buffer) were homogenised to prepare 10% homogenate (868.8 mg brain + 7819.2 μl sucrose, speed: 6.5, time: 4x 35 s). After the first homogenisation step the tubes were cooled down on ice and the step was repeated 2 times. The homogenates were collected in 50 ml falcon tubes. The sample was centrifuged at 700 g for 3 min. The supernatants were aliquoted in 1 ml eppendorf tubes (500 μl each) and frozen at -20°C. The samples were shipped to the Department of Chemistry, Cambridge, on dry ice.

2.4.8 *In vitro* translation and *In vitro* ubiquitination of aSyn

In vitro translation and ubiquitination reactions carried out by Shai Zilberzwige.

His-tagged aSyn expresses in cell-free *in vitro* transcription (4 h, 37°C). *In vitro* ubiquitination (IVU) was carried out by mixing 1/10 of the *In vitro* translation (IVT) reaction with E3 ligase specific to aSyn and incubation for 1 h at 37°C. The ubiquitinilation was confirmed using western blots with antibodies against aSyn and ubiquitin.

2.4.9 Immunodetection of aSyn

The detection of monomeric as well as brain aSyn was performed with the alphaLISA® kit purchased from PerkinElmer (PerkinElmer,Seer Green, UK). Given their light sensitivity, these reagents were stored and handled under filtered and subdued lighting. The protocol used was the 2-steps addition. The immunoassay readings were performed on a CLAR-

IOstar® plate reader system (BMG Labtech GmbH, Ortenbeg, Germany) in 384-well white polystyrene plates with volumes of 100 μl per well.

The detection of aSyn oligomers was conducted with the TR-FRET kit purchased from Cisbio (Codolet, France). The immunoassay readings were performed on a CLAR-IOstar® plate reader system (BMG Labtech GmbH, Ortenbeg, Germany) after 1 h incubation at 25°C, in 384-well white polystyrene low-volume plates.

2.5 Towards TR-FRET on-chip detection

The TR-FRET and alphaLISA kits for insulin were purchased from PerkinElmer.

TR-FRET measurements were performed in a Clariostar® platereader at 25°C on cycles of 15 min. alphaLISA measurements were performed as indicated by the PerkinElmer protocol with the 2-step protocol: mixing the antibodies, sample, and acceptor beads together first, incubating, then adding donor beads for final incubation.

2.5.1 Microfluidic experiments

Microfluidic devices were prepared as indicated in Section 2.1, using the protocol for black PDMS devices bound to quartz slides.

2.5.2 TR-FRET Platform

Light from a 340 nm Mounted LED (Thorlabs M340L4) was passed through an aspherical lens of focal length to obtained a collimated beam. This beam was incident on a dichroic filter cube, which consists of an excitation filter (Semrock FF01-340/22-25) centred at a wavelength 340 nm and a dichroic mirror (Semrock FF347- Di01). The light is focused onto the sample flowing in a microfluidic device by an infinity corrected UV objective lens (magnification 10X, numerical aperture = 0.25). The fluorescence from the sample is collected through the same objective, passed through an emission filter (Semrock FF01-625/26 or FF01-661/20-25) centred at a wavelength of 625 and 661 nm respectively, and finally focused onto a EMCCD camera (Evolve Delta Photometrics) by an air-spaced achromatic doublet lens (Thorlabs ACA254-200-UV) of focal length 200 mm. The exposure time used in our experiments was about 500-1000 ms. See Appendix A for spectra details.

Propidium iodide (Sigma Aldrich, UK) was diluted in water to a concentration of 1 mM, and used as a calibration dye.

2.6 Chaperone influence on insulin aggregation

2.6.1 Materials

Bovine insulin was purchased from Sigma Aldrich and it was used without any further purification. The concentration of insulin in solution was determined by absorbance at 276 nm, using an extinction coefficient value of 1 for 1 mg ml^{-1} [99]. All inorganic chemicals were obtained from Sigma Aldrich unless otherwise specified. In all cases, mQ H_2O (18.2 mΩ) was used to prepare the aqueous solutions.

2.6.2 Expression and purification of alpha B-Crystallin

Expression and purification method adapted from the protocol of Justin Benesch's laboratory (University of Oxford, United Kingdom).

Standard heat-shock transformation of chemically competent bacteria

A human aBC gene (codon-optimised for *E. coli* expression) in a kanamycin resistant pET24d(+) vector (5 μl DNA) was mixed with BL21-Gold cells (Agilent, 50 μl). The mixture was kept on ice (30 min) and then it was heat-shocked by placing half the tube in a 42 °C water bath (45 s). The mixture was kept on ice (2 min) before adding it into LB media (250 μl, no antiobiotic) and grown in the incubator (180 rpm, 37°C, 45 min). The transformation was spread onto agar plates (containing kanamycin, 50 μg/ml) and incubated overnight (37 °C, 180 rpm). One of the colonies was chosen and it was placed in LB media (12 ml) previously inoculated with kanamycin (50 mg ml^{-1}, 12 μl). After overnight incubation (37 °C, 180 rpm), the cells were mixed in a 1:1 ratio with a glycerol solution (50% v/v glycerol/water). The glycerol cell stock was separated in eppendorf tubes and frozen in liquid N_2 for further storage at -80 °C.

Expression in LB and OverExpression Media

The pre-culture was prepared by addition of frozen cells from the glycerol stock with a sterile pipette tip into LB-media, (150 ml) supplemented with kanamycin (50 mg ml^{-1}, 150 μl) and the mixture was incubated overnight (180 rpm, 37 °C).

Kanamycin (50 mg ml^{-1}, 1 ml) and pre-culture (20 ml) were added to each litre of LB-media, and the cells were incubated (37 °C, 180 rpm) until the OD was more than 0.6 but less than 0.7 (approx. 3.5 h). Then a solution of Isopropyl β-D-1-thiogalactopyranoside

(IPTG, 1M, 1 ml) was added to each flask and the mixture was incubated for longer (4 h, 37 °C, 180 rpm). The cells were harvested by centrifugation (7000 rpm, 15 min, 4 °C). The supernatant was discarded and the pellet resuspended on ice, in 25 ml lysis buffer for each litre grown. The lysis buffer was a solution of Tris-HCl (40 mM, pH 8.6), lysozyme (0.1 mg ml^{-1}), DNAse1 (a few milligrams) and complete protease inhibitor cocktail (1 tablet for 2 litres of culture). The cells were lysed by sonication (16 cycles of 15 s spaced 45 s) before being centrifuged (15000 rpm, 30 min, 4 °C). The supernatant was collected and filtered.

As the yield of aBC in LB-media was low, a second protocol was performed and optimised using OvernightExpress media (OE). Kanamycin (50 mg ml^{-1}, 500 μl) and cells from the pre-culture (10 ml) were added to 500 ml batches of OE, to incubate during the day (37 °C, 7 h, 180 rpm) and then overnight (30 °C, 180 rpm). The cells were harvested by centrifugation in a Beckman Avanti J25 centrifuge (Beckman Coulter UK Ltd., High Wycombe, UK) with a JLA-8.1000 rotor for 15 min at 7000 rpm at 4 °C. The supernatant was discarded and the pellet was kept on ice and resuspended in 25 ml lysis buffer for each litre grown. The cells were lysed by sonication (16 cycles of 15 s pulse, 45 s pause) before being centrifuged (15000 rpm, 30 min, 4 °C). The supernatant was collected and dialysed against buffer A (20 mM Tris-HCl at pH 8.6 and 1 mM EDTA).

2.6.3 Purification with anion-exchange and size-exclusion chromatography

Table 2.1 AEC elution gradient used in the purification of aBC.

Elution volume (ml)	Buffer B percentage	Flow rate (ml/min)	Volume of collected fractions (ml)
0	0	4	0
30	0	4	2
80	20	4	2
130	100	4	2
190	100	4	0

The protein was purified by Anion Exchange Chromatography (AEC) using a HiTrap Q HP column (5 × 5 ml, GE Healthcare). The column was equilibrated with 2 column volumes (50 ml) of water, NaCl (2M, 50 ml) and the buffer A. After filtration (0.22 μm pore diameter), the sample was injected onto the column (10 ml/injection) using a 50 ml Superloop (GE Healthcare) and eluted over a gradient of Buffer B (Tris-HCl 20 mM, pH 8.6, EDTA 1 mM

and NaCl 1 M) as shown in Table 2.1. SDS-PAGE analysis was carried out to select the suitable fractions (usually around 24-30) to be concentrated using a Vivaspin 20 concentrator (MWCO 5 kDa, GE Healthcare).

A Superdex 200 PG column (GE Healthcare) was equilibrated with 2 column volumes (CV) (240 ml) of ammonium acetate buffer (200 mM, pH 6.9). The sample was injected onto the column using a 10 ml Superloop (GE Healthcare), eluted over 1 CV (120 ml) and collected in 2 ml fractions. SDS-PAGE analysis allowed the suitable fractions to be pooled and concentrated using a Vivaspin 20 concentrator (MWCO 5 kDa, GE Healthcare). The final concentration of the protein was measured with a Nanodrop 2000 Spectrophotometer (Thermo Scientific) at 280 nm ($\varepsilon_{280} = 19000 cm^{-1}M^{-1}$).

2.6.4 Sample preparation for kinetics experiments

Solutions of monomeric insulin were prepared by dissolving the lyophilised insulin in 50 mM HCl to a concentration of 10 mg ml^{-1}, which corresponds to 1.74 mM. The monomer solution was filtered and diluted with HCl (50 mM) to the desired concentration and supplemented with 40 μM Thioflavin T (ThT) from a 1 mM stock. All samples were prepared in low binding eppendorf tubes and kept on ice before use. Each sample was then pipetted into multiple wells of a 96-well half-area, low-binding, clear bottom and PEG coating plate (Corning 3881), 150 μl per well, in the absence and the presence of different molar-equivalents of aBC, and/or the presence of different equivalents of fibrils. In order to prevent evaporation caused by the high temperature used to promote aggregation, all the unused wells were filled with mQ water and the plate sealed with a foil cover.

2.6.5 Kinetic bulk assays

Assays were initiated by placing the 96-well plate at 60 °C under quiescent conditions in a plate reader (Fluostar Optima, BMGLabtech, Offenburg, Germany). The ThT fluorescence was measured through the bottom of the plate with a 440 nm excitation filter and a 480 nm emission filter. The ThT fluorescence was followed for triplicates of each sample. The data were analysed with the Amylofit web-based software [109].

2.6.6 ThT spectral scan

ThT fluorescence spectral scans were measured with 20 μM ThT in the wavelength range of 470 - 550 nm using a 440 nm excitation filter. The error of the assay was calculated from three independent replicate measurements of the microplate assay.

2.6.7 Transmission Electron Microscopy (TEM)

Samples for TEM were prepared on carbon support film, 400 mesh, 3 mm copper grids (EM Resolutions Ltd., Saffron Walden, UK) and stained with 2% uranyl acetate (w/v). The samples were imaged on a FEI Tecnai G2 transmission electron microscope in the Cambridge Advanced Imaging Centre (CAIC, University of Cambridge, Cambridge, UK). The images were analysed with the ImageJ software.

2.6.8 Microdroplet assays

Insulin aggregation reactions were carried out in microdroplets, by encapsulating water-in-oil-emulsions using a microfluidic device with flow focusing geometry, with the protocol modified from [110]. The different aqueous solutions were injected into the middle inlet on the chip at a flow rate of 200 μl h^{-1}. The carrier oil phase made of fluorinated FC-40 (Sigma) with 4% (w/v) fluorosurfactant FS-008 (Ran Biotechnologies, Beverly MA, USA) was injected into the outer inlet at a flow rate of 300 μl h^{-1} to generate droplets with a radius of $\sim$50 μm. Fluid flow rates were controlled with a Cetoni neMESYS syringe pump (Cetoni GmbH). The microdroplets were collected into Rectangular Borosilicate capillaries (CM Scientific), and the capillaries were sealed with wax plugs to prevent sample evaporation. Before imaging the capillaries containing samples at different fibril dilutions, capillaries were aligned on a glass slide for imaging. The aligned capillaries were placed on the automated motorised stage of a custom-built epifluorescence laser microscope, and covered with a custom-built incubator heated to 60 °C to induce aggregation. The incubator was used in order to observe the position of the droplets over time with brightfield images taken for each timepoint and position, with a brightfield LED light source on top of the incubator. To track aggregate formation within the droplets, fluorescent images were acquired every 15 min for approximately 72 h using laser excitation at 445 nm (diode laser MLD445, Cobolt).

Chapter 3

Development of Immuno Diffusional Sizing

3.1 Introduction

3.1.1 The diffusional sizing method

The diffusive transport of molecules in microfluidic devices has been applied to both the separation and analysis of biomolecules [111–120]. For example, the H-filter [113] can be used to separate large from small molecules according to their diffusion coefficients, but it can also be applied to the analysis of molecular interactions [118]. The diffusional behaviour can be exploited to estimate the hydrodynamic radius R_H, which for a biomolecule can be defined as the radius of a hard spherical particle that diffuses at the same rate as that molecule.

Diffusional sizing can be used to resolve heterogeneous mixtures of proteins by determining the diffusion profile of molecules at different positions of the channel, and comparing it to simulations made for different R_H [111]. Figure 3.1 a shows the microfluidic device design and the reading positions for obtaining the diffusion profiles along the channel. This method can be exploited to calculate binding constants and can be used in complex backgrounds given that the molecule of interest is fluorescently labelled, as in this enhances sensitivity. However, labelling of the analyte is in principle undesireable as the tag may modify the main structure and disturb binding interactions [121, 122]. But diffusional sizing can in principle be performed in a label-free manner, by using the intrinsic fluorescence property of proteins, as long as there is just one protein component present in solution and the concentration is high enough to be detected [97].

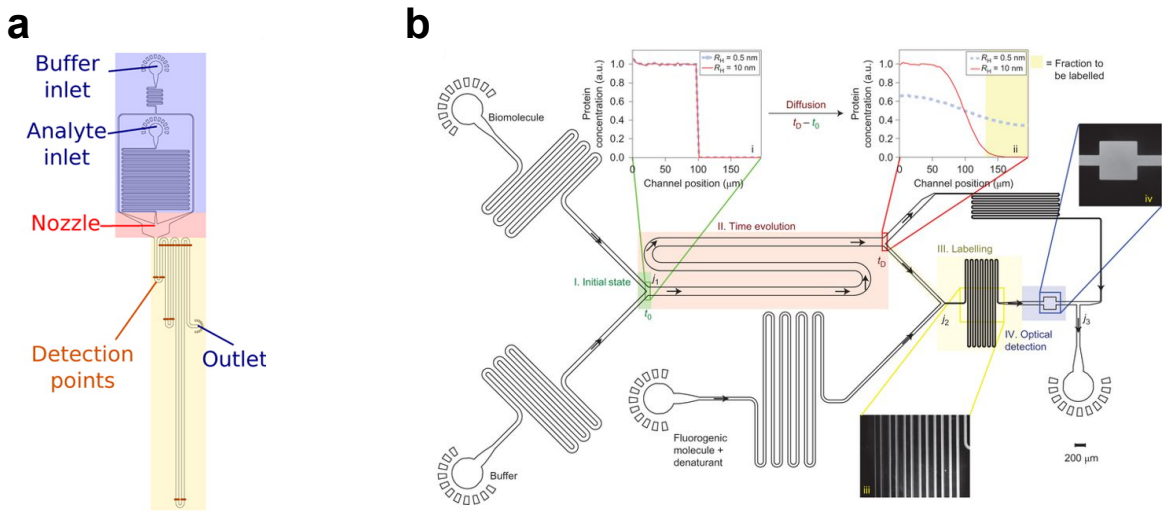

Fig. 3.1 Two different microfluidic diffusional sizing examples. a) The device allows to track the diffusion profiles of particles in space and time, and b) native microfluidic diffusional sizing device, where the biomolecules are separated by diffusion into a stream of buffer, and the label is added just before detection. Reproduced from [111] and [112], respectively.

Another possibility to study proteins in a label-free manner is by addition of the label after separation but just before detection, for example with fluorescence detection after electrophoretic separation [123]. The separation by diffusion followed by fluorescent labelling is known as native microfluidic diffusional sizing (nu-sizing) [112], and the device used in nu-sizing is illustrated in Figure 3.1 b. This method has several applications, such as detection of protein complexes, binding constants and direct measurements of protein unfolding [124]. The labelling is made with orto-phthalaldehyde (OPA) which reacts with primary amines and thiols in aqueous alkaline medium to form fluorescent adducts [125, 126]. The use of OPA therefore limits this method for solutions of one protein component only, as the reaction is not specific and would target all primary amines, including those present in some buffers like tris. The method requires the addition of a denaturing component to the labelling mixture in order to guarantee that all the primary amine groups are exposed, making the labelling quantitative. The fraction of diffused protein obtained experimentally is compared to the one obtained with simulations, termed basis functions [127] to estimate the hydrodynamic radius of the protein of study.

Another application example of diffusional transport is its use to separate aSyn fibrils (large particles) from monomers (small particles) [120]. The device, shown in Figure 3.2 a, originally used to monitor the binding of small molecules to amyloid fibrils, works by injecting the protein stream in the middle and buffer on the sides. In the microfluidic channel, the particles in the sample stream can mix with the auxiliary buffer only by diffusion.

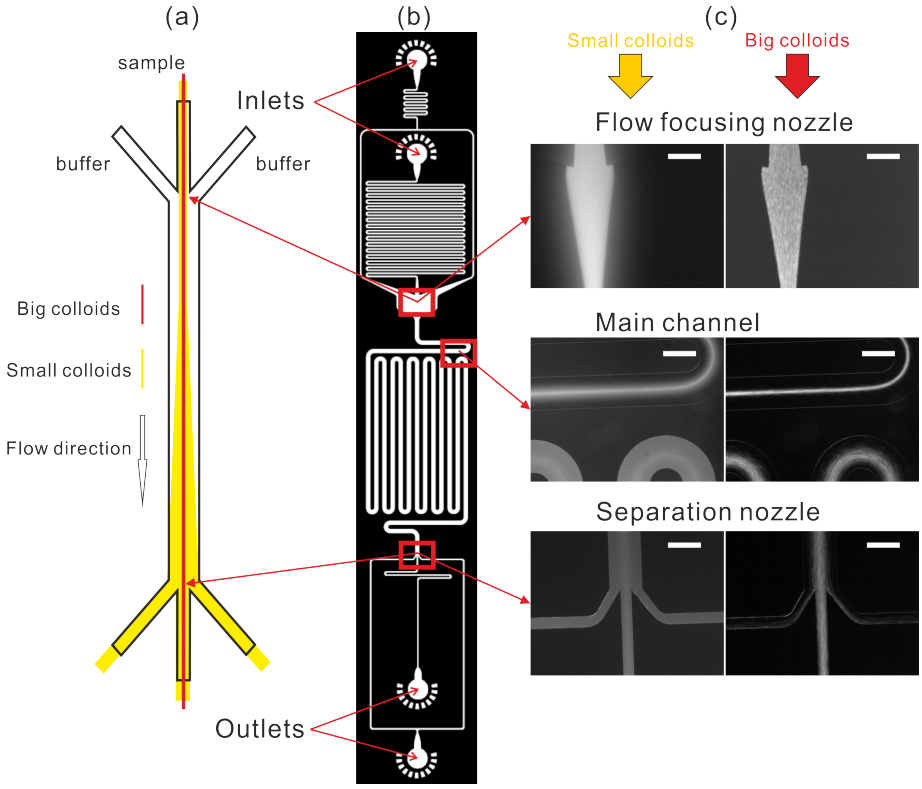

Fig. 3.2 Illustration of the microfluidic diffusional separation used in the first experiments of IDS. a) The sample is injected in the middle and auxiliary buffer on the sides, which run side by side in the diffusion channel and are separated again in the end. b) AutoCAD design of the device and c) images of fluorescently-labelled small and large colloids, at the different positions in the device. Reproduced from [120].

Figure 3.2 c shows the aSyn monomers and fibrils at different positions of the device. At the end of the diffusion channel, the monomers have completely diffused, while the fibrils remain in the central stream, due the their smaller diffusion coefficient.

The technique of fluorescence resonance energy transfer (FRET), involves a donor fluorophore in an excited electronic state, which transfers its excitation energy to an acceptor fluorophore when they are in close proximity ($<$10 nm) through a non-radiative process [128]. In this study, the diffusional sizing technique has been coupled to immunoassay detection, which, do to the use of antibodies, makes the detection of the protein being sized highly specific. Time-resolved FRET (TR-FRET) [129] uses separately labelled antibodies with FRET donor and acceptor fluorophores. In the context of microfluidic technology, a TR-FRET immunoassay could be a potential detection method as some of its characteristics make it a suitable candidate for on-chip measurements.

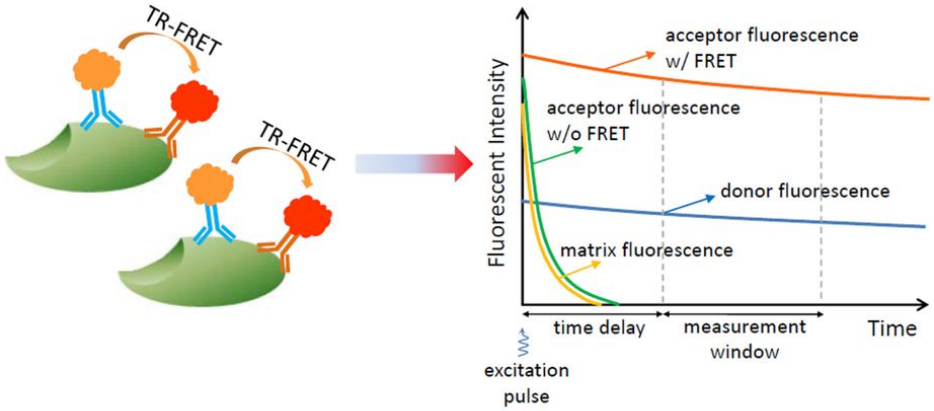

Fig. 3.3 Schematic description of TR-FRET assays. Left: FRET donor and acceptor labelled antibodies come in close proximity upon binding to the same molecule, which enables FRET between the fluorophores conjugated to the antibodies. The excitation is a single pulse and the FRET signal is read in a time-resolved manner to eliminate the background fluorescence. Reproduced from [130].

3.1.2 Time-Resolved FRET

An obvious improvement to the nu-sizing method would be the addition of a specific label that is innactive without the target, as this would allow the detection of proteins in complex mixtures. Here, the method of choice for specific detection was the use of immunoassays, in particular the time-resolved FRET (TR-FRET) immunoassay as it is a 1-step homogeneous assay, which offers the possibility to be performed on-chip. Homogeneous Time Resolved FRET (HTRF) [129] technology usually works with sandwiching antibodies, each of them labelled with a FRET-donor and the other with a FRET-acceptor. The formation of the immunocomplex brings the FRET pair into close proximity, and the intensity of the FRET signal is directly correlated to the concentration of the analyte. The measurement is conducted in a time-resolved way to eliminate any non-specific fluorescent signal from the background, which enables sizing in complex biological samples without prior purification of the protein or protein oligomeric species.

Time-resolved measurements are performed for the reason that FRET signals are influenced by the fluorescence of the sample background. Therefore TR-FRET uses a rare earth chelate as donor due to their long-lived fluorescent signals upon excitation by an energy pulse [130] as shown in Figure 3.3. The excitation pulse is in the order of microseconds and thus the background signal decays rapidly, and the detection of the FRET dependent signal is measured after a time-delay, within a time window.

TR-FRET technology has multiple advantages over traditional immunoassays such as enzyme-linked immunosorbent assay (ELISA), which is usually time-consuming and requires

surface immobilisation and multiple washing steps that makes it quite complicated to adapt into a microfluidic device. TR-FRET combines homogeneity, great signal stability and high specificity with low-background interference [131]. Its multiple advantages confers this technology great potential for its use with different body fluids such as CSF, blood, serum, plasma, and saliva. However, as all immunoassays it has some drawbacks, for example the limitation in dynamic range caused by the high-dose *Hook* effect. In systems where the analyte concentration range is large, antigen concentration can go into excess, and both free and bound analyte compete for the limited antibody binding sites, when the antibody pair is added simultaneously [132]. This effect can be adverted by performing the assay with multiple sample dilutions. Another limitation of TR-FRET assays is the detection of binding distance up to 9 nm [133] due to FRET efficiency that decreases with increasing distance [134].

3.2 Aims

The aim of this chapter is to provide an overview of the development and optimisation of the device used for Immuno Diffusional Sizing (IDS). All the experiments mentioned in this and the following two chapters, are for a device where diffusion happens on-chip, but all immunoassays are made in bulk. The attemps to create a device for on-chip detection are mentioned in Chapter 5.

3.3 Results and discussion

3.3.1 First generation device for Immuno Diffusional Sizing

Insulin is found as a zinc-coordinated hexamer under physiological conditions, but in the absence of zinc it is found as a dimer [135]. Monomers, the active form of insulin, are predominant under acidic conditions [136]. The oligomeric states of insulin can be manipulated through changes in the pH and the addition of various additives such as Zn^{2+}, and thus it was chosen as the model protein for diffusional sizing. The preliminary experiments of the diffusional sizing post-separation were conducted with the device designed to separate fibrils from monomers [120], shown in Figure 3.4 a. The device, works by injecting the protein stream in the middle and auxiliary buffer on the sides, at a flow rate ratio of 1:10. At the end of the diffusion channel (l = 9 cm, w= 300 μm), it is split into three equal parts (w= 100 μm) to collect the centre as a fraction non-diffused (f_{nd}) and the two sides as a separated

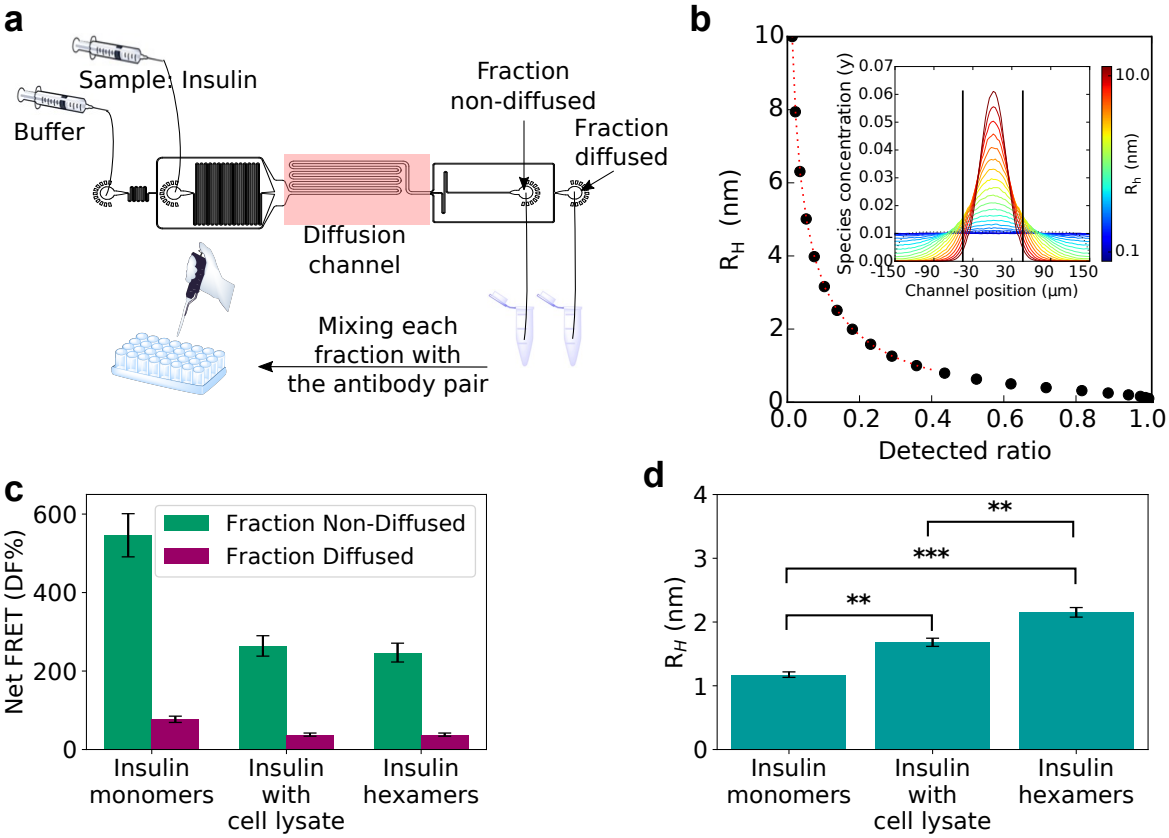

Fig. 3.4 Schematic description of the IDS method using the first generation device. a) Design of the device indicating the protein and auxiliary buffer inlets, diffusion channel and outlets that separate the fractions diffused and non-diffused, for their analysis with the TR-FRET on a platereader. b) Concentration profiles for reference species of known size obtained with simulations [127], observed laterally from across the end of the diffusion channel. c) The Net FRET signal of the separated fractions for insulin monomer, insulin in the presence of cell lysate and the insulin hexamer. The error bars show the standard deviation of triplicate TR-FRET measurements of each sample. The net FRET values are converted to concentration with a TR-FRET standard curve, and divided to calculate the detected ratio ($\frac{f_d}{f_{nd}}$). d) The corresponding hydrodynamic radius after interpolation of the experimental detected ratio to the basis functions in b. Values in bar graph represent mean $\pm$ SD of $n = 3$ experiments performed with different devices. One-way ANOVA $P = 0.0001$, followed by Tukey's HSD test $^{**}P < 0.002$, $^{***}P < 0.0002$.

fraction diffused (f_d). Therefore, proof-of-principle experiments for immunodetection after separation by diffusion were performed with this design, with the model protein insulin. Both fractions at the outlet were collected separately, and the detection with TR-FRET was performed in bulk, by mixing the fractions with the antibodies on a microwell plate and readings were taken on a platereader. The Net FRET (DF%) for each of the separated fractions reflects the signal to background of the assay

$$\mathrm{DF\%} = \frac{R_{Sample} - R_{\text{Neg control}}}{R_{\text{Neg control}}} \times 100, \tag{3.1}$$

where R_{Sample} or $R_{\text{Neg control}}$ are an average of the ratio of the signal calculated for each individual well, measured at two different wavelengths (620 nm and 665 nm) which normalises the signal [129]:

$$R = \frac{Signal_{665nm}}{Signal_{620nm}} \times 10^4. \tag{3.2}$$

Figure 3.4 c shows the net FRET signal of each of the fractions f_{nd} and f_d, for monomeric insulin pure and with cell lysate, and the insulin hexamer. These signals are converted to concentration with a TR-FRET standard curve, to calculate the experimental “detected ratio”. This value is extrapolated to its corresponding hydrodynamic radius, with the simulated concentration profiles of a range of particle sizes, shown in Figure 3.4 b.

The method presented here, which I named Immuno Diffusional Sizing, does not require the use of fluorescently-labelled proteins, since the detection is made only after the protein is diffusional-separated in the microchip (Figure 3.4 a). The TR-FRET provides then the concentration of protein non-diffused and diffused (to the auxiliary buffer) as indicated in Figure 3.4 c, or the experimental “detected ratio”. Finally, in order to estimate the protein size, the “detected ratio" is extrapolated to its corresponding hydrodynamic radius with the basis functions, simulations of the diffusion profiles for different particles of known size (Figure 3.4 b).

The monomeric insulin test was carried out by running the device at 600 μl/h, flow rate that worked well for small proteins. The size of monomeric insulin at a concentration of 22 nM and at pH 2 (1.17 $\pm$ 0.04 nm) was consistent with the previously reported size of 1.3 nm [137] but the error in the size measurement (3.4%) would not allow the distinguishment of species close in size, such as monomer from dimer. The sizing of the insulin monomers in a complex mixture was also made by spiking it into 1% cell lysate, leading to the a size (1.68 $\pm$ 0.06 nm) that may reflect a mixture of monomers, dimers and hexamers, as illustrated in Figure 3.4 b. The mixture of species could be causd by the additives present in the cell lysate

mixture. IDS was suitable to size the insulin hexamer (2.15 ± 0.07 nm) by stabilising it in the presence of Zn^{2+} at a high concentration of insulin (70 μM) [100]. However, when attempts to size higher molecular weight proteins were conducted, the device was not appropriate leading to large errors among repeats.

One of the main limitations of the design was that there was no way to observe that the flow rate of the protein remained centred in each and every device, as all the measurements were conducted in a label-free manner. Sometimes the instabilities were caused by bubbles present at the nozzle, but bubbles could be detected with a brightfield microscope. If there was an irregularity on the glass or PDMS, which caused the flow to be modified, it was only detected after doing the TR-FRET measurement as it seemed that there was more protein in the f_d than in the f_{nd}. The other main problem was that the use of the 1:10 flow rate ratio of protein to buffer caused fluctuations in the protein flow rate when low flow rates were used. In this device, the analyte and the auxiliary fluid were loaded into syringes and the solution flow rate was controlled by applying a positive pressure with two syringe pumps, the fluctuations depend on the two pumps.

An alternative to the problem was to switch to the withdrawing mode rather than the pulling. Usually, the pulling mode is preferred not only because the fluctuations in the flow rate are less than in pushing mode, but also because it requires less sample volume and only one pump to control the whole device. Nevertheless, as the detection with TR-FRET was performed off-chip, it was still necessary to collect the two separated fractions from the outlets. One alternative to solve this limitation was to use a "pulling-adaptor", but this had several drawbacks as with such a device it would have been complicated to collect the separated fractions from the outlets. Therefore, a complete change to the separation device was performed, making specific changes as shown in Figure 3.5 to make it suitable for sizing small and large particles.

3.3.2 Physical considerations

Figure 3.5 shows a schematic description of the main changes introduced to the diffusional separation device in order to optimise it for IDS. Among the main considerations made for the new design was the fact that the samples in the diffusion channel were label-free, therefore a geometry like the traditional H-filter [113] was chosen because it is the simplest configuration. Unlike the old design, where the buffer separates in two streams that run on the sides of the protein one, in the H-filter there are only two streams that move in parallel.

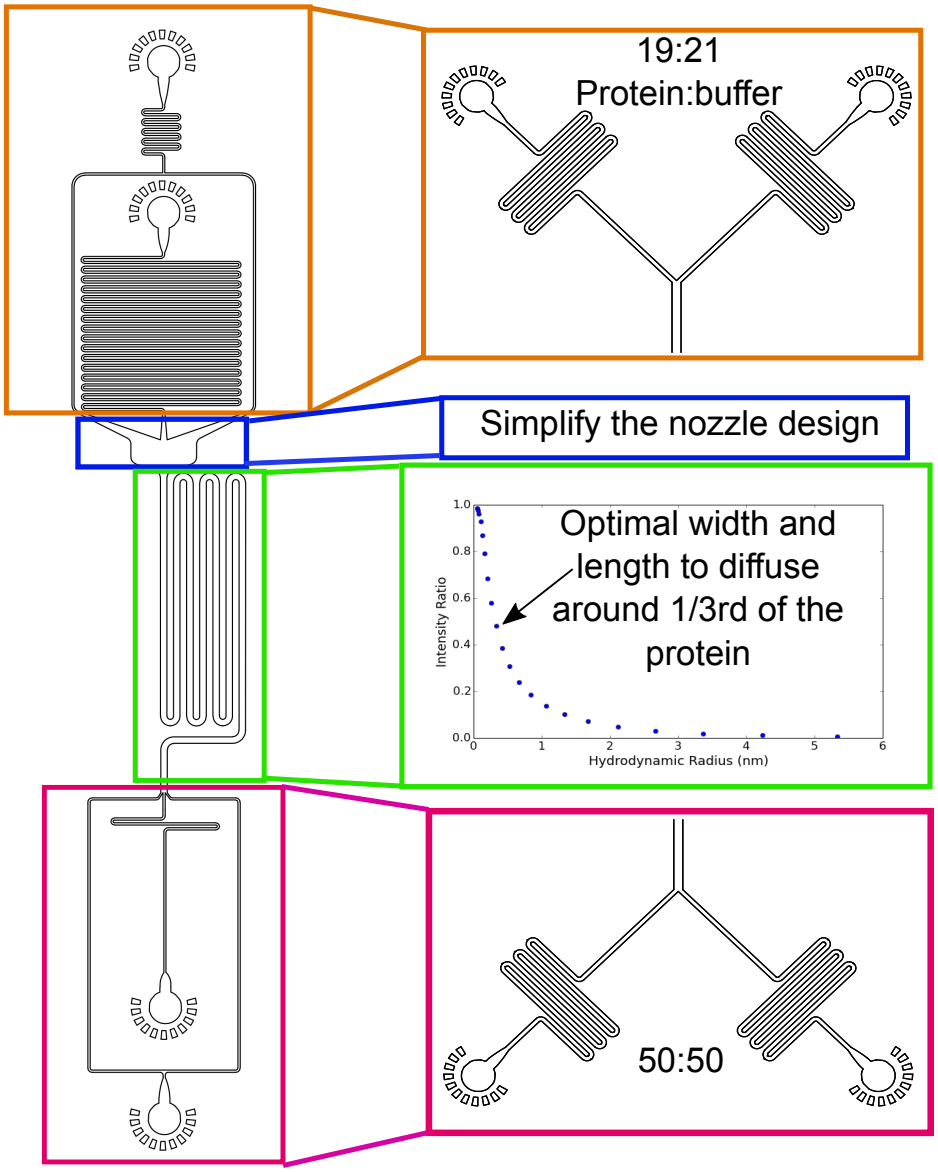

Fig. 3.5 Schematic description of the changes introduced to the diffusional separation device for optimisation. The inlets were changed to a geometry of 19:21 to avoid the errors caused by the flow fluctuations. The nozzle was simplified to reduced the possibility of bubbles. The main diffusion channel was adapted to have a fraction diffused of 1/3rd of the total protein, or $\frac{f_d}{f_{nd}=0.5}$. An intensity ratio of 0.5 ± 0.1 does not affect the value of the calculated hydrodynamic radius (0.34 ± 0.07 nm). In the contrary, at intensity ratios below 0.1, small changes affect the size of the radius drastically, which can lead to errors in the size estimation. The outlets were simplified to a geometry of 50:50.

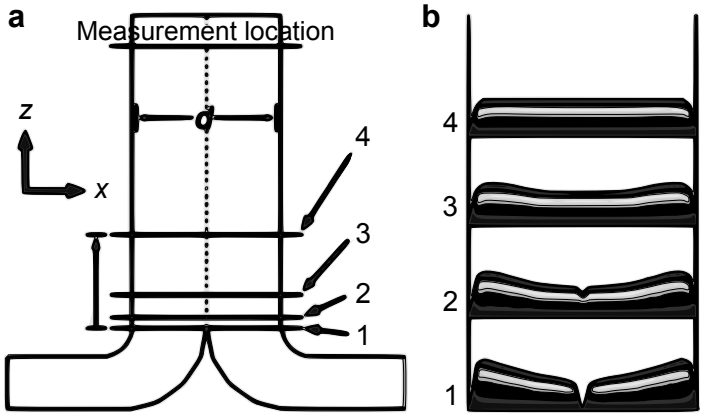

Fig. 3.6 Three-dimensional simulations of the velocity profiles at four different positions in a T-sensor indicated in A. Simulations were conducted over a large range of flow rates from 41.7 nl/s and 1 μl/s, and in all cases the velocity profiles, shown in B, had the same shape and relative magnitud. Velocity is fully developed to 99% at 1423 μm. Adapted from [115].

The nozzle was also modified to make it simpler. The original design was wider and usually several air bubbles were trapped on it; the main problem was the stream not being perfectly centred because of small imperfections in the nozzle. Simulations of flow in previous studies [115] showed that the velocity at the junction where the two inlet channels meet was zero, but it increased rapidly until flow was fully developed (99% at a distance of 1.4 cm) as shown in Figure 3.6. Since in all of our experiments the measurements were collected at a distance of at least 10 cm, the nozzle should not make a difference.

The optimal length of the device was selected by considering that ideally $\frac{f_d}{f_{nd}} = 0.5$, this means 1/3rd of the total protein should be diffused at the end of the channel. As indicated in Figure 3.5, an intensity ratio of 0.5 ± 0.1 does not change the value of the calculated hydrodynamic radius. In the contrary, at intensity ratios below 0.1, small changes affect the size of the radius drastically, which can lead to errors in the size estimation. The diffusion coefficient is defined by the Stokes-Einstein equation:

$$D = \frac{k_B T}{6\pi\eta R_H} \tag{3.3}$$

Where k_B is the Boltzmann constant, T is the temperature in K, η is the viscosity of the fluid and R_H is the hydrodynamic radius of the particle. The displacement along the x-axis (width, in this case) over which the concentration distribution softens is of the order of the square root of 2Dt [138, 139], as illustrated in Figure 3.7. This means that

$$\sigma = \sqrt{2Dt} \tag{3.4}$$

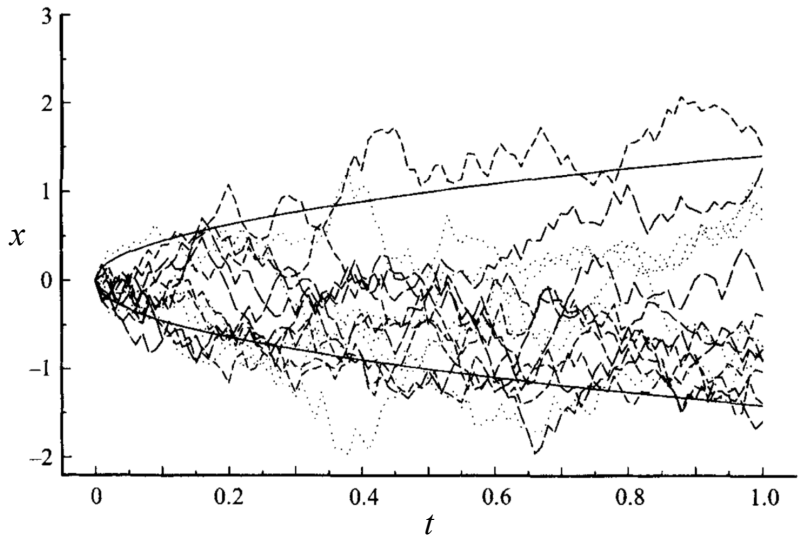

Fig. 3.7 Simulations of fifteen random walks $x(t)$, with origin and $t = 0$ and $x = 0$ with diffusivity $D = 1$. The continuous curves are $\pm\sqrt{2Dt}$. Reproduced from [138].

where σ is the width of the function, D is the diffusion coefficient and t is the time. The time at which the particle is at the end of the diffusion channel is the residence time, which could be estimated through

$$t = \frac{lhw_c}{Q}, \tag{3.5}$$

where l is the channel length, h is the channel height, w_c is the channel width and Q is the flow rate. For particles diffusing up to at least half the width of the buffer stream, that represents $\sigma = \frac{w_c}{4}$. By adding this expression to equation 3.4

$$\frac{w_c^2}{16} = 2Dt. \tag{3.6}$$

By substitution of the residence time (eq. 3.5) in equation 3.6, and re-arranging the terms:

$$l = \frac{Qw_c}{32Dh} \tag{3.7}$$

Equation 3.7 can be used to estimate the optimal length for diffusing particles from the sample stream up to at least half the width of the buffer stream. Considering a particle of 1.5 nm radius, a channel height of usually 25 μm, a flow rate of 200 μl/h and a width of 200 μm, the total length of the channel would be of 103 mm. For a particle of 10 nm radius, with the same device dimensions and flow rate, the optimal length would be of 685 mm. Since the channel would be too long, a possibility is to make the channel width smaller, to 80 μm,

flow at a lower rate, and then the channel length results in 109 mm. These measures are reasonable for a device, and therefore two main designs were used with different widths, 80 μm and 200 μm width, each of them of 10 cm length and 25 μm height, with the 80 μm being optimal to diffuse a particle of 10 nm radius to at least $\frac{w}{4}$, i.e. 30%.

The inlet was designed to be in a ratio of 19:21 protein buffer. The slight change in the volume ratio was to avoid the errors produced by the fluctuations in the flow if the initial state was at 50:50 exactly. The outlets were at a ratio of 50:50. The length of the inlets and the outlets were designed to produce a resistance of the order of the diffusion channel. The resistance in microfluidic networks can be calculated as analogous to electrical circuits [140]. The pressure drop Δp through a finite channel of length L can be calculated with the following expression:

$$Q = \frac{\Delta p}{r_H}, \tag{3.8}$$

where r_H is the hydraulic resistance $[Pa/(m^3/s)]$, and Q is the total volumetric flow rate $[m^3 s^{-1}]$ [140]. Equation 3.8 is the Hagen–Poiseuille's law simplified, and it relates the pressure drop to the hydraulic resistance that for a circular channel with a radius R and fluid viscosity η with the following expression:

$$r_H = \frac{8\eta L}{\pi R^4}. \tag{3.9}$$

Equation 3.9 can also be applied to rectangular channels, which is the case for most of the microfluidic channels. An approximation can be used for high aspect ratio geometry (e.g $h/w \ll 1$) and the hydraulic resistance can be approximated as:

$$r_H = \frac{12\eta L}{wh^3} \tag{3.10}$$

Combining equations 3.8 and 3.10, the pressure difference in a rectangular channel can be estimated as:

$$\Delta p = Q\frac{12\eta L}{wh^3} \tag{3.11}$$

Where η is the viscosity given in $[Pa/s]$. For a more precise approximation, a geometry factor can be added to equation 3.11 and modified to:

$$\Delta p = Q\frac{12\eta L}{wh^3(1-0.630\frac{h}{w})} \tag{3.12}$$

Equation 3.12 is valid only when $h < w$. This expression was used to estimate the length of the inlets and outlets of the devices, in order to have a Δp in the same order of magnitude as the diffusion channel.

3.3.3 Final design and testing

Figure 3.8 shows a schematic of the IDS method and the two devices used in this study. Multiple devices were tested but the preferred length was 10 cm and the difference is the channel width. In the experiments described in Chapters 3 and 4, the detection of the diffused and non-diffused fractions was performed in bulk after collection of the samples in the outlets. For all the proteins, preliminary experiments were conducted with each of the devices (Figure 3.8 b and d). Usually, a detected ratio smaller than 0.1 is in undesirable, because below this value the slope of the curve becomes to steep, which means that a very small change in detected ratio is a big change in size and this leads to large errors in the measurements. The basis functions in Figure 3.8 c show that the 200 μm device run at 200 μl/h is suitable for small particles of less than 6 nm radius. The 80 μm device (Figure 3.8 d) is more suitable for larger particles, as it can be seen in the basis functions for this device at a flow rate of 80 μl/h (Figure 3.8 e). When conducting experiments with proteins, an experiment with the 80 μm device confirmed if the particle was large or small, since the small particles were completely diffused at the end of the diffusion channel.

The height of the channels was measured with a profilometer and the exact height (usually 25 ± 5 μm) was adjusted in the basis functions for a more precise fitting of the hydrodynamic radius. The flow rate at the outlets of the device was measured with Elveflow® flow sensors to determine the volume ratio at the outlet of the channels. Figure 3.9 shows the calibration curve of the flow rate measured against the one in the pumps. The graphics show the flow rate measured at each of the outlets and the independent variable is the total flow controlled by the nemesys pumps. The slope is the actual fraction of volume. We can see that the values are not exactly 50:50, but with a small difference. The calibration was performed only once and these values were adjusted in the the basis functions code, for a more precise fit value. The calibration with the flow sensors also showed that a flow rate only stabilises after 6 minutes, and therefore for each of the experiments collection only started after 10 minutes of selecting the flow rate with the nemesys pumps. This waiting time allows not only flow rate stabilisation but also it allows the BSA (bovine serum albumin) present in the buffer to coat all the PDMS channel and prevent non-specific binding of the target protein.

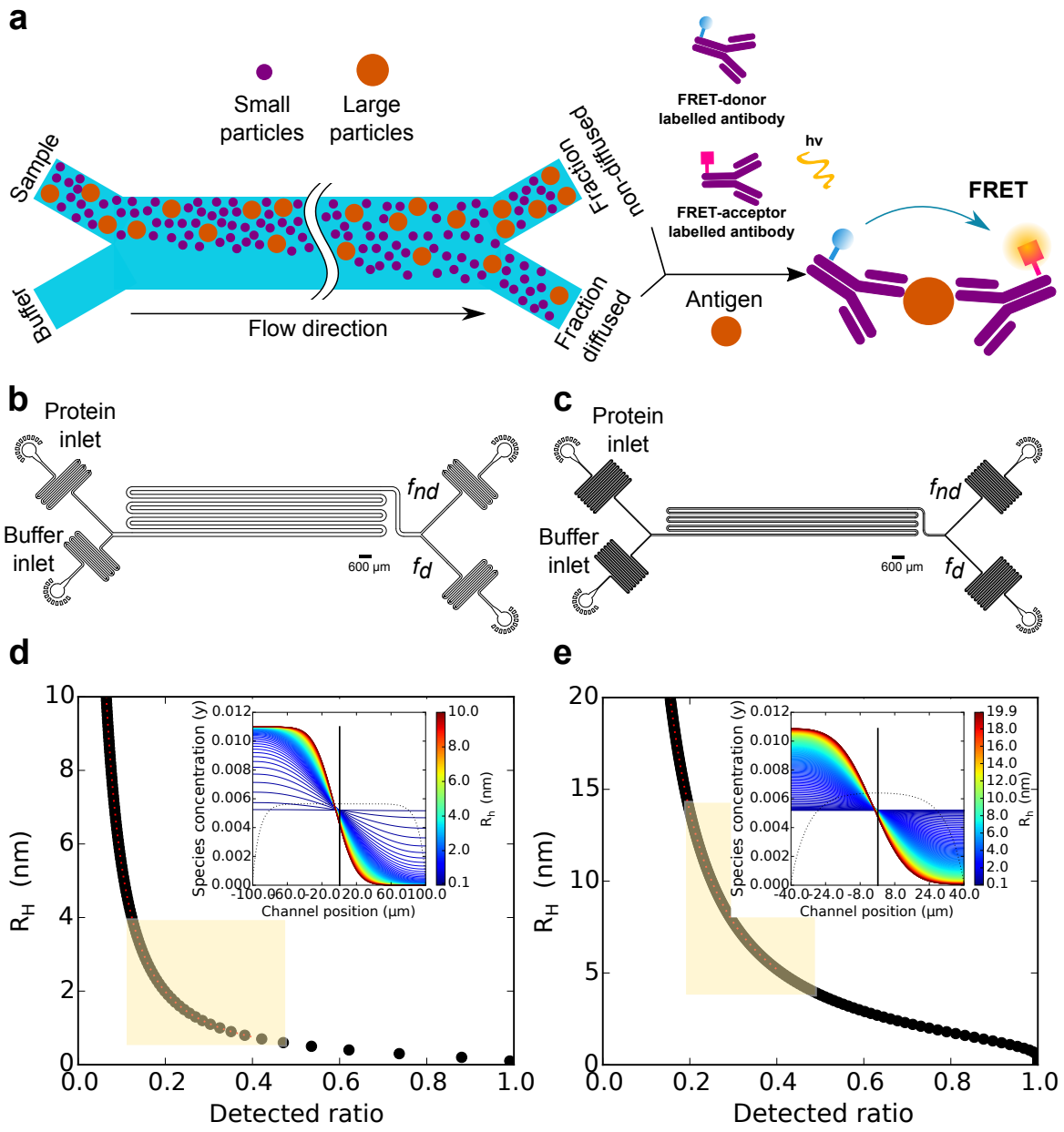

Fig. 3.8 Final designs of the devices used for IDS. a) Schematic description of the Immuno Diffusional Sizing method. The protein is injected into one inlet and buffer into the other at a flow rate ratio of 19:21. The streams meet at the junction and due to laminar flow they run side by side through the channel. At the end of the diffusion channel the streams are split into two equal parts (50:50) and both fractions (f_d and f_nd) are collected separately for analysis. The diffused and non-diffused fractions are analysed separately with a sandwich immunoassay in order to quantify the protein of interest. b) The 200 μm width device is optimal to use for small particles, while c) the 80 μm width device is optimal to use for larger particles. c) The basis functions for the 200 μm device at 200 μl/h, and e) the basis functions for the 80 μm device at 80 μl/h. The yellow area indicates the optimal size ranges to avoid large errors when the slope $\frac{\Delta R_h}{\Delta Ratio}$ becomes too steep or flat.

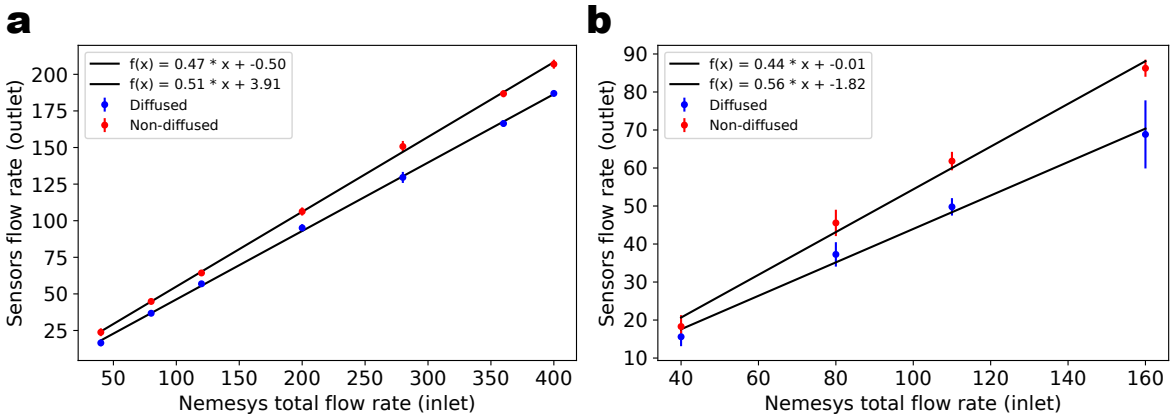

Fig. 3.9 Flow rate calibration at the outlet channels. The slope of the graphic represents the variation of the flow as a function of the inlet flow controlled with the pumps, which is the real fraction of the outlets. a) Data and fitting of the 200 μm width device outlets and b) the 80 μm width device outlets.

The flow rate profile at the nozzle was tested with fluorescent colloids of 25 nm radius, as shown in Figure 3.10. The images show that the flow in the beginning is well-defined so this nozzle geometry is the preferred one, as it allows a faster equilibration and air bubbles are eliminated easier. This test was also performed to observe the behaviour of the flow rate over time, mainly because these experiments usually run for long periods of usually half an hour up to even two hours, where it is important that the flow remains relatively stable. Figure 3.10 shows the change in the separation position of the two strems (fluorescent colloids and water) over time. Over 70 minutes, the separation position of the 80 μm device is in average 38.08 $\pm$ 0.25 μm, while the one of the 200 μm device is 95.6 $\pm$ 1.15 μm. But this fluctuation should not affect the separation outlet, which is at 40 μm and 100 μm, designed like that precisely to avoid the errors at the inlet. A final test with monomeric insulin was conducted with the new device design (200 μm width at 400 μl/h) and the resulting size was 1.24 $\pm$ 0.22 nm which is in good agreement with the reported size of 1.3 nm [141].

In this project, some of the experiments with the prions (Chapter 4) were conducted in a biosafety laboratory, therefore the method was optimised with conditions suitable to work with infectious material and under a biosafety cabinet. But a possibility to reduce the errors in the measurements would be by the use of a pressure-driven flow instead of the syringe pumps, as the pressure driven system is typically more stable and the pumps cause fluctuations in the flow [142].

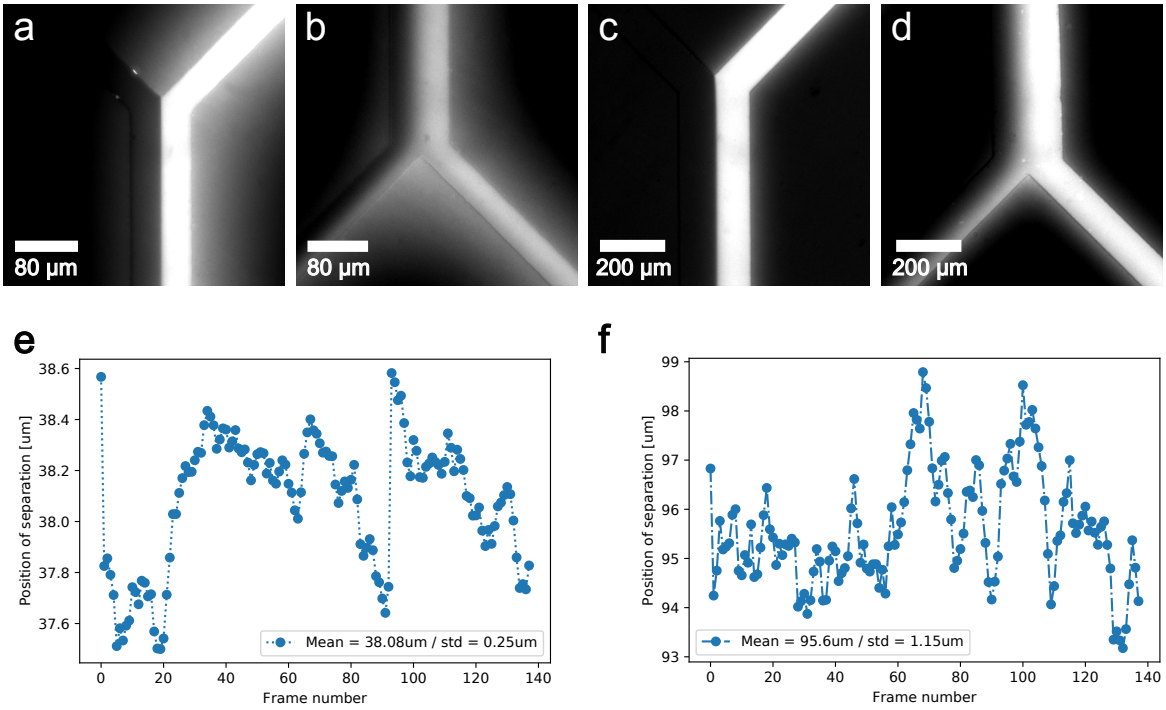

Fig. 3.10 Fluorescent images of the flow with pushing mode at 80 μl/h at the 80 μm width channel a) inlet and b) outlet of the 10 cm length device, and the 200 μm width channel c) inlet and d) outlet. The sample in the protein channel are fluorescent colloids of 25 nm radius, run against mQ water. Images were acquired every 5 min, and the fluctuations in the flow affect the separation position of the streams. e) Flow stability at the nozzle of the 80 μm width device and f) the 200 μm width device.

3.4 Conclusions

During this project I have optimised the diffusion device design for its use with immunoassays. The main changes resulted in a simpler geometry with the width and length optimised to work with either small or large particles. The H-filter geometry allows the use of this device in a label-free environment and smaller errors caused by fluctuations in the flow. Nevertheless, this device has great potential to be coupled with other detection techniques that would otherwise be difficult to adapt for on-chip detection, for example mass-spectrometry. The fraction-collection makes it suitable to adapt to non-homogeneous immunoassays, such as sandwich ELISA. The following Chapter describes the applications of the method presented here for its use with prions and amyloidogenic oligomers.

Detection with fluorescently-labelled antibodies has great advantages over other techniques. It provides great sensitivity and specificity. In order to reduce the errors related to the time-dependency of the FRET signal, a standard curve was measured simultaneously with the separated fractions. Furthermore, to avoid errors and false negatives of the “hook-effect”,

the highest concentration of protein injected into the device was chosen to be the highest possible in the standard curve, after which the FRET signal decreases. For biological samples, it is recommended to make multiple serial dilutions of each of the fractions to avoid false negatives when an excess analyte concentration is present.

Chapter 4

Size analysis of prion proteins and amyloidogenic oligomers with IDS

The content of this Chapter is based on a manuscript in preparation for submission to Nature Methods: "Direct Size Determination of Prions and Amyloidogenic Oligomers".

This chapter is divided in two parts, the first one describes the application of IDS to prion proteins, and the second one focuses on the application to amyloidogenic proteins.

4.1 Part I: The prion protein

Prion diseases or transmissible spongiform encephalopathies (TSEs) are a group of neurodegenerative disorders that belong to the Protein Misfolding Diseases (PMDs), with the main difference of being infectious. While some people have claimed that proteins like Aβ in Alzheimer's disease and aSyn in Parkinson have prion-like properties, their infectivity has not yet been demonstrated [143]. TSEs involve the accumulation of aggregated forms of the prion protein (PrP). The term "prion", derived from "protein + infection" was coined by Stanley Prusiner in 1982, after isolating the minimal infectious unit that is required to spread scrapie among sheep, and finding that is composed of PrP only [144]. PrP exists as PrP^{C} (cellular) in non-infected hosts, and as PrP^{Sc} (Scrapie) as the major component of the scrapie infectious agent. The human forms of prion disease are Creuztfeldt-Jakob disease (CJD), fatal familial insomnia (FFI), German-Straussler-Scheinker (GSS) syndrome, kuru and variably protease sensitive prionopathy (VPSPr). They arise sporadically, genetically or be acquired, with the latter accounting for only 5% of the cases of human prion disease [145].

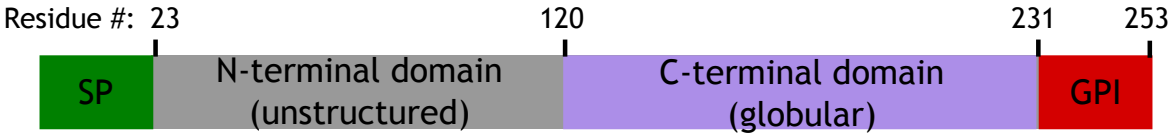

Fig. 4.1 Schematic description of the structural domains of PrP. The protein, after transcription is 253 amino acids in length and includes a signal peptide (SP) that is cleaved and the 232-253 fragment is replaced by a glycosyl anchor GPI (glycophosphatidylinositol). Adapted from [146].

4.1.1 The structure and function of PrP

PrP is a cell-surface mammalian protein synthesised in the central nervous system (CNS) and various non-cerebral tissues, such as blood lymphocites, muscle, heart, kidney, and the digestive tract [147]. PrP is encoded as a 253 amino acid protein, but the final processed form contains amino acids 23-231. The peptide 1-22 is cleaved as a signal peptide and the 232-253 fragment is replaced by a glycosylphosphatidylinositol (GPI)-anchor [148]. Native PrP is isolated as a mixture of unglycosylated, mono-glycosylated and with two glycosyl groups. The "protein-only" hypothesis [149, 150] proposes that TSEs are caused by the misfolding of PrP^{C} into the scrapie form PrP^{Sc}.

The recombinant human PrP, hPrP 23-230, is formed by a globular domain and an N-terminal disordered tail [101]. The globular domain contains a disordered loop, 3 alpha-helices and a short anti-parallel beta-sheet. The disordered loop (167-171) is shared with the murine PrP (mPrP). The small differences in the structure of PrP among different species may provide insights for the species barrier of the infectivity.

The physiological function of PrP^{C} is still unknown, but because its structure is highly conserved in mammals it is thought that its role exerts beneficial functions [151]. To understand its role, different controlled animal models were created and the first one were knockout mice that lack the PrnP gene, Zurich 1 (or ZH1 $PrnP^{0/0}$). However, no significant abnormality was found except resistance to prion infection and a small alteration in behaviour. A latter study showed that the PrnP knockout mice had deficiencies in memory and spatial learning. Other possible functions suggested for PrP are its role in the regulation of sleep, modulation of synaptic mechanisms and neuronal excitability, as well as a possible role in embryonic development and as neuroprotector in acute cerebral ischemia and against aβ oligomers toxicity.

4.1.2 The structure of PrP^{Sc}

The protein-only hypothesis states that the transmissible agent of prion diseases is composed of misfolded PrP only, and lacks nucleic acid [152]. The evidence shows that the infectious agent is resistant to UV and ionizing radiation, which normally destroy nucleic acids. However, the ultimate proof for this hypothesis, i.e. the generation of PrP^{Sc} in vitro, is still missing. Originally the term PrP^{Sc} was directly related to the protease resistant fraction, as infectivity as well as concentration are dependent on digestion conditions. The isolation of the protease-resistant form (PrP^{res}) which copurifies with infectivity, is perhaps the strongest evidence that supports the prion-only hypothesis. The virino hypothesis is one of the alternatives to the prion-only, and suggests that the transmissible agent is a small informational molecule encapsulated on a tight protein coat [153]. But this hypothesis is not really widely accepted. The main problem to address the prion problem is that the precise structure of the transmissible prion is not yet completely known. The main challenge to resolve the complete structure is the difficulty to maintain PrP^{Sc} infectivity throughout purification. Another challenge is the lack of solubility of the PrP aggregates, which makes it difficult to study with NMR or X-Ray crystallography.

Unlike PrP^{C}, PrP^{Sc} is characterised by a high beta-sheet content. Electron cryomicroscopy (cryo-EM) has provided insights into the structure of brain-derived GPI-anchorless PrP^{Sc} [154]. The structure of infectious prion from mice expressing GPI-anchorless PrP shows a four-rung β-solenoid as its key feature, and fibril segments with a repeating unit of 1.91 nm. Micro electron diffraction (MicroED), a cryo-EM method, reveals a bank vole prion protofibril with amyloid-like features [74]. MicroED shows that a 3D network of hydrogen bonds and stacked aromatic residues stabilise the structure of proto-PrP^{Sc}.

4.1.3 Prion protein antibodies

The Aguzzi lab (Institute of Neuropathology,University of Zürich, Switzerland) has created a variety of antibodies specific for different epitopes of PrP^{C} [104] by immunisation of $PrnP^{0/0}$ knockout mice with recombinant mPrP. The monoclonal antibodies, named POM1 to POM19, are specific to several epitopes of PrP^{C}, including the N-terminal region, as shown in Figure 4.2.

Although the development of prion antibodies emerged as a possible therapeutic against prion diseases, studies with the POM antibodies have shown that the antibodies that bind to the globular domain of PrP induce neurotoxicity [155]. This suggested that the flexible tail transmits the toxic signals that trigger oxidative stress and calpain activation.

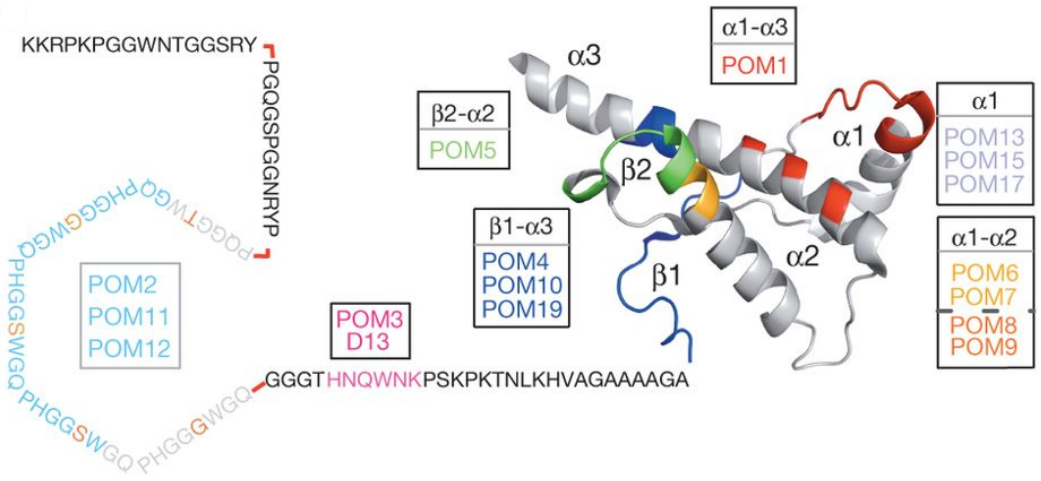

Fig. 4.2 POM antibodies and their binding sites to PrP(23-230). The antibodies selected for these studies were POM1 and POM19. Reproduced from [155].

4.2 Results and discussion

All prion experiments were performed in the Institute of Neuropathology, University of Zürich. The experiments involving Rocky Mountain Laboratory strain mouse-adapted scrapie prions (RML-infected) brains were performed in biosafety laboratories at level 2 or 3.

4.2.1 Selection of the FRET antibody pair

The application of IDS to the study of prions would have not been possible without an adequate FRET antibody pair suitable for PrP^C. The selection of the FRET labelled pair was conducted by testing four different combinations of FRET-labelled POM antibodies and choosing the one with the highest FRET signal and better dynamic range. Figure 4.3 shows the standard curves for the FRET pairs tested. The fitting of the data was performed with a sigmoidal 4-parameter logistic (4PL) equation, and the points after the hook point were eliminated. The FRET pair of APC-POM1/Eu-POM19 was selected as its shows the highest signal of the pairs, and it has also the broadest dynamic range of all the pairs.

4.2.2 Sizing of the recombinant mPrP

The first step in this project was to test the device with the recombinant monomeric PrP^C to measure its size and ensure that the device was suitable to work with this protein. In order to prevent PrP^C aggregation due to the presence of salt, the first experiments on the microfluidic device were performed with PrP^C in mQ water. In water the protein was sticking in the

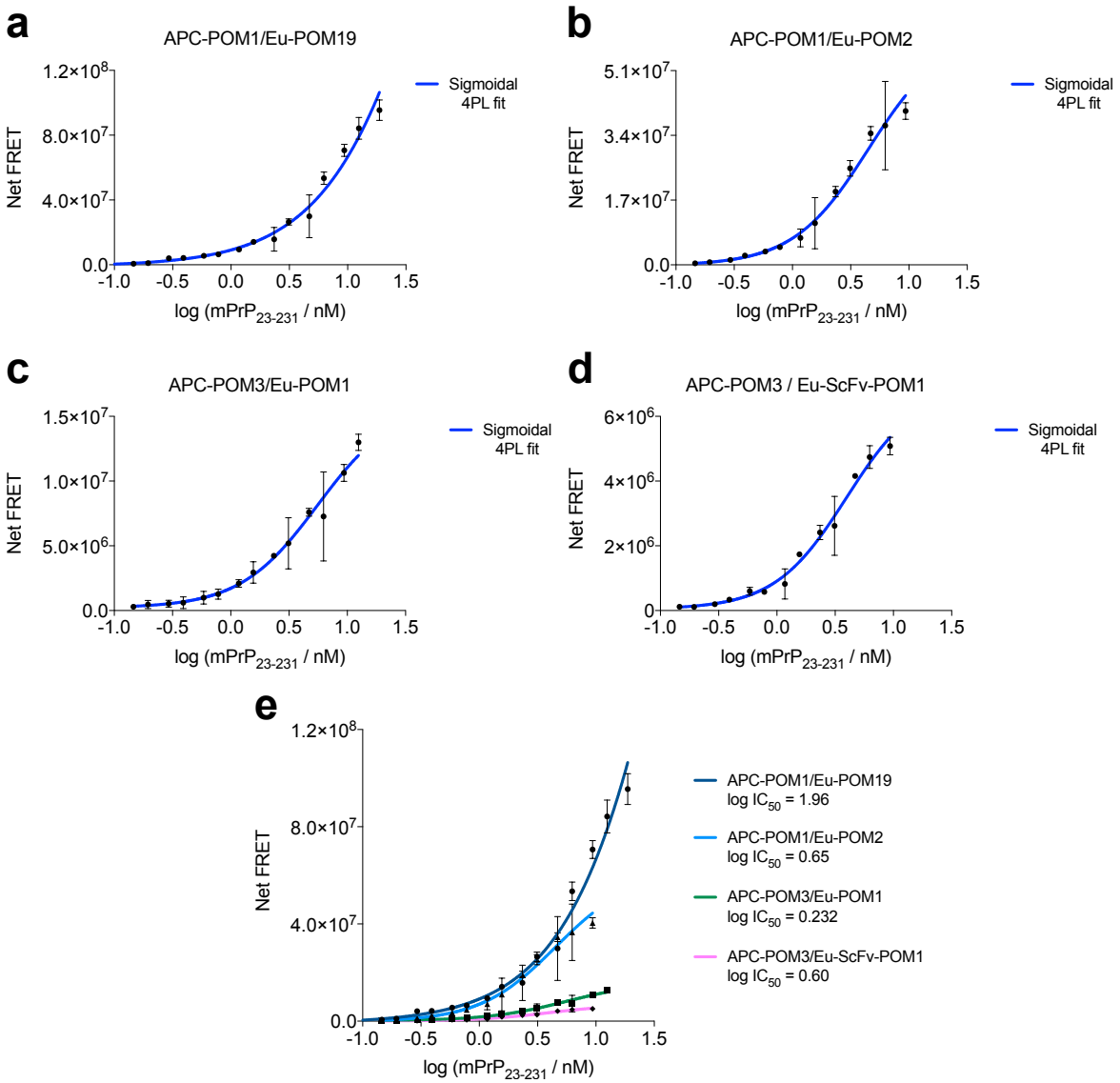

Fig. 4.3 Net FRET signal against PrP^C concentration for the different antibody pairs tested, a)APC-POM1/Eu-POM2, b)APC-POM1/Eu-POM19, c)APC-POM3/Eu-POM1 and d)APC-POM3/Eu-ScFv-POM1. e) Comparison of the standard curves for all the FRET-labelled POM antibody pairs tested.

plastic syringe and in the PDMS device. A successful experiment was performed with tris buffer and BSA (see Methods, Chapter 2, Section 2.3), since BSA adsorbs to the channel and prevents PrP sticking to the channels. The size of recombinant mPrP was then measured at a concentration as low as 100 nM and obtained a radius of 2.73 $\pm$ 0.5 nm, which is in good agreement with the 3.1 $\pm$ 0.5 nm value obtained at 300 μM with DLS and indicating that the mPrP is monomeric under the conditions tested. We note that the slight difference in size may be due to the change in viscosity caused by the variation in concentrations used in the two techniques.

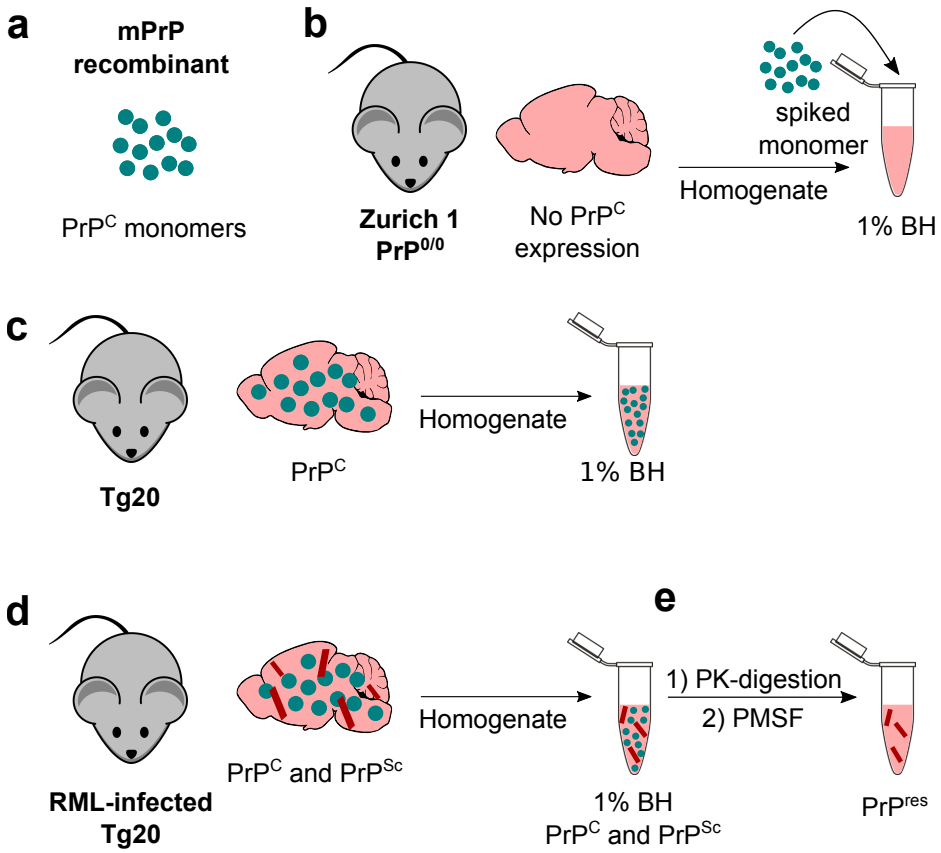

Fig. 4.4 a) As a control experiment the recombinant PrP^C was measured at a concentration of 20 nM in buffer only. b) Recombinant PrP^C was spiked into knockout BH, of ZH1 $PrP^{0/0}$ mice, also at a concentration of 20 nM. c) PrP^C overexpressing mouse (Tg20) BH was directly injected into the device and its size (3.1 nm) quantified via IDS. BH of RML-infected Tg20 contains both PrP^C and the scrapie isoform PrP^{Sc}. d) We have injected this BH directly into the device, and e) after digestion with proteinase-K (PK) enzyme followed by the addition of protease inhibitor phenylmethane sulfonyl (PMSF) to stop digestion before injection into the device. In this way the only species we detect with the TR-FRET are the PK-resistant ones.

4.2.3 Sizing of brain mPrP

The study of the native state of PrP from brain tissue is important for understanding its pathological effects, as it could provide a potential explanation for why it is prone to pathological aggregation. To investigate the difference between recombinant PrP and brain PrP in Tg20 mouse brain homogenate, we first "spiked" the recombinant form into Zürich 1 double knockout (ZH1 $Prnp^{0/0}$) brain homogenate (BH) and injected the BH directly into the microfluidic device (Figure 4.4 b). The obtained size of 3.5 ± 0.5 nm suggests no significant change in size from the pure recombinant mPrP. Then we investigated the size of protein directly obtained from PrP^C overexpressing mice (Tg20) BH (Figure 4.4 c), and compared

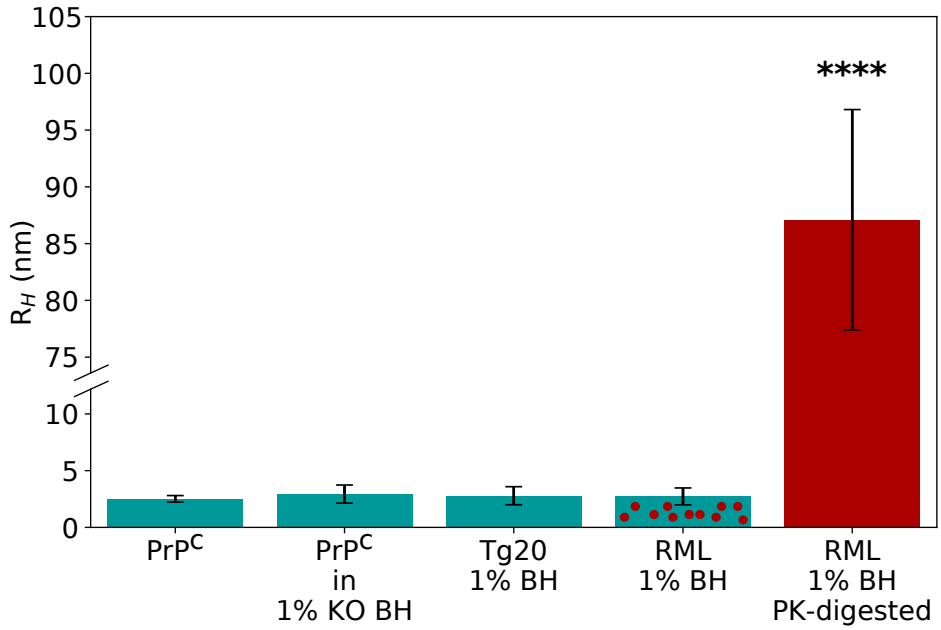

Fig. 4.5 The hydrodynamic radii of the different prion experiments made in this study. Values in bar graph represent mean ± SD of $n = 3$ experiments performed with different devices. One-way ANOVA $P < 0.0001$, followed by Tukey's HSD test $^{****}P < 0.0001$.

this to the one on RML-infected Tg20 BH of mice at the terminal stage of prion disease (Figure 4.4 d). Surprisingly, a similar size to the monomer (3.1 nm) was obtained in both cases (Figure 4.5). This could be explained because the fibrillar form of PrP^{Sc} is at much lower concentrations than the native PrP^C and therefore we mainly measured the size for the most abundant form, PrP^C. The method presented here provides information on the average radius of all the species in solution that the antibody pair binds to, and if that includes monomers and oligomers the results will be biased towards the higher concentration species.

4.2.4 Size of PrP^{res} in mouse brain homogenate.

One of the drawbacks of this study was the lack of a FRET antibody pair that binds only to PrP aggregates, since the POM antibodies bind only to PrP^C epitopes. In order to overcome this limitation and to size the misfolded, protease-resistant prion protein (PrP^{res}), we have treated BH of RML-infected Tg20 mice at the terminal stage of prion disease with proteinase-K (PK) digestion followed by addition of phenylmethyl sulfonyl (PMSF) to stop the digestion (Figure 4.4 e), before injection into the microfluidic device. Different conditions of PK-concentration and incubation times were tested in order to remove most of the monomeric PrP^C without digesting all the PrP^{res} fraction. In this way we guaranteed that the only PrP species in solution are PrP^{res} aggregates. However, by treating the sample with PK around 90% of PrP

was digested and the concentration was too low to be detected with TR-FRET, necessitating detection with a sandwich ELISA to detect down to subpicomolar concentrations. The complete removal of PrP^{C} and the presence of PrP^{res} after PK-digestion was confirmed with Western Blot analysis (See Appendix A Figure A.1). As shown in Figure 4.5, we obtained a size of 86.5 nm in a range from 77.7 to 97.1 nm, which indicates the average size for the PK-resistant aggregates found in the infectious brains.

4.3 Conclusions of PrP experiments

The application of IDS to the study of prions has demonstrated it has great potential for the study of native and infectious proteins at the biologically relevant conditions. The purification of prions represents a major challenge as parts of prion infectivity are lost during the PK-digestion process, and this method has overcome this limitation by measuring the sample directly without purification.

I have demonstrated the ability of this system to resolve a complex mixture such as mice brain homogenates, with monomeric and aggregated samples. Furthermore, characterising the average size of the prion in a biological fluid could potentially work as a diagnostic tool, as these data indicate that PrP aggregation can be detected when the average hydrodynamic radius exceeds the size of monomeric PrP^{C}.

4.4 Further work

A final piece of further work that would be useful is one that would address one of the limitations of IDS - the fact that it relies on a FRET antibody pair for detection. The size of the relevant infectious particles, PrP^{Sc}, in BH undigested sample would be possible with a TR-FRET pair specific for PrP^{Sc}.

We have used only one FRET antibody pair for all experiments, as this pair is suitable to work with BH. However, in order to be safe and make sure that all the infectious relevant species are measured, tests with different POM antibodies should be performed to confirm the current results.

In order to obtain more information from the infectious particles, the separated fractions of IDS could be tested for infectivity. Measuring the infectivity of both fractions would allow the clarification of which of the smaller or larger particles are the most infectious agents.

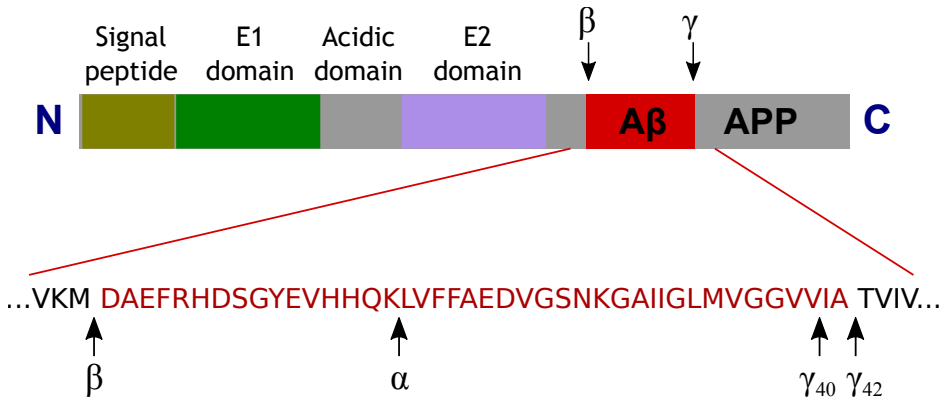

Fig. 4.6 The schematic shows the APP domains and the cleavage sites that lead to the formation of the amyloid β peptide. Adapted from [159] and [158].

4.5 Part II: Amyloidogenic oligomers

Amyloid-oligomers are increasingly thought to be the main cytotoxic agents in many neurodegenerative diseases, such as Alzheimer's and Parkinson's disease. Size could be a determining factor of the activity of oligomers as smaller species may diffuse faster and have a larger number of growing ends per unit mass of peptide [156].

4.5.1 Amyloid β properties

Amyloid Precursor Protein (APP) is a member of the APP family, which is conserved across a variety of species from mammals to invertebrates [157]. The function of APP has been widely studied due to its association with Alzheimer's disease (AD) and it has been suggested that it plays a key role in neuronal signaling, which may explain why APP disruption may lead to neuronal damage. APP has other key physiological functions during brain development and in neuronal plasticity, memory and neuroprotection in the aging brain [158]. Although the complete X-Ray structure of APP has not been resolved yet, it is available for the folded E1 and E2 subdomains, and information from NMR solved the structure for the C-terminal fragment-β and the cytoplasmic tail. Figure 4.6 shows a schematic description of the APP domains.

Monomeric Aβ is produced from the APP via cleavage by the enzymes β- and γ-secretase. The cleavage sites are indicated with arrows in Figure 4.6. The cleavage of γ-secretase occurs at various positions, leading to the formation of peptides of different lengths, such as Aβ43, Aβ42, Aβ40, Aβ38, and Aβ37 [52]. The Aβ42 peptide in particular, has received more attention as it has been considered to be the major etiologic agent due to

its more aggressive aggregation properties [160]. Aβ monomer is mostly unstructured in aqueous solutions, representing a equilibrium of interconverting conformations rather than a unique fold, determined by the solution conditions [161].

The amyloid cascade hypothesis suggests that the main pathological agent in Alzheimer's disease is the deposition of Aβ [162]. The hypothesis suggests that the tangles, neuronal damage and dementia are an effect of the peptide deposition, but it also suggests that other causes may trigger Aβ deposition, for example head trauma or mutations in the APP gene. However, in the last fifteen years the hypothesis has been modified with focus on the soluble oligomers as the most toxic species [163].

Unfortunately, due to their transient nature and high heterogenicity, the low-molecular weight oligomers are difficult to analyse with high resolution techniques [52]. Moreover, oligomers of a specific structure are difficult to isolate and therefore it has not been possible to obtain a high-resolution structure for the oligomeric species of Aβ40 and Aβ42 [164]. But even low-resolution techniques present some difficulties in studying these aggregates. DLS for example, would not only be biased towards the larger species in a heterogeneous mixture, but also would need a relatively high concentration of sample [87]. Therefore, the term oligomer has been broadly used to describe some form of non-fibrillar aggregates [165] such as disordered aggregates, micelles, protofibrils, prefibrillar oligomers and anular protofibrils. While the precise definition of an "oligomer" is broad, they can be classified by their origin in '*ex vivo*" or brain-derived oligomers and "*in vitro*-generated oligomers" [52].

The preparation method and solution conditions affect the structure of *in vitro*-generated oligomers, such as the buffer, ionic strength and metal ions. The latter are of particular interest since they have demonstrated to alter the kinetic pathway of Aβ aggregation as well as the structure of the aggregated species. Heavy metal ions are the first suspected to be implicated in the pathology of Alzheimer's disease due to their neurotoxic activity, but recent evidence points to the biologically important metals such as Zn, Cu and Fe [166, 167]. Some studies also focus in non-physiological aluminium, due to its prevalence in our environment [168].

The Zn^{2+} ion has been shown to inhibit the aggregation of Aβ at substoichiometric concentrations, by formation of a Aβ40-Zn^{2+} which binds to the fibril ends and reduces the elongation rate [169]. The interaction of Aβ and copper is stronger than that of Aβ-Zn, and some studies suggest then that the complex Aβ-Cu may play an important role in the early stages of Aβ aggregation [170]. The role of Aluminium in Alzheimer's disease remains controversial, mostly because it has been shown to be neurotoxic, but it seems to be poorly absorbed and efficiently excreted from the body [171]. Iron, along with Zinc and Copper,

has been found colocalised with Aβ aggregates in senile plaques [172]. Iron has been shown to increase Aβ generation and oligomerisation due to its chelating properties, like zinc and copper, which may form complexes with the His and Tyr residues located at the hydrophilic N-terminal region of the peptide [173].

4.5.2 aSyn properties

Synucleins are a group of proteins predominantly expressed in the brain, whose function is not yet totally understood. The synuclein family is formed of α-Synuclein (aSyn) and the β and γ isoforms, with 127-140 aminoacids in length ($\approx$ 40 kDa) and 50% similarity in sequence [174]. The protein sequence was first described in 1988 and named after its association with the synaptic vesicles and nuclear envelopes. aSyn is an intrinsically disordered protein, capable to adapt a variety of conformations, whose features depend on the protein environment and interactions with other binding partners [175]. The aSyn domain structure and sequence are depicted in Figure 4.7. It is mostly known by its association with multiple neurodegenerative disorders, like Parkinson's disease (PD) and the major non-amyloid beta component (NAC) of the amyloid plaques found in Alzheimer's disease patients [176].

The association of aSyn with PD was discovered as it was found to be the major component in the 70 molecules identified in Lewy Bodies (LBs), which are protein aggregates that are the pathological hallmark of the disease [177]. The direct role of aSyn in PD was demonstrated by genetic evidence, as a series of familial mutations leading to early-onset (A30P, E46K, A53T, G51D) or late onset (H50Q) PD have been shown to dramatically affect the rate of fibril production *in vitro* [178]. In addition to genetic modifications, it has been shown that post-translational modifications (PTMs), such as phosphorylation, nitration and dopamine modification to aSyn, could alter its propensity to aggregate or form oligomers [179]. Ubiquitination at multiple sites has also been found in CSF samples of PD patients but also in control samples [180]. The role of ubiquitination in PD is not completely understood. Whereas polyubiquitinated proteins are targeted for degradation by the proteasome system, monoubiquitinated proteins are not, and interestingly only the mono and diubiquitinated aSyn are the main forms found in Lewy bodies [181].

The general mechanism of aSyn aggregation has not been totally described yet. Recent evidence shows that aSyn aggregates proliferate by a prion-like process of protein seeding [182]. Moreover, it has been shown that the aggregation of aSyn depends strongly on the solution conditions. For example, at mildly acidic pH the amplification of aggregates

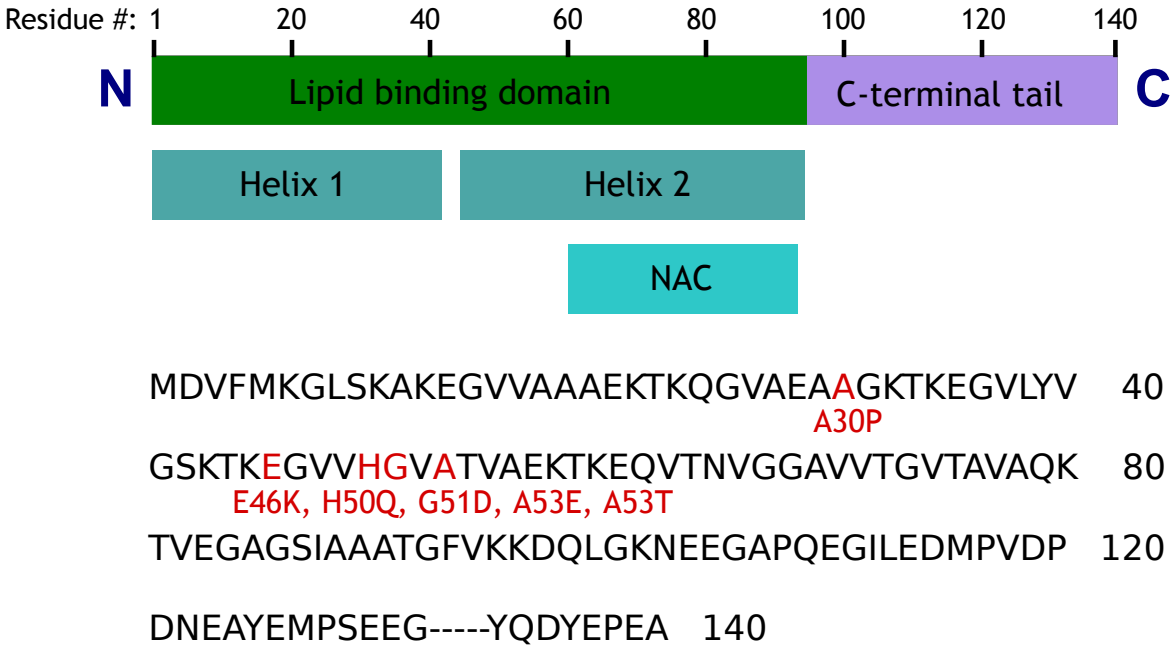

Fig. 4.7 The schematic shows the aSyn domain structure and amino-acid sequence, as well as the point human mutations indicated in red. The N-terminal domain folds into two helices upon binding to lipid membranes. Helix 2 contains the non-amyloid β component (NAC) domain (residues 60-95), which is prone to aggregation. Adapted from [176] and [174].

via secondary nucleation of monomers on the surface of fibrils, is much faster than at physiological pH [183]. Other studies suggest that the interactions of aSyn with lipid membranes play a key role in the aggregation process, as the presence of small unilamellar vesicles (SUVs) enhances the primary nucleation rate of aSyn by three orders of magnitude or higher [184].

The small oligomers formed during the aggregation process are thought to be the most cytotoxic species. By isolating stable aSyn oligomers their toxicity was shown by measuring their ability to disrupt lipid membranes and generate reactive oxygen species (ROS) in primary neuronal cells [108]. Moreover, solid state NMR experiments demonstrated that the main structural elements that give rise to oligomer neurotoxicity are the highly lipophilic element of aSyn oligomers that interacts strongly with the membranes, as well as a structured region that is able to disrupt them [185, 186].

The native state of aSyn is also important to understand its role in neurodegenerative disease. The pathological end-state of PD is well described from post-mortem tissue, but the early stage of the disease remains unclear. Whilst recombinant aSyn is largely unfolded, some studies propose that native brain aSyn purified from erythrocytes forms a stable tetramer that

prevents aggregation [187]. Other studies show that endogenous aSyn, purified from mice brain tissue, consists of an unstructured monomer and is aggregation-prone [188].

In this chapter, a combination of microfluidics with immunoassays, TR-FRET and alphaLISA , provide insights on the structure of stable aSyn oligomers as well as brain aSyn present in transgenic mice SNCA-OVX brain homogenates that express wild-type (WT) human aSyn at disease relevant levels [189].

4.6 Aims

The aim of these studies is to determine the hydrodynamic radius of two intrinsically disordered proteins, the Aβ40 peptide and aSyn in their monomeric and oligomeric forms. The Aβ40 peptide in particular has been challenging to study in a label-free manner, mainly because it does not have any tyrosines or tryptophans it its structure which would allow the study with intrinsic fluorescence. Due to their heterogeneous nature, any given isolation procedure could select a certain population of oligomers that might not reflect the spectrum of oligomers that exist under biologically relevant conditions. Moreover, since most biophysical studies are typically performed at non-physiological high-micromolar concentrations, it has not been possible to extrapolate the observations to very low total concentrations of oligomers observed *in vivo*. IDS could provide an alternative as it measures the hydrodynamic radius in a very sensitive way, and the method could apply for different solution conditions, such as different buffers and ionic strength background.

4.7 Results and discussion of amyloidogenic oligomers

Size of the Aβ40 monomer and metal-stabilised oligomers

IDS was suitable to characterise the size of the intrinsically disordered peptide, Aβ40, and its metal-stabilised oligomers at a concentration of 2 nM, as shown in Figure 4.8. The hydrodynamic radius of the monomer (0.9 ± 0.1 nm) is in good agreement with fluorescent correlation spectroscopy (FCS) (0.9 ± 0.05 nm) [190]. But it seems to be slightly smaller than the size obtained with NMR of 1.59 ± 0.1 nm at 25 °C [191]. The difference in the size obtained could be due the errors in dilutions caused by the low concentration needed in IDS of 2 nM.

The IDS method proved very useful in sizing the oligomeric forms of Aβ40, since these oligomers should be prepared in tris buffer, as any saline buffer like phosphate would

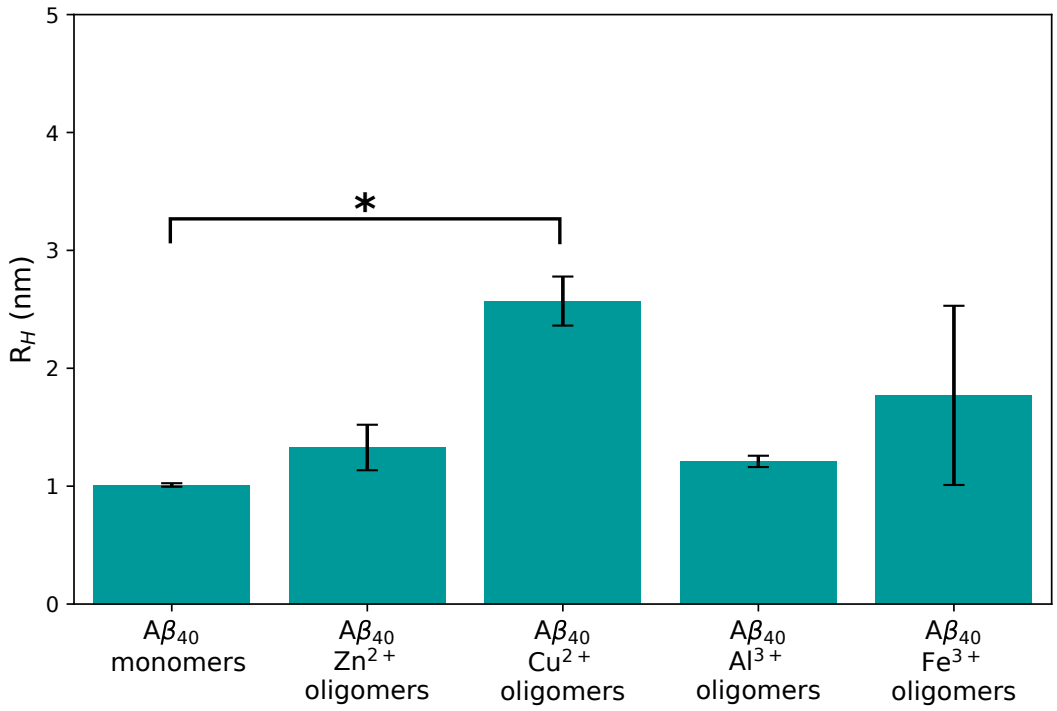

Fig. 4.8 Size of Aβ40 monomer and oligomers. The sizes were measured with IDS at concentrations of 2 nM in tris buffer with 0.01% tween to prevent stickiness. Values in bar graph represent mean $\pm$ SD of $n = 3$ experiments performed with different devices. One-way ANOVA $P = 0.0297$, followed by Tukey's HSD test $^{*}P < 0.03$.

cause the precipitation of metallic ions. The presence of tris prevents the measurements being performed with the Nu-sizing method [112] due to the presence of amines in the buffer. The main advantage of IDS over traditional sizing techniques such as DLS, is the low concentration needed to make the measurements. The sizing of the oligomers with DLS shows a bigger size because the hydrophobic surface of the oligomers makes them form clusters at the mili or micromolar concentrations needed for DLS. The measurements conducted at 2 nM guarantees that the measurement is made for oligomers rather than for clusters.

4.7.1 On-pathway oligomers

A key experiment to exploit in this method would be the sizing of on-pathway Aβ40 oligomers. The main drawback of this experiment was the lack of an antibody pair specific for aggregated forms of Aβ. Since the TR-FRET pair used to detect Aβ40 binds to its monomer as well as oligomeric forms, size exclusion chromatography (SEC) was used to separate the predominant monomeric fraction from the on-pathway oligomers of an

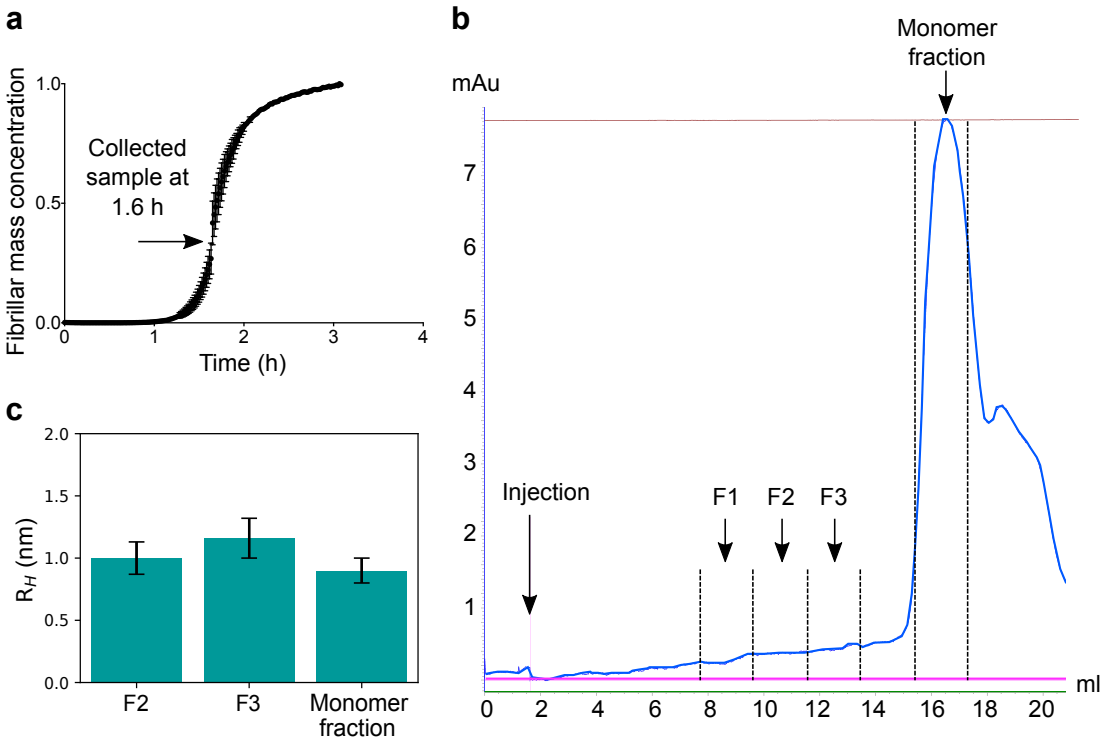

Fig. 4.9 Schematic description of the on-pathway oligomers experiment. a) Aggregation curve of Aβ40 (60 μM) at 37 °C, the error bars represent the standard deviation of three curves. The sample collection was conducted after 1.6 h reaction before separation with SEC. b) The chromatogram shows the monomer and collected fractions (F1, F2 and F3) which should correspond to the oligomers. c) The calculated sizes of monomer, F2 and F3 obtained with IDS, while the F1 concentration was below of the limit of detection of the TR-FRET. Values in bar graph represent mean $\pm$ SD of $n = 3$ experiments performed with different devices. One-way ANOVA $P = ns$.

aggregation reaction. Without the separation of the monomer, the result of IDS would only be the size of the monomer as it is the highest concentration species and the provided size is an average of all the species in solution.

As shown in in Figure 4.9 a, the sample was collected at 1.6 h which corresponds to the half time of the aggregation reaction. This time was chosen as previous simulations show that around this time the population of oligomers peaks [192]. Figure 4.9 b shows the fractions selected, F1, F2 and F3, that elute just before the fraction of the monomer. The resulting hydrodynamic radius (Figure 4.9 c) for the F2 and F3 of 1.00 $\pm$ 0.13 nm and 1.16 $\pm$ 0.16 nm respectively, are not too different of the size that corresponds to the monomer, of 0.9 $\pm$ 0.1 nm. The size of F3 could not be estimated with IDS as the concentration of this fraction was below the limit of detection of the TR-FRET assay. The measurements could not be compared to other sizing methods, like DLS, due to the low concentration of F2 and F3, of

1-2 nM. The hydrodynamic radius of F2 and F3 could only be the ones of the monomer, since these oligomers are metastable and it is possible that they have dissociated during the SEC separation. However, it is also possible that the sizes of the oligomers are just small, like the case of the stabilised Zn^{2+} and Al^{3+} oligomers, whose sizes are quite close to the monomer radius.

A key experiment would be performing the experiment directly after aggregation without any separation, but this requires an antibody pair which detects the soluble oligomers only, not the monomer or the fibrils. The detection with such a pair, would also make it possible to study the size of oligomers present in CSF of Alzheimer's disease patients, which due to their low concentration in the subnanomolar range, would make it impossible to study their sizes [193].

4.7.2 Size of aSyn monomer and oligomers

We exploit the sensitivity of the method to characterise disordered structures, such as the aSyn monomer to the size of a relevant Parkinson's complex, the stabilised aSyn oligomers (8 ± 1 nm) [108] (Figure 4.10). The sizing of the oligomers was performed with the microfluidic device designed for large particles, and the detection was conducted with a TR-FRET pair specific for aggregated aSyn, since it is a monoclonal antibody specific for aggregated aSyn labelled with either donor or acceptor, and then produces a FRET signal only in the presence of aggregated forms. In the case of the monomer, the detection was performed with alphaLISA immunoassay, at a picomolar concentration (233 pM), as the signal depends on a chemiluminiscence reaction upon proximity of the two antibodies. The estimated size for the monomer (2.3 ± 0.8 nm) corresponds well with previously reported size (2.82 nm) [194].

4.7.3 Size of brain aSyn

The native state of brain aSyn has been a subject of discussion as some studies suggest that it consists of a largely unfolded monomer that is prone to aggregation [188] while others suggest it is well structured tetramer that resists aggregation [187]. The discrepancy may be due to the purification method of brain aSyn on each of the studies. IDS provides the possibility to study the hydrodynamic radius of brain aSyn without purification. In this study, aSyn-overexpressing (SNCA-OVX) brain homogenate (BH) was used at 0.01% and injected into the microfluidic device (Figure 4.11 a). In order to determine the possible presence of aggregates, the sample was first tested with the TR-FRET pair for aggregated aSyn, but no signal was observed. A control of wild-type mouse BH was also tested in order to determine

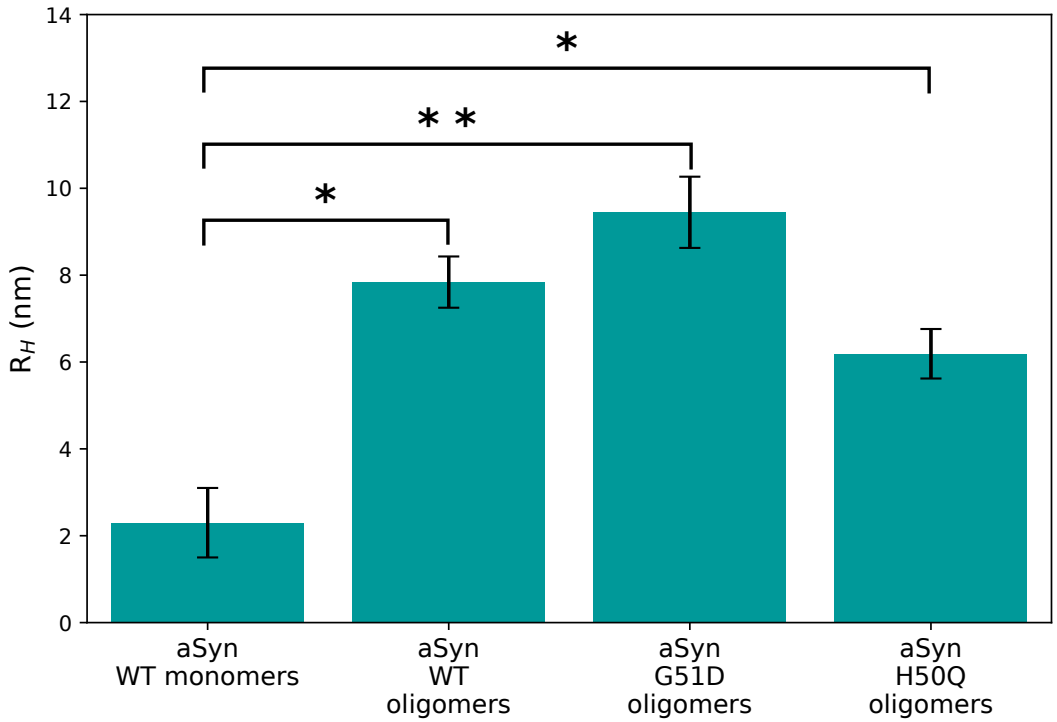

Fig. 4.10 Size of aSyn monomer and oligomers. The size of the monomer was measured with IDS at concentrations of 233 pM in tris buffer. The oligomers were measured at a concentration of 47 nm (in mass equivalents). Values in bar graph represent mean ± SD of $n = 3$ experiments performed with different devices. One-way ANOVA $P = 0.0024$, followed by Tukey's HSD test $^{*}P < 0.03$, $^{**}P < 0.002$.

if the centrifugation steps induce aggregation, but the TR-FRET pair was binding poorly to murine aSyn as a control experiment with recombinant murine protein showed. Therefore the following experiments were conducted with an alphaLISA assay specific for monomeric aSyn and the results, shown in Figure 4.11 b), indicate no significant difference between the size of the recombinant monomer (2.3 ± 0.8 nm) and the brain aSyn (3.34 ± 0.8 nm) measured at 233 pM and 0.01% BH, respectively. For comparison purposes, the recombinant aSyn was also measured with the benchtop unit of the native diffusional-sizing method [112] but in PBS since this unit utilises OPA labelling which binds to free-amines and therefore would bind to the tris-buffer. The result of 3.7 ± 0.1 nm is in good agreement with the size of the brain aSyn. Even though the recombinant protein seems to be smaller, the literature actually reports different values for the size of monomeric aSyn which range from to 2.0 to 2.96 ± 0.36 nm [112]. aSyn is an intrinsically disordered protein whose conformation state may vary depending on the solution conditions and temperature.

4.7.4 Post-translational modifications of aSyn

IDS depends on the detection of proteins with antibodies specific for them. Therefore if the method is applied to measure a biological sample or body fluids, a number of things are unknown, such as the concentration and the state of the protein, like the possible presence of post-translational modifications (PTMs), for example. A measurement of his-tagged aSyn was performed and compared to the same sample after *in vitro* translation (IVT) and *in vitro* ubiquitination IVU. As depicted in Figure 4.11 c, the IVU reaction performed with an enzyme is supposed to stop after 1 h, but this sample was measured after overnight incubation. A possibility is that the large protein size after the IVU reaction compared to the IVT of 3.5 ± 0.3 nm (Figure 4.11 d) is due to the presence of multiple ubiquitins bound to the protein. Furthermore, it was unclear whether the antibodies used in the alphaLISA assay would detect post-translationally modified (ubiquitinated) aSyn with the same sensitivity as with the detection of unmodified aSyn. If the sample was a mixture of mono, di and poly ubiquitinated aSyn, the diffused-fraction may contain species that cannot bind to the antibodies and the signal of this fraction would be small, reflecting in a large size (22.8 ± 1.4 nm). In order to improve this measurement, an experiment with antibodies for the his-tag or antibodies for ubiquitin rather than for aSyn would be the adequate to target the ubiquitinated protein.

4.8 Conclusions

The IDS method was suitable to study amyloidogenic oligomers under biologically relevant conditions. The experiments performed in this study were conducted with synthetic oligomers but it has demonstrated the potential of IDS to study biological mixtures, like brain homogenates. This method could potentially determine the protein sizes in biological fluids, such as CSF, to provide insights into the oligomeric population at different stages of the disease. Its main limitation is the requirement of an antibody pair specific for the aggregated forms of the protein, because usually the oligomers are in low abundance with respect to the monomer fraction. With a specific pair, a pre-separation step would not be necessary and the measurement could be performed directly in a complex sample. However, these antibodies are normally prepared by using synthetic oligomers as an immunogen, but the properties of the oligomers vary depending on the protocol of preparation, and therefore, it is very likely that any oligomer-specific antibodies obtained using a specific oligomer preparation may detect only a subset of oligomers in vivo. In order to have a more reliable study, it would be

good to perform the sizing with multiple antibody pairs. This method provides the sizes of intrinsically disordered proteins and protein complexes in a biologically relevant state, in a label-free manner and has overcome the sensitivity issues of traditional sizing techniques. The study of PTMs could be an interesting application of IDS, with a suitable antibody pair that targets a specific group such as ubiquitin. These antibodies are widely present in the market and their use expands the application of IDS which is often limited by the need of an antibody-pair specific for the target protein.

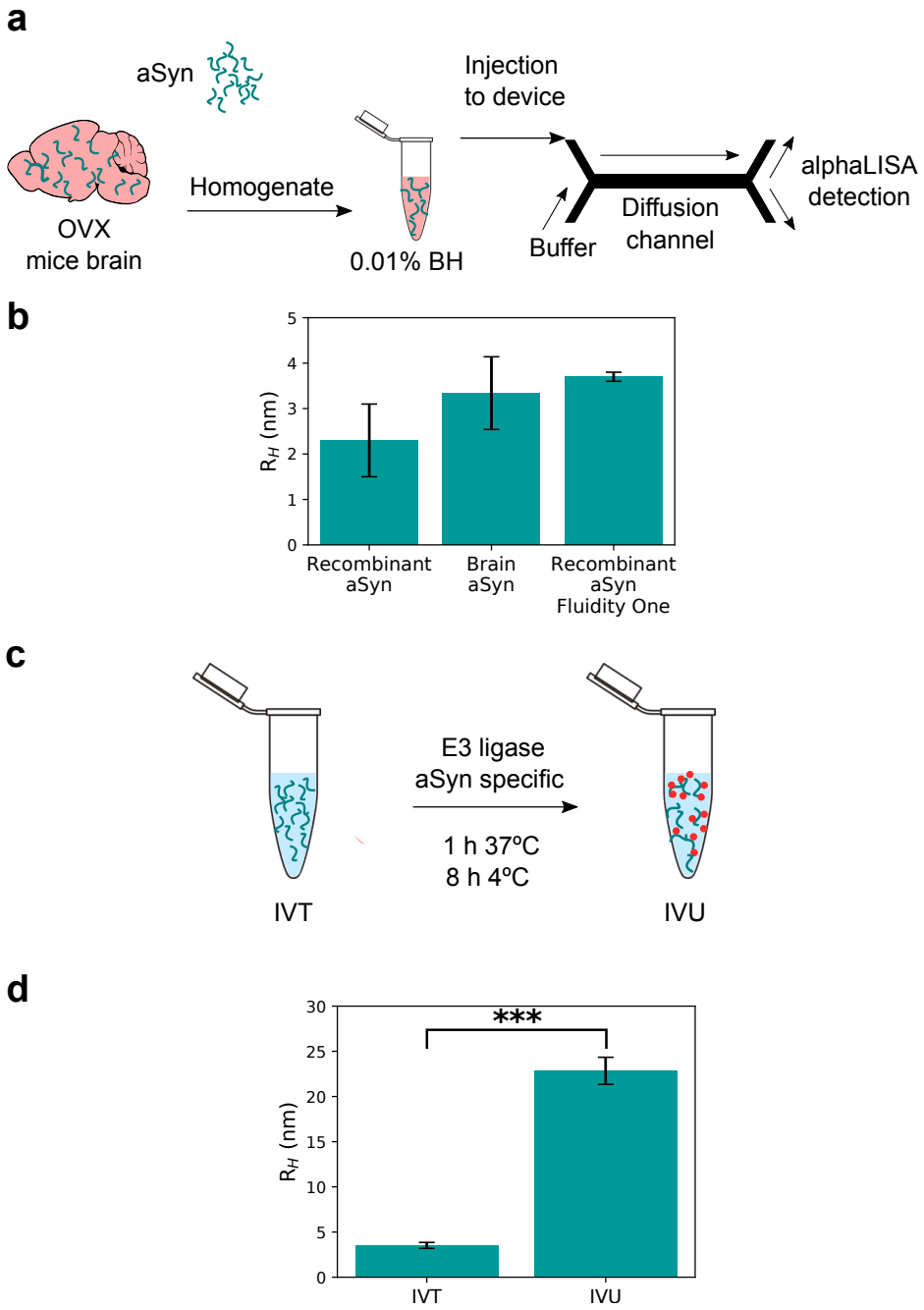

Fig. 4.11 Schematic description of experiments with brain aSyn and PTMs. a) OVX BH at 0.01% was injected into the microfluidic device to study the native state of aSyn. b) The resulting size of aSyn in the BH compared to the size of the recombinant monomer measured with IDS at concentrations of 233 pM in tris buffer and measured with the fluidity one at 100μM in PBS buffer. Values in bar graph represent mean $\pm$ SD of $n = 3$ experiments performed with different devices. One-way ANOVA $P = ns$. c) His-tagged aSyn was expressed in cell-free environment (IVT) and mixed with E3 ligase enzyme for ubiquitination (IVU). d) The difference in size of IVT and IVU measured with IDS. Values in bar graph represent mean $\pm$ SD of $n = 3$ experiments performed with different devices. T-test $^{***}P = 0.0006$.

Chapter 5

Towards TR-FRET on-chip detection

5.1 Introduction

Lab-on-a-chip immunoassays have greatly developed over the last two decades, leading to a range of diverse biosensor concepts and applications [195]. The miniaturisation of immunoassays into microfluidic technology represent many advantages such as the reduction of reagent consumption, portability, lower cost of the assay and a controlled environment [196]. However, the reductions in scale may result in a number of challenges such as the requirement of extremely sensitive detection schemes. This may be overcome by enhanced amplification, which is usually achieved by multiple steps assays, difficult to perform on-chip. An alternative could be the use of an homogeneous (in-solution) time-resolved FRET (TR-FRET) immunoassay, a fluorescence-based technique which has a wide range of applications from protein folding and dynamics to biosensing microfluidic reactors [197]. TR-FRET offers great analytical sensitivity and does not require antibody immobilisation. On the other hand, it remains challenging to miniaturise, partially because of the low quantum yield produced by the TR-FRET signal.

5.1.1 The principles of FRET

Föster resonance energy transfer (FRET) is a phenomenon widely utilised in biophysical research of macromolecular interactions due to its high resolution of typically 0.1 nm. FRET is a process in which a donor molecule in its excited state transfers its excitation energy through dipole-dipole coupling to an acceptor fluorophore, when both species are in close proximity (typically 1 to 10 nm) [198]. Although IUPAC nomenclature is Föster resonance energy transfer, sometimes it is also referred to as fluorescence resonance energy transfer.

FRET is a two-step process that occurs simultaneously via a non-radiative process. Excitation of the photons occurs from the ground (D) to the excited state (D*), and then the acceptor is excited from A to A* via dipolar coupling between dipolar moments of the donor emission and acceptor excitation [199]. FRET efficiency (E_{FRET}) varies as the sixth power of the distance (R) between D and A and can be determined with the following equation:

$$E_{FRET} = \frac{R_0^6}{R_0^6 + R^6}. \tag{5.1}$$

where R_0, Föster radius or critical distance, is the distance where FRET efficiency is 50% [134]. Although D-A proximity is necessary for FRET, orientation is also important. A geometrical factor, κ^2 , is related to R and it may change as R changes in different donor-acceptor configurations [200]. κ is related to R as indicated with the following equation (5.2):

$$R_0^6 = 8.785 \times 10^{-5} \frac{\kappa^2 \Phi_D J}{\psi^4} \tag{5.2}$$

where Φ_D is the quantum yield of the donor in the absence of the acceptor, η is the index of refraction (normally taken as 1.4 in aqueous solution), J is the overlap integral between the donor and acceptor, of the peak-normalised fluorescence spectrum between the donor and the acceptor [201].

Choosing a suitable donor-acceptor pair is a key step to perform a successful measurement. Among the conditions they should meet are: a) Sufficient separation in excitation spectra so that the light source is selective for the donor; b) enough overlap between the emission spectrum of the donor and the excitation spectrum of the acceptor to ensure efficient energy transfer; c) an adequate separation between the emission spectra to allow selective detection of emitted fluorescence from the acceptor and d) the distance between both donor and acceptor, when attached to biomolecules should be within 10 Å-100 Å [202].

5.1.2 alphaLISA as an alternative to TR-FRET

Since the FRET efficiency varies as the sixth power of the distance (eq. 5.1), the binding distance detection of TR-FRET is limited to 9 nm [133], amplified luminiscent proximity homogeneous assay (alphaScreen or alphaLISA) technology may represent an alternative to TR-FRET. alphaScreen is an homogeneous, nonradioactive bead-based assay that utilises a sandwich antibody pair. Described in 1994 by Ullman et al. [203], the method is based on the channeling of singlet oxygen species, generated from a photo excitable latex bead with laser

irradiation at 680 nm, to a second one located in close proximity to induce a chemiluminescent signal [204]. The beads are covalently bound to the antibodies, and therefore they come in close proximity in the presence of an antigen. The low background signal of the assay is due to the short singlet oxygen lifetime (4 ms) and the maximum distance that it can diffuse (up to 200 nm), as the beads are normally added in low concentrations to prevent non-specific interactions. Thus, the detection binding distance of the assay is of 200 nm.

alphaScreen technology has been implemented to microfluidics [205]. In that study, the detection mode was made by imaging several detection chambers simultaneously, as the device also integrated microvalves and micropumps to control the injection of the multiple reagents (antigent, antibodies and beads) at different times. Due to the complexity of the device design, a one-step immunoassay like TR-FRET may be the preferred one to integrate with IDS.

5.2 Aims of this project

In this project I have tried to implement the detection of TR-FRET at the microscale. Even though a number of optic systems are suitable for single-molecule FRET [206, 207], the detection of TR-FRET immunoassays on-chip remains a challenge. I have tested a custom-built setup analogous to the plate reader, with a LED as an excitation source and a camera for detection. I have also tested the detection with a photomultiplier tube (PMT) to obtain suitable detection, with no success.

I have also made a comparison of the performance of the alphaLISA and TR-FRET assays for the detection of insulin. Critical parameters for an assay include the sensitivity and reproducibility. Furthermore, a limiting factor for the implementation of these assays on-chip is the time required to get a stable signal. Therefore we have tested modifications to the PerkinElmer protocol which affect the kinetics and equilibrium of the antibody-antigen binding, such as incubation time, steps of addition, antibody concentration and temperature.

5.3 Results and discussion

5.3.1 Comparison of alphaLISA protocols

The protocol suggested by PerkinElmer involves a two-step one, which means mixing the sample with the antibodies/-acceptor beads mix, incubating, incubating and adding the donor beads for final incubation and reading. Although this protocol allows a better sensitivity, if

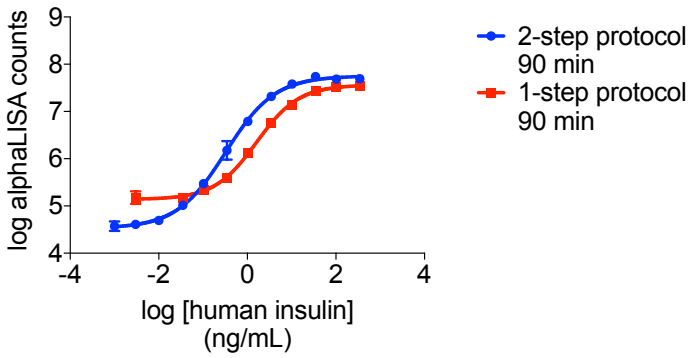

Fig. 5.1 The sensitivity of the protocol decreases by adding all the reagents in 1 step. The total incubation time for both protocols is 90 min. at 25°C.

one would like to implement this technology for IDS detection, a multi-step protocol would not be suitable for the reading on-chip. Therefore I measured the limit of detection (LDL) and lower limit of quantification (LLOQ) for each protocol in order to estimate the sensitivity loss by performing the assay in one step. Figure 5.1 shows the resulting standard curves with each of the protocols, at the same total incubation time. For the two-step protocol, the LDL was 7.94 pg/ml and the LLOQ was 23.44 pg/ml. The one-step protocol with a LDL of 82.00 pg/ml and LLOQ of 191.62 pg/ml was estimated. These values indicate a decrease in sensitivity of roughly 10 times for the 1-step protocol.

Another drawback to the implementation of immunoassays on-chip could be the incubation time required to stabilise the signal. The signal stabilisation time depends on the kinetics of the binding of antigen and antibody. In order to implement an immunoassay on-chip, the detection signal should be performed within a short time frame in the order of minutes. By contrast to immunoassays in bulk, long incubation times on-a-chip may be problematic due to evaporation or diffusion of the sample to the PDMS pores, as PDMS is permeable to water. Figure 5.2 a shows the alphaLISA signal at different incubation times. The signal stabilises only after 90 min incubation and the difference in signal intensity between 5 and 90 min incubation is nearly 10 times higher. From the plot of signal intensity vs. time for each of the concentrations shown in Figure 5.2 b it is clear that the signal reaches a maximum faster for the highest concentrations. If one would like to implement this assay on-chip, calibration should be performed for each of the measurements, as it was made with IDS and the measurements on the platereader. The microfluidic device could be modified to add some calibration points if the measurement is performed by imaging the detection chambers and calibration points simultaneously [205].

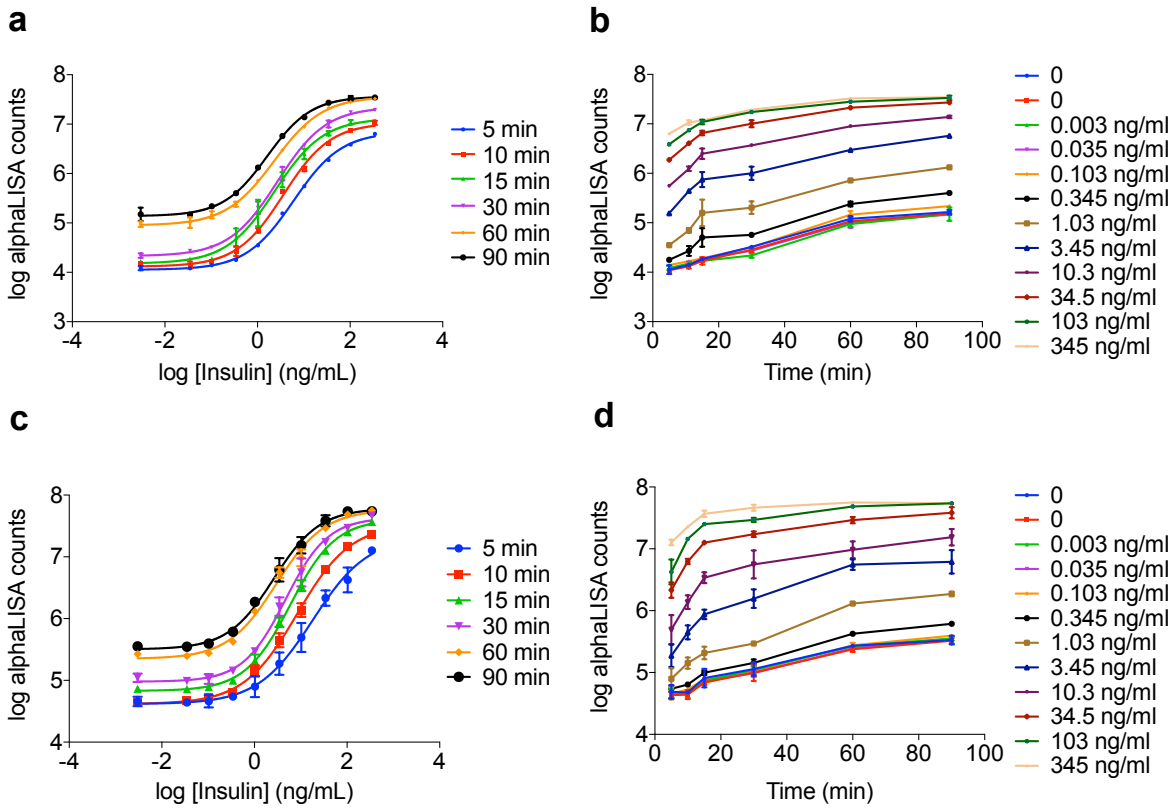

Fig. 5.2 Effect of the incubation time and antibody concentration on alphaLISA signal. a) Standard curves of alphaLISA obtained at different incubation times. The measurements were conducted at 25°C. b) Signal dependency of the time for the different concentrations used in a). c) Standard curves of alphaLISA with triple the concentration of antibodies, d) shows the signal variation over time when the concentration of antibodies is triple the original.

Increasing the concentration of antibodies up to 3-times as suggested by PerkinElmer did not change the signal equilibration significantly. The alphaLISA standard curves at different incubation times with 3x concentration of antibodies is shown in Figure 5.2 c. The signal is still increasing with time but the plots of signal vs time shown in Figure 5.2 d indicate that the slope decreases compared to Figure 5.2 b which indicates that an increase in antibody concentration accelerates the signal stabilisation. Nevertheless, an increase in the antibody/donor beads resulted in reduced sensitivity by a factor of 10 with respect to the original protocol.

Increasing the incubation temperature could potentially help to stabilise the signal the faster. The experiment conducted at 40°C shown in Figure 5.3 shows that indeed the signal stabilisation is faster at this temperature. This may be preferable to do rather than incubating the samples in the microfluidic device for longer times, with its disadvantage of a higher risk of evaporation.

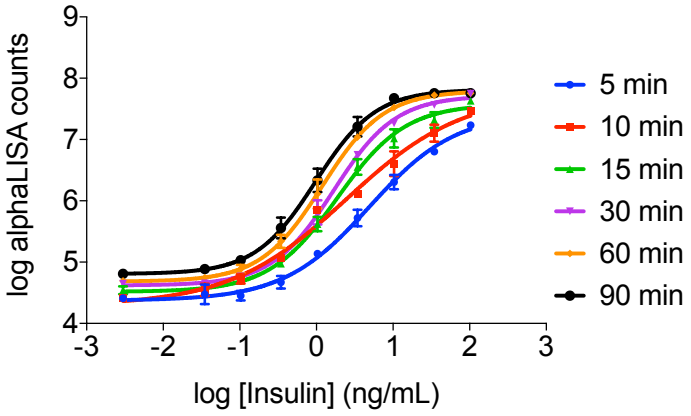

Fig. 5.3 AlphaLISA 1-step protocol at 40°C, reading at different incubation times.

5.3.2 Comparison of TR-FRET protocols

TR-FRET was the original immunoassay of interest due to its advantages over other assays, mostly because it is a one-step homogeneous assay and it lacks of dependence on background conditions. Normally, the signal stabilisation of TR-FRET also depends on the kinetics and equilibrium between antibody and antigen. The signal stabilisation time for the suggested PerkinElmer protocol was tested. Figure 5.4 a shows the standard curves at different times by incubation at 25°C for 90 min, and after overnight incubation at 4°C. Even though the signal keeps increasing over time, it does not change drastically in the first 20 minutes. From Figure 5.4 b it is possible to see that there is already a signal for higher concentrations from time 0, but the limit of detection improves with increasing incubation time.

The antibody concentration effect was tested and the results shown in Figure 5.4 c indicate that the Net FRET signal increases but so does the background signal. The plot shown in Figure 5.4 d shows that the signal maximum is closer to the values reached at overnight incubation (Figure 5.4). But it is important to mention that the experiment with an overnight incubation with 3x antibodies was not measured in order to compare if the maximum signal was reached or not. What is clear from Figure 5.4 d is that there is compromise of sensitivity, as the lowest values have the same signal as the control (buffer only).

5.3.3 The optics for TR-FRET on-chip

In this study, we have designed and implemented a FRET microscope with two detection modes, a camera and a photomultiplier tube (PMT), as shown in Figure 5.5. We have utilised the same optics as in the platereader, thus the excitation source adequate was a 340 nm LED. In these experiments the signal was detected at two different wavelengths, the donor emission

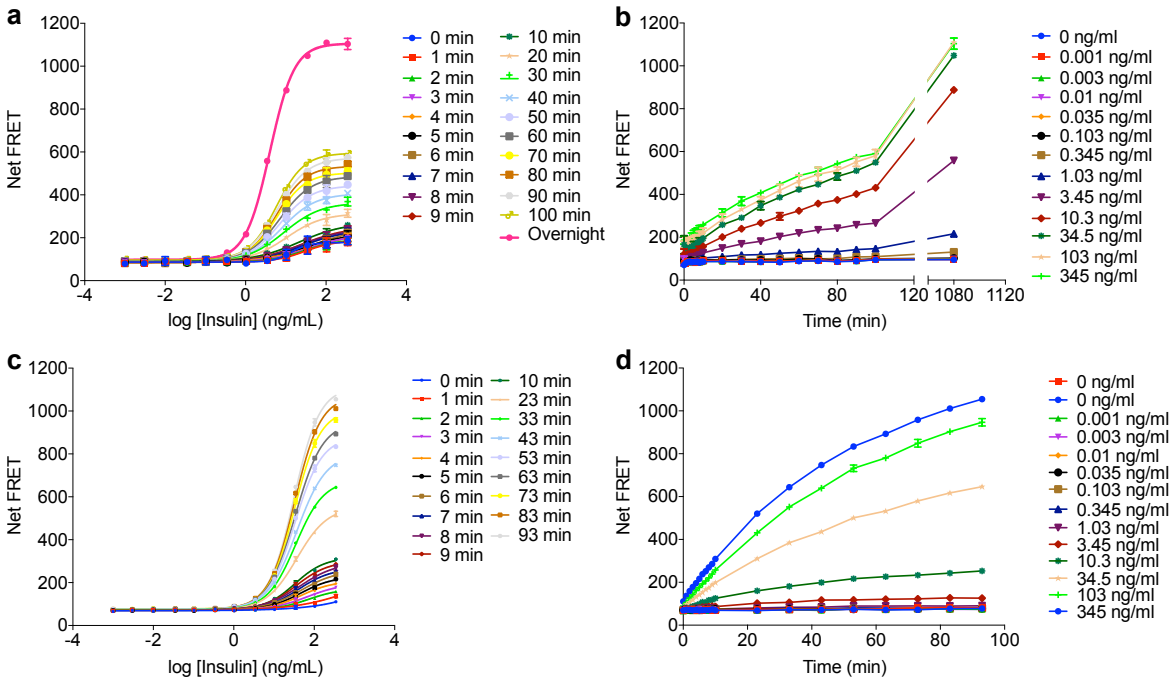

Fig. 5.4 Effect of the incubation time and antibody concentration on TR-FRET signal. a) Standard curves of the TR-FRET measurements conducted at 25°C incubation and b) the signal increasing over time for different concentrations. c) TR-FRET standard curves with triple concentration of antibodies, at different incubation times and d) shows the signal over time for each concentration using 3x antibodies concentration.

at 620 nm and the acceptor emmision at 665 nm. In the platform presented here we can exchange the filters in the filter cube manually. The camera was chosen to visualise the FRET signal in real time and by visualising it is also possible to focus the detection area of the microfluidic device. However, when samples of FRET labelled antibodies in the presence of the antigen at different concentrations (Figure 5.6) were observed, no change in the signals was detected. Figure 5.6 also shows a fluorescent signal from the antibody pair without the antigen, and we believe that this background fluorescence is from the donor emmision itself. We further tried to detect the signal of FRET with the PMT but no signal was detected either.

The images shown in Figure 5.6 were taken in a continuos mode, i.e. the LED was illuminating during the image acquisition process. We therefore believe that in order to detect the FRET signal, the acquisition control should be performed in a time-resolved way, to eliminate all the background fluorescence. Furthermore, these samples were tested on a platereader to confirm that they had FRET signal, but were injected into the microfluidic device manually and not under continuous flow, which may cause signal photobleaching. Europium cryptate (FRET donor) is known for its long-lived fluorescence lifetime and

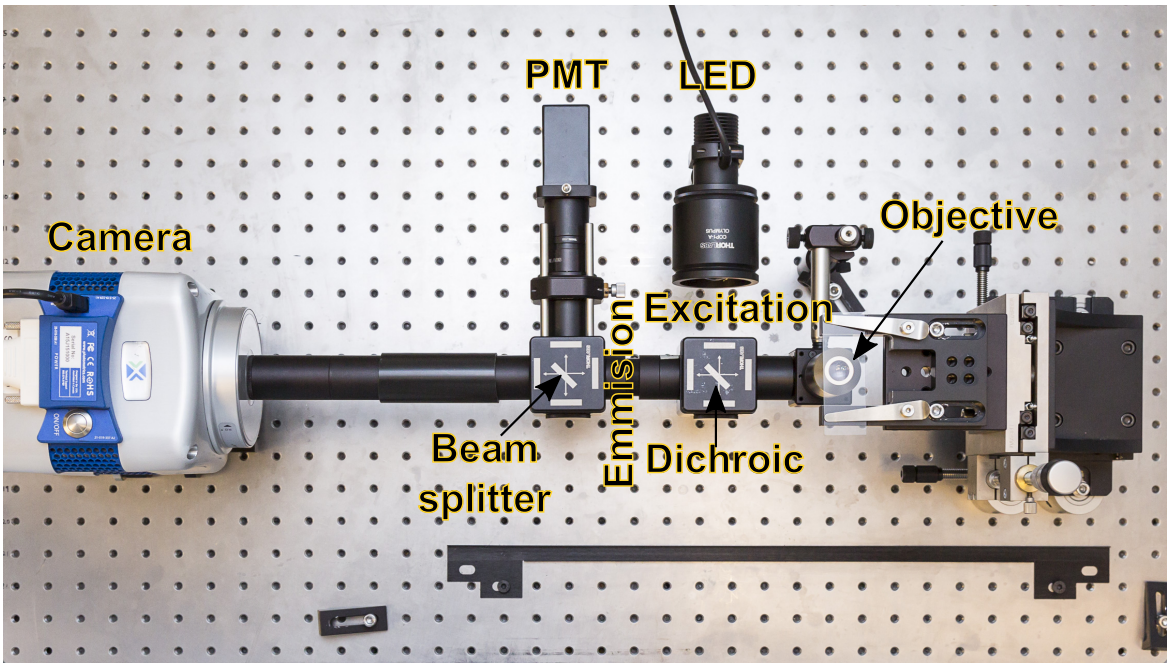

Fig. 5.5 Instrument built by Dr Pavan Challa and myself, for testing the signal of TR-FRET on-chip. The excitation source is a 340 nm LED, the light is reflected through a dichroic mirror to the sample and is emmision signal is detected with the filter for the donor (620 nm) and acceptor (665 nm). The camera is used for focusing the signal while the PMT can detect as well, when the beam splitter is used.

stability, so in principle the signal should remain stable over the image acquisition time course (2000 ms).

Even though these experiments were challenging, we have information on the optimisation that needs to be performed for the on-chip detection of the FRET immunoassay. Firstly, the measurement should be performed in a time-resolved manner, to eliminate all the background fluorescence. Moreover, due to the time dependency of the FRET signal, it may be necessary to make either incubation on-chip or calibration on the same device, against the blank and at least two concentrations to have the slope of the curve and the signals simultaneously to reduce errors. Finally, the platform should be able to exchange both emission filters automatically. We realised that exchanging the filters manually may cause some errors due to the time difference. Some commercial microscopes are available to exchange filters in an automated way, and a code could be written to make the measurement in a time-resolved manner, by excitation with a pulse and a time delay before acquisition.

The microfluidic device proposed for TR-FRET detection is shown in Figure 5.7 a. The device has the same geometry of an H-filter, as described in Chapter 2. But integrates an inlet for antibodies that mix them with the separated fractions just before detection in 2 chambers.

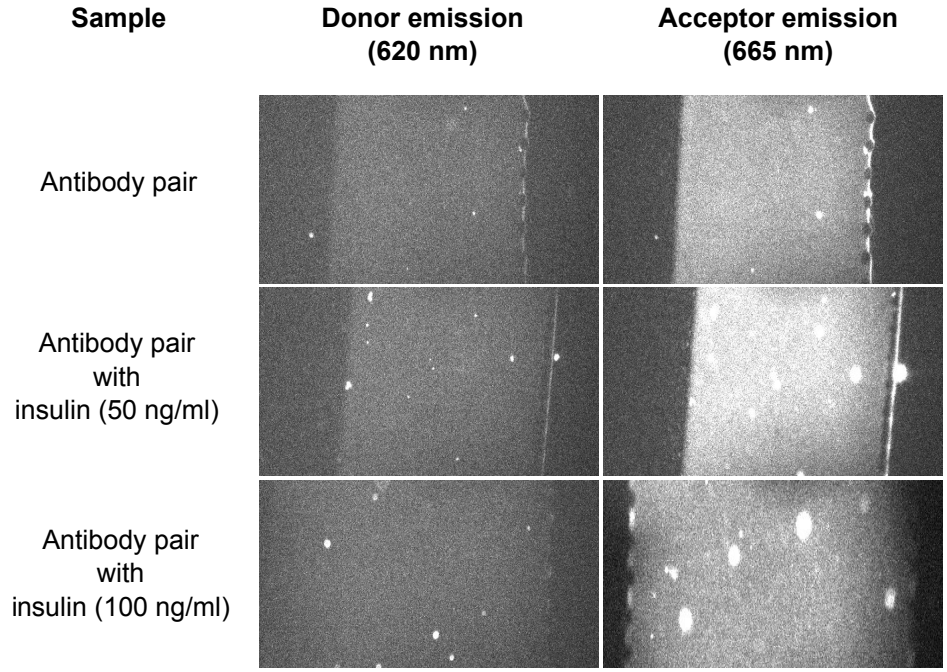

Fig. 5.6 Test of FRET platform with different antigen concentrations. Fluorescent images of the FRET-antibody pair with different insulin concentrations from 0 to 100 ng/ml, at 620 and 665 nm. No change in the net signal at 665 nm was observed with increasing antigen concentration.

In this design, the flow control is made with pulling mode, so only one syringe pump is needed at the device outlet and the length and with of the channels determine the flow rates at each of the channels. An schematic of the device seen as a microfluidic network with analogy to electrical circuits [140] is shown in Figure 5.7 b. In the particular case of insulin, the antibody to insulin ratio is 9:1. As such, the resistance of the channel of the fractions (r_{f1} and r_{f2}) and the resistance of the antibody sample r_{a1} and r_{a2} are designed in a way that they mix in a 1:9 ratio. The design is simplified by the geometry of the device, with is split into 50:50 fractions at the end of the diffusion channel. For a different sample, the device should be either adapted to the corresponding antibody to antigen ratio, or used in the positive displacement mode to control the flow rate directly from the syringe pumps. However, this mode would not be optimal because three syringe pumps would be used, one for the sample, one for the auxiliary buffer and one for the antibody pair. The FRET labelled antibodies are usually expensive and the withdrawing mode would be the preferred one, because it does not have the constraint of injecting the sample with a syringe, which requires a larger volume of sample.

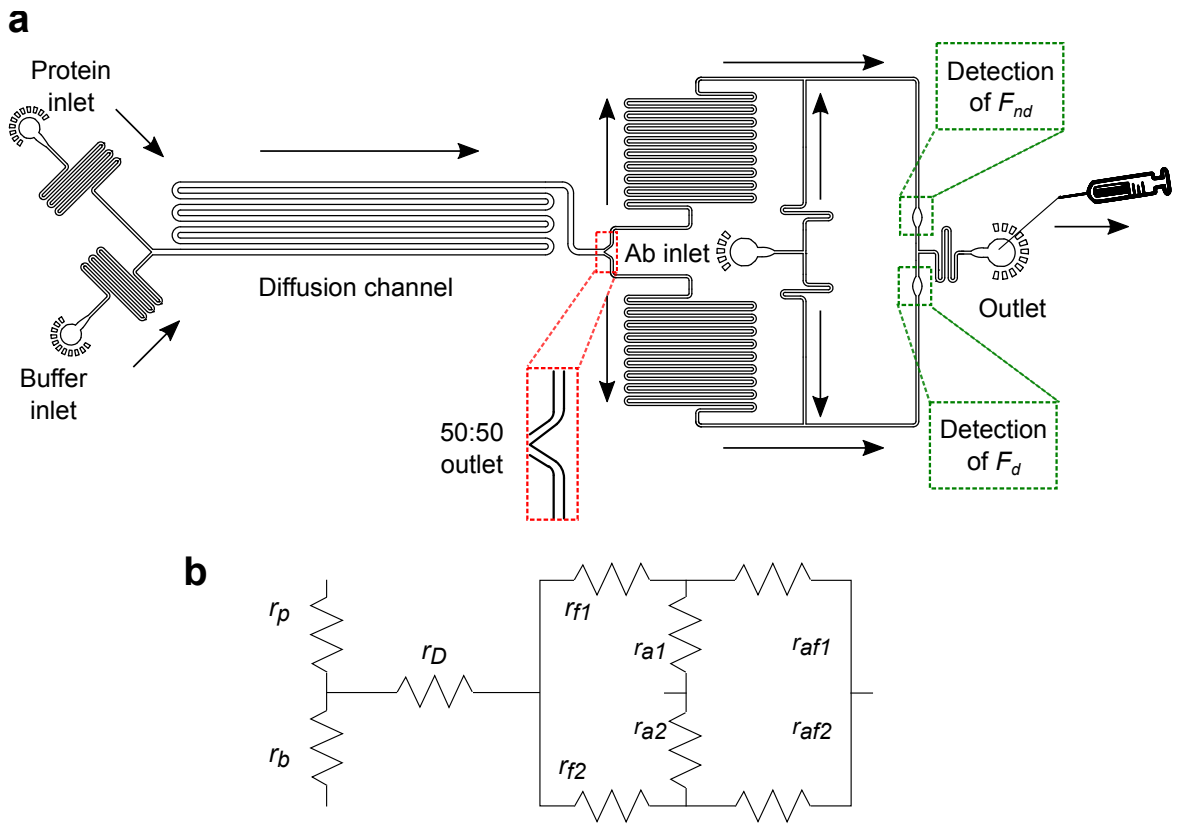

Fig. 5.7 A microfluidic device design for IDS oc-chip. a) The microfluidic device has the same geometry of an H-filter, but is adapted to inject the antibodies and mix them with each of the fractions in the same device. The detection of the signal for both separated fractions, f_{nd} and f_d is made on-chip. In this example, the flow is controlled with the withdrawing mode, therefore only one syringe pump is needed and the flow rate is defined by the resistance r of each of the channels. b) The device design can be seen as a microfluidic network analogous to the electric circuits [140]. In this design, the resistance are designed to have a ratio of protein to antibody of 1:9, as defined by the protocol of the TR-FRET.

5.4 Conclusions

In this chapter I have studied two commercial homogeneous immunoassays and varied some kinetic parameters such as incubation time, antibody concentration and temperature in order to determine the feasibility of implementing these assays to the on-chip detection of IDS. The results indicate that, for both assays, a decrease in the incubation time compromises the sensitivity. It was also shown to be the same for an increase in antibody concentration, where the signal may stabilise faster but would increase the LDL and LLOQ. Temperature may help to stabilise the signal faster but it also compromises sensitivity. Nevertheless, an increase in both temperature or incubation time may result in higher evaporation or diffusion into PDMS membranes. These results indicate therefore, that in order to implement immunodetection

for diffusional sizing on-chip, it may be necessary to include calibration points at the sides of the detection chambers.

We have designed and implemented a FRET platform to perform immunodetection on-chip. However, we believe that the actual FRET signal should be detected in a time-resolved way to eliminate all the background fluorescence. A microfluidic device design is proposed for the on-chip measurements of IDS. The withdrawing mode is preferred due to its lower sample consumption.

Chapter 6

Effect of the chaperone αB-Crystallin on insulin aggregation

6.1 Introduction

After being synthesised on the ribosome, the amino acid sequence of a protein is exposed to the crowded intracellular environment, that may promote misfolding and subsequent aggregation. As a consequence, protein folding *in vivo* is typically not a spontaneous process, and living organisms have evolved a class of proteins, called molecular chaperones, that counteract the tendency of non-native states to aggregate as a result of cellular stress [208]. Chaperones assist proteins in their correct assembly and disassembly of non-functional aggregates favoured by molecular crowding, in which the most favoured state is that which excludes the least volume for all macromolecules present [209]. Moreover, chaperones can also mediate the toxicity of aberrant protein oligomers, either by direct binding to the hydrophobic surface responsible for oligomer toxicity, or by conversion of the oligomer into larger and more innocuous aggregates [210]. Elucidating the exact role of molecular chaperones in the inhibition or promotion of protein aggregation may lead to new therapeutic strategies in the prevention and treatment of PMDs.

Perhaps one of the most studied molecular chaperones is the family of highly conserved stress proteins known as heat shock proteins (HSPs). These proteins are ubiquitous, occurring in all organisms from bacteria to humans. HSPs have been found to be involved in a multitude of functions, among them *de novo* folding, refolding of denatured proteins, oligomeric assembly and assistance in proteolytic degradation [211]. HSPs are first produced by cells in response to stressful conditions such as heat shock and while not all members of this family

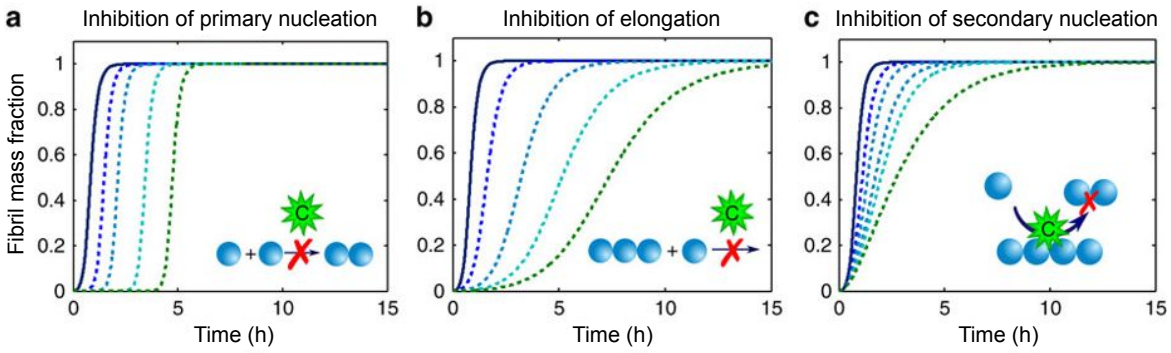

Fig. 6.1 Molecular chaperones can cause perturbation of the individual microscopic steps of the aggregation process. Schematic representation of the analysis of the global kinetic profiles of protein aggregation in the presence of molecular chaperones provides quantitative information on the specific microscopic steps altered. For example, different mechanisms (a-c) lead to different expected global kinetic profiles. Reproduced from [213].

are stress inducible, there are some that respond well to a variety of stresses, such as cellular energy depletion, extreme concentrations of ions, gases and various toxic substances [212].

A two-step strategy might be applied to understand how chaperones can perturb protein aggregation, such as the one used to study the effect of Zn^{2+} ions on Aβ aggregation [169]. The kinetic approach consists of characterising the mechanism of aggregation of the protein in the absence of the chaperone. Next, the same analysis is repeated in the presence of various concentrations of the chaperone. This approach allows us to pinpoint the change in protein aggregation kinetics, as the chaperone may specifically alter a single microscopic event, not the overall aggregation mechanism as shown in Figure 6.1. Finally, the kinetic analysis must be complemented with an experimental method to calculate the binding interaction of the chaperone-protein [214].

6.1.1 alpha B-Crystallin properties

The alpha-crystallins are members of the heat shock protein family. Alpha-crystallin accounts for about 35% of the protein in the mammalian lens, and particularly in the human lens it reaches a concentration of 450 mg ml^{-1} [215]. Although alpha-crystallin is better known for its chaperone properties, it has also been found to be related with several eye pathologies, including cataracts, among other conditions [216].

There are two alpha-crystallin genes, alpha A and alpha B. In the mammalian lens, the concentration ratio of alpha A to alpha B is generally three to one. There is about 57% homology between the amino acid sequence of alpha A and alpha B [215]. αB-crystallin

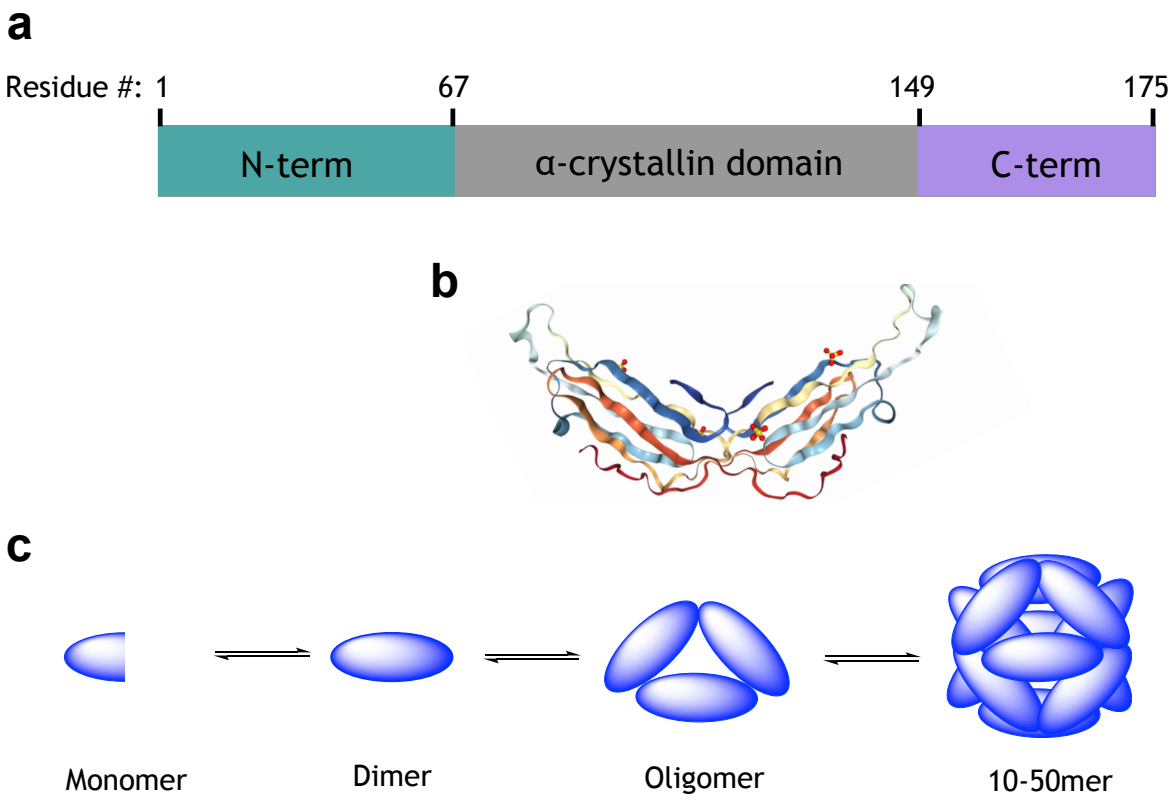

Fig. 6.2 The structure of αB-Crystallin (aBC). a N-terminal, α-Crystallin and C-terminal domains. Adapted from [217]. b) The 3D structure of truncated aBC (residues 68-162, PDB 3L1G). c) The dynamic state of aBC. The oligomers consist of a dimeric substructure as the fundamental unit of oligomers of 10-50 subunits [218].

(aBC) is a small heat shock protein found in several tissues including eye-lens, heart, skeletal muscle, brain, skin, spinal cord, lung and retina [219]. The three-dimensional structure of aBC consists of three domains, shown in Figure 6.2 a; an N-terminal domain, a highly conserved core known as the "alpha-crystallin core domain" and a highly flexible C-terminal extension consisting of 12 amino acid residues [220].

aBC does not have a defined quaternary structure, but rather a wide range of oligomer species consisting of 10 to 50 subunits [218] as illustrated in Figure 6.2 c. These species are capable of interconversion and are found to be strongly dependent on the solution conditions, such as protein concentration, ionic strength, pH and temperature. Since aBC does not crystallise even at very high concentrations, the crystalline X-ray structure for aBC has not been determined to date, yet NMR and small-angle X-Ray scattering (SAXS) studies have shown that a dimeric substructure comprises the fundamental building block of the oligomers [221].

aBC chaperone activity is closely related to the binding of non-native proteins by hydrophobic interactions. The correlation between temperature changes and chaperone activity has been previously studied, yet no significant changes in its activity were observed and the chaperone function is preserved at temperatures as high as 55-65 °C, which indicates that there is no notable conformational change affecting hydrophobicity [222].

aBC has further been found colocalised with α-Synuclein (aSyn) fibrils in patients with Parkinson's disease. This finding led to the study of the mechanism of inhibition of aSyn aggregation using ThT assays, QCM and NMR, amongst other techniques [223]. The results demonstrated that despite the weak interaction between aBC and monomeric aSyn, the chaperone strongly binds to formed aSyn fibrils, inhibiting fibril elongation. A similiar strategy was used to study the inhibition of Aβ42 aggregation by aBC. The results of this study revealed that aBC supresses the elongation phase of the peptide fibrils by strongly binding to the fibrils, perhaps because of the hydrophobic interactions between them [224].

In order to determine the ability of aBC to inhibit protein aggregation, several methods have been employed. In particular, quartz crystal microbalance (QCM) studies were performed to prove the inhibition action of aBC on insulin aggregation [225]. QCM [226] allows the monitoring of changes in the number of molecules in fibrils by measuring variations in their masses. Insulin fibril seeds were attached to the surface of the QCM, and the mass deposited on the surface was measured following the addition of insulin in the presence and absence of aBC. By using this technique, it has been possible to investigate the rate of fibril growth in the absence of nucleation and therefore prove that aBC inhibits the elongation of insulin fibrils at low pH.

Unravelling the detailed molecular mechanism of the chaperones' binding to aggregated protein species and its ability to modulate fibrils may be crucial in the development of adequate treatments for neurodegenerative diseases. This requires the study of intricate systems with multiple events occurring simultaneously in a complex environment. A deeper understanding of aBC's dynamic oligomerisation along with chemical kinetics will provide greater insight into the mechanism of the chaperone action.

6.1.2 The hormone insulin and its aggregation process

Insulin is a small protein hormone composed of 51 amino acids produced in the pancreas and secreted into the blood after meals in response to high blood glucose concentrations. Because of its propensity to self-assemble in long term storage for its application in diabetes treatments, as well as after repeated subcutaneous injections, it has been extensively studied.

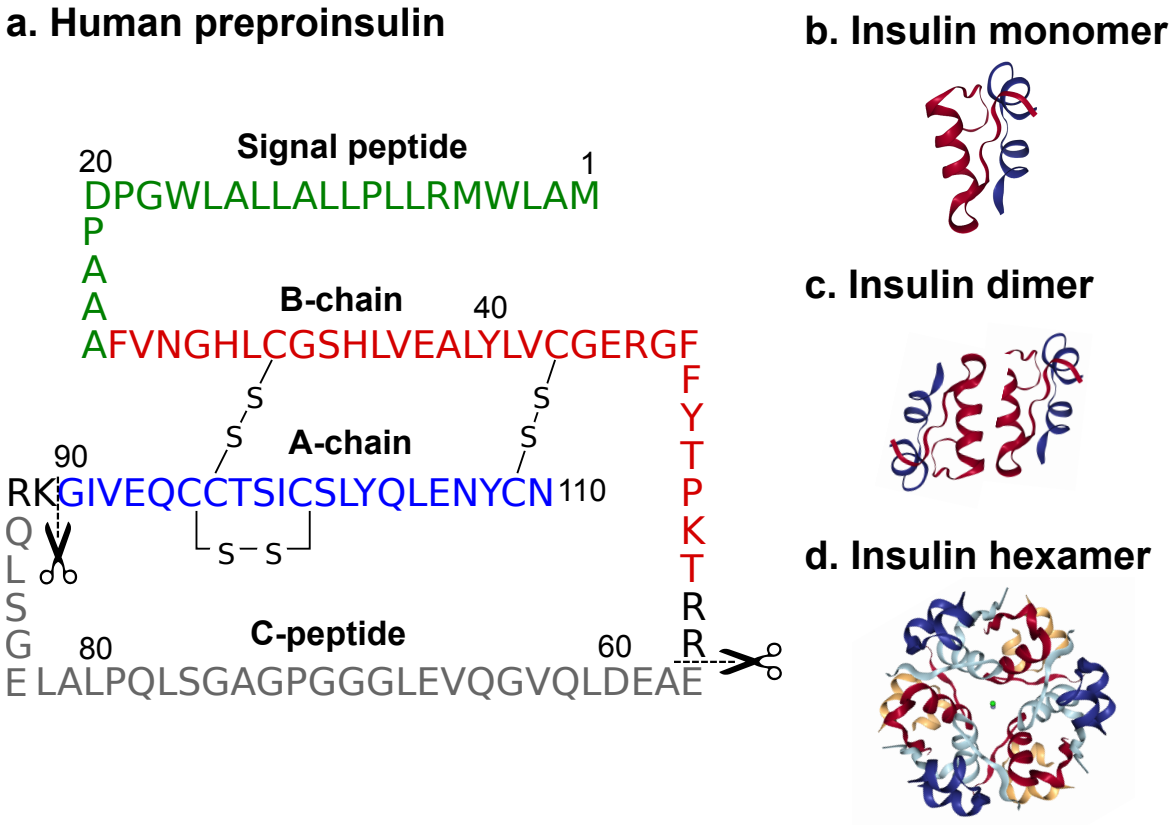

Fig. 6.3 a) Schematic representation of the amino-acid sequence of the human preproinsulin molecule, showing the cleavage sites for conversion from proinsulin to insulin. The signal peptide sequence is indicated in green, the B chain in red, the connecting peptide (C-peptide) in gray and the A chain in blue. b) Insulin monomer, c) insulin dimer and d) insulin hexamer. Adapted from [227]. 3D structures of insulin obtained from PDB (3I40 and 4EWZ).

Insulin is derived from human preproinsulin [228] and consists of two chains connected by two disulfide bonds and a connecting peptide (C), as shown in Figure 6.3 a, the A-chain (21 residues) which contains an intrachain disulfide bond and the B-chain (30 residues). The signal peptide is cleaved to form proinsulin during transport into the endoplasmic reticulum and the C-peptide is cleaved before the secretion of insulin from the pancreatic B cells [228]. The predominant structure of the monomer (Figure 6.3 b) is the α-helix, with high flexibility at the N- and C-terminal segments of the B-chain [229]. The physiologically predominant structure of insulin is normally found as a zinc-coordinated hexamer, formed by the association of three dimers [135], as shown in Figure 6.3 d. Yet, in the absence of zinc, insulin forms a dimer (Figure 6.3 c) at low protein concentrations over the pH 2-8 range, shifting to a tetramer at concentrations higher than 1.5 mg ml^{-1} [230].

In vitro aggregation of insulin can occur under specific conditions such as acidic pH, high temperature (60 °C) and increased ionic strength [231]. As its fibrillar structures share common properties with other amyloidogenic proteins, insulin has been widely used as a model system to gain insights into protein aggregation processes and their biological implications. The predominant α-helical structure is converted to a flat β-sheet state upon fibrillation. While several studies show that the B chain, or a segment of it (LVEALYL), may be the primary determinant of insulin fibrillation, there is also evidence that the A chain can contribute [232]. A-chain and the B-chain of insulin can form fibrils on their own and nucleate the fibrillation of full-length insulin, while the soluble chain peptides are able to inhibit insulin fibril formation [233].

By using the fluorescent dye ThT, the kinetics of insulin aggregation in bulk was studied under several variables, among them, the effect of concentration, pH, ionic strength, anions, the addition of the denaturant urea, and the stabilisers trimethylamine N-oxide dihydrate (TMAO) and sucrose [234]. A decrease in lag time and faster fibril growth was observed when increasing insulin concentration. A similar trend was observed when decreasing the pH from neutral to acidic. Regarding ionic strength, no clear correlation with fibril growth was found. Unlike the denaturant which decreased the lag time, the stabilisers TMAO and sucrose showed increased lag times. These results indicated that electrostatic and hydrophobic interactions control both nucleation and fibril growth. Regarding the fibrillar structure, data obtained by TEM has shown that the diameter of the fibrils is around 20 nm, which does not change with increasing incubation times, as opposed to the length which may increase up to 2-3 μm [235]. The physical properties of insulin fibrils were characterised with AFM and force spectroscopy. The fibrils have a strength of 0.6 ± 0.4 GPa. In addition, a breakage rate constant was found to be $1.3 \cdot 10^{-8}$ s^{-1}, which indicates that a fibril of 10 μm length breaks spontaneously on average every 47 min [236].

Although insulin fibrils have been extensively studied, no integrated rate law for the mechanism of insulin aggregation has yet been determined. Macroscopic experiments, along with microdroplet assays, would provide an ideal technique to calculate the numeric values of the rate constants for a deeper understanding of the mechanism. A disadvantage of the macroscopic experiments, such as ThT assays, is that it is very challenging to track individual nuclei in solution. Thus, volume confinement techniques have been developed in order to form microreactors with a limited number of nuclei that can be followed over time while determining the aggregation kinetics of fibrils formed as a result of secondary processes [110, 237]. Microdroplet experiments of insulin aggregation have demonstrated that primary nucleation rate depends strongly on system size. By forming different sized droplets it

was shown that when the system size decreases below a critical volume, the lag time of aggregation increases significantly, therefore proving that confinement helps proteins to remain soluble [238].

6.2 Aims

Molecular chaperones play a key role in modulating the aggregation process of amyloidogenic proteins. aBC has been extensively studied using several methods, yet a detailed understanding of the underlying mechanistic process of this chaperone remains unclear. In particular, most commonly used methods in studies involving aBC require an immobilisation step on a surface, which makes it difficult to determine whether the chaperone plays a role in the inhibition of primary nucleation in solution. The molecular mechanism of aggregation reactions in the presence of inhibitors has remained challenging, mostly because the aberrant aggregation of proteins takes the form of complex networks, with elementary steps that depend on several species and simultaneous reactions. Nevertheless, an approach to understand the mechanism by which molecular chaperones suppress protein aggregation is by identifying which of the reaction steps is perturbed [214]. In this study, a global kinetic profile analysis of insulin aggregation in the absence and presence of the chaperone reveals that aBC inhibits primary nucleation and reduces the elongation rate. Hence, microdroplet experiments were performed in order to confirm the observations made in bulk.

6.3 Results and discussion

Understanding the molecular mechanisms involved in protein aggregation is a multifaceted problem due to the number of processes that occur simultaneously. However, in the case of an inhibitor, it can be simplified as it usually supresses the self-assembly process by potential interaction with the substrate protein in either its monomeric misfolded, oligomeric or fibrillar forms. As a consequence, either the primary or secondary pathways of the aggregation process can be influenced by chaperone binding [214]. In this approach, a model that describes insulin aggregation was first identified and, using this model with the chaperone, the specific microscopic steps that are perturbed by aBC were determined.

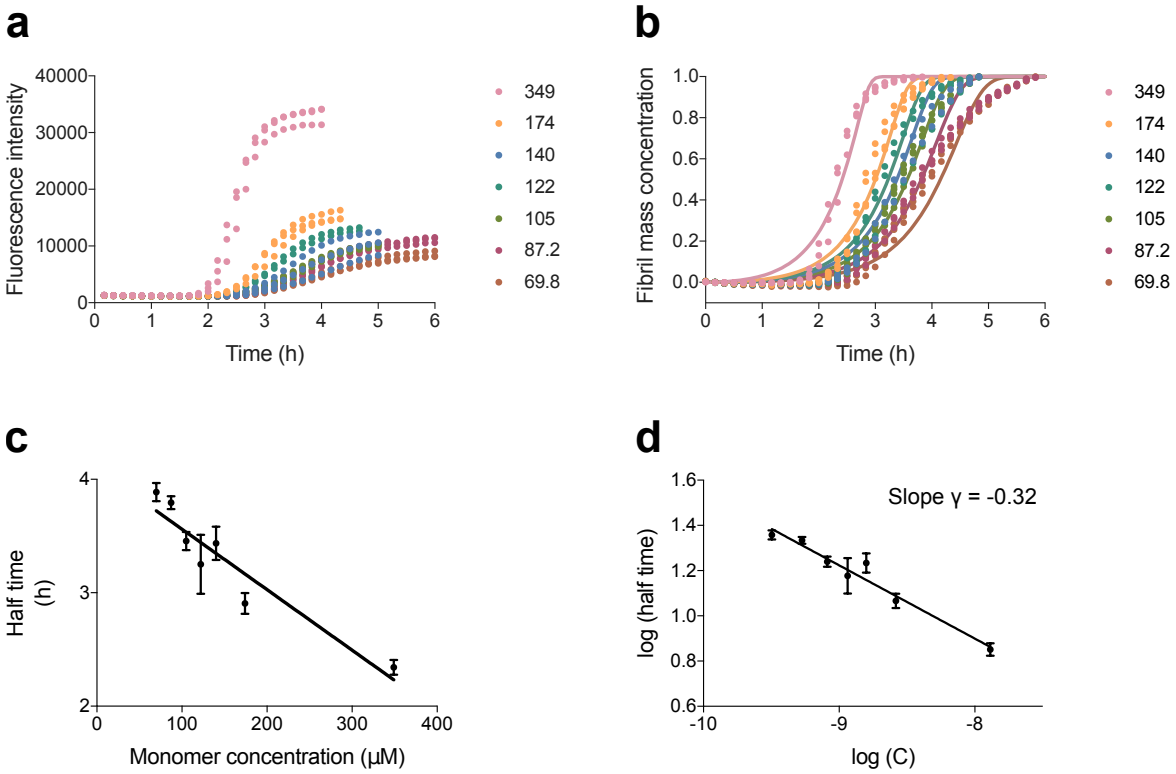

Fig. 6.4 The rate limiting steps of insulin aggregation. a) The kinetic traces for different insulin concentrations, by ThT fluorescence at acidic pH and high temperature (60 °C). b) Normalised data with the fitting of a model with saturating elongation and fragmentation, obtained with the aggregation fitting software Amylofit [109]. c) Half time scaling of insulin aggregation under the same conditions. d) The scaling of the log (half time) plot with a slope γ of -1/3 which gives an indication of the mechanism of insulin fibrillation.

6.3.1 The mechanism of insulin aggregation

In order to understand the aggregation process of insulin in the presence of an inhibitor, it is necessary to first describe the system itself. Insulin aggregation has been widely studied as a model protein, but so far no detailed mechanism for aggregation has been reported. To obtain more information on the mechanism, fibril growth from insulin monomer at acidic pH (1.4) and high temperature (60 °C) was measured for several monomer concentrations from 8.7 μM to 349 μM. The data were subsequently analysed using the approach by Meisl et al. [109], of performing a global fitting with different models to determine the molecular mechanism for insulin aggregation (Figure 6.4).

In the approach of Meisl et al. [109], the first step consists of normalizing the raw data, shown in Figure 6.4 a, because at different monomer concentrations the ThT endpoints would be different for each of the curves. Afterwards, the half times (Figure 6.4 c) and scaling are

calculated in order to determine possible models that would fit the data better. For this set of conditions, the scaling exponent is $\gamma = -\frac{1}{3}$. This indicates a possible saturating process, either saturating elongation and fragmentation or saturating elongation and secondary nucleation. The best fit was obtained with a saturating elongation and fragmentation model (Figure 6.4 b), which describes this range of concentrations well under acidic pH and high temperature conditions. This model confirms previous studies on insulin aggregation where fragmentation plays an important role on the mechanism [42, 239].

The best model to fit these data was the saturating elongation with fragmentation, which means that several processes are implicated in the aggregation of insulin where at high concentrations of monomer the elongation rate is saturated and fragmentation plays an important role. Even if fibril fragmentation is a monomer-independent process, the number of monomers available affect the elongation rate and as fibrils can grow faster, they can also break more easily and generate new fibrils ends. In aberrant aggregation, primary and secondary pathways always play a role, but solution conditions determine which one is the dominant process. In the case of insulin, under the conditions used here, it seems that elongation and fragmentation are the dominant steps.

6.3.2 Kinetics of insulin aggregation in the presence of aBC

In order to understand the mechanistic step at which aBC inhibits the aggregation of insulin, experiments using insulin with different molar ratios of chaperone were conducted, and the chaperone showed an effect of rate reduction at concentrations as low as 10%. The kinetics of amyloid formation in the presence of an inhibitor can also be analysed with the Amylofit interface as a perturbation of the rate constants. As insulin follows a model of saturating elongation and fragmentation, the same model has therefore been used to analyse the data with the inhibitor. Figure 6.5 a-c shows the possible outcomes resulting from the selective reduction of each of the microscopic rate constants, or those relevant in the mechanism of insulin aggregation, primary nucleation (k_n), fragmentation (k_-) and elongation (k_+). The dots are the experimental data and the continuous lines show the kinetic curves resulting from simulations when each of the rate constants is affected. The experimental data show an increase in the lag time without any change in the steepness of the sigmoidal transition, which suggests a reduction of k_n. The fitting values with a reduction in the primary nucleation constant (Figure 6.5 a) describes the process better. The reduction of k_- leads to a change in the slope but it does not reduce the overall nucleation rate significantly, and as shown in Figure 6.5 b, this model does not describe the experimental data. Finally, a decrease in k_+

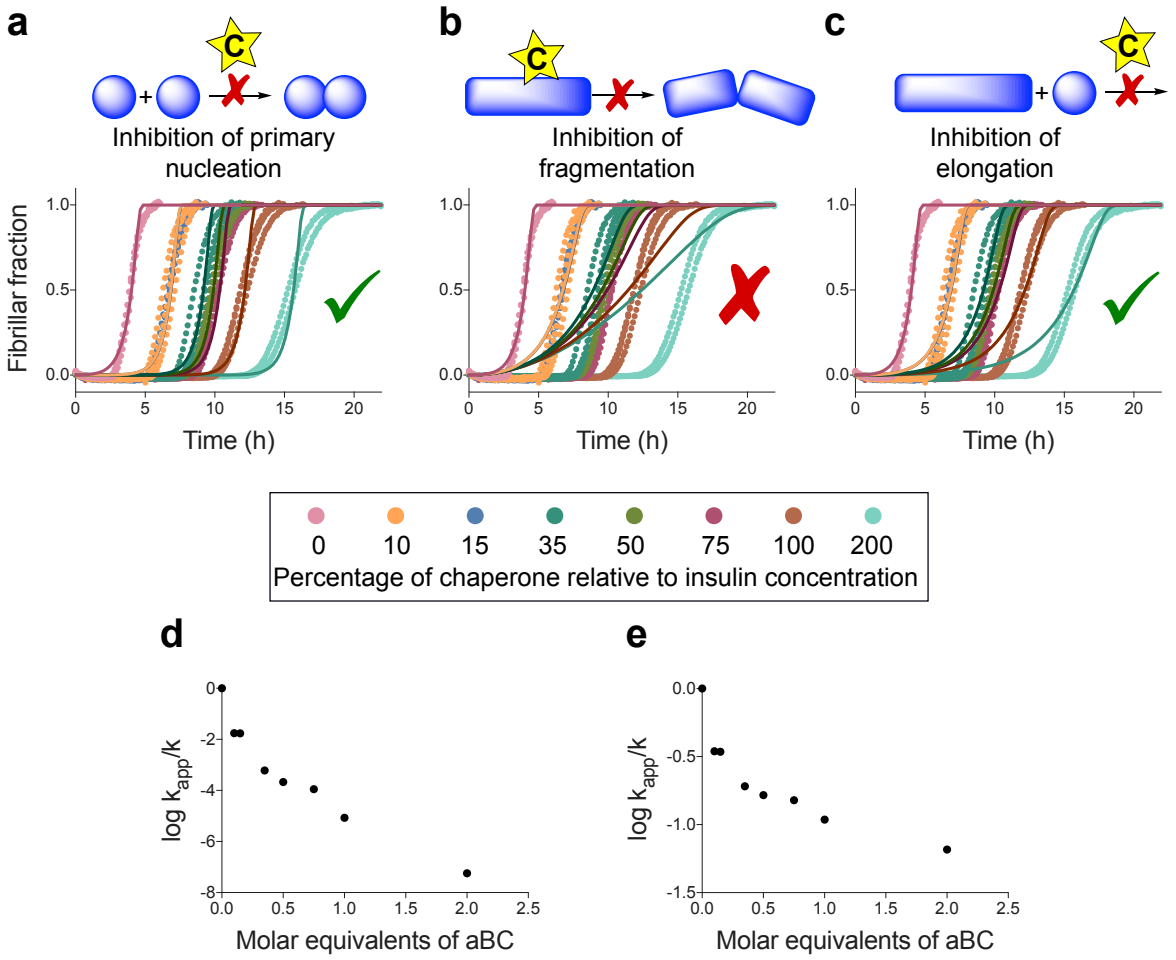

Fig. 6.5 aBC inhibits the primary nucleation and elongation steps of insulin aggregation. (a-c) Kinetic profiles of the aggregation reactions of a 349 μM sample of insulin in the absence and presence of increasing concentrations of aBC (0 to 200%, represented by different colours). The solid lines show predictions for the resulting reaction profiles when a) primary nucleation, b) fragmentation, and c) elongation are inhibited by the chaperone aBC. The prediction for the case where primary nucleation in perturbed, fits closer to the experimental data (represented with dots) but the prediction of fragmentation may also describe the data. d) and e) shows the decrease in the apparent constant (k_{app} for primary nucleation and fragmentation). Note that the decrease in k_{app} for primary nucleation is larger than for fragmentation.

leads to an extended lag phase and decrease in slope as well. Figure 6.5 c shows that even though this is not the best fit, it still describes the lag time and a part of the aggregation curve. This may suggest that the chaperone plays a role in the inhibition of both primary nucleation as well as elongation. Figure 6.5 d-e shows the change in the apparent constant (k_{app}) for primary nucleation and elongation, respectively. The change in the primary nucleation constant k_n is notably larger than the one in elongation k_+, which may indicate that under these conditions the chaperone might interact more strongly with the monomers or prefibrillar

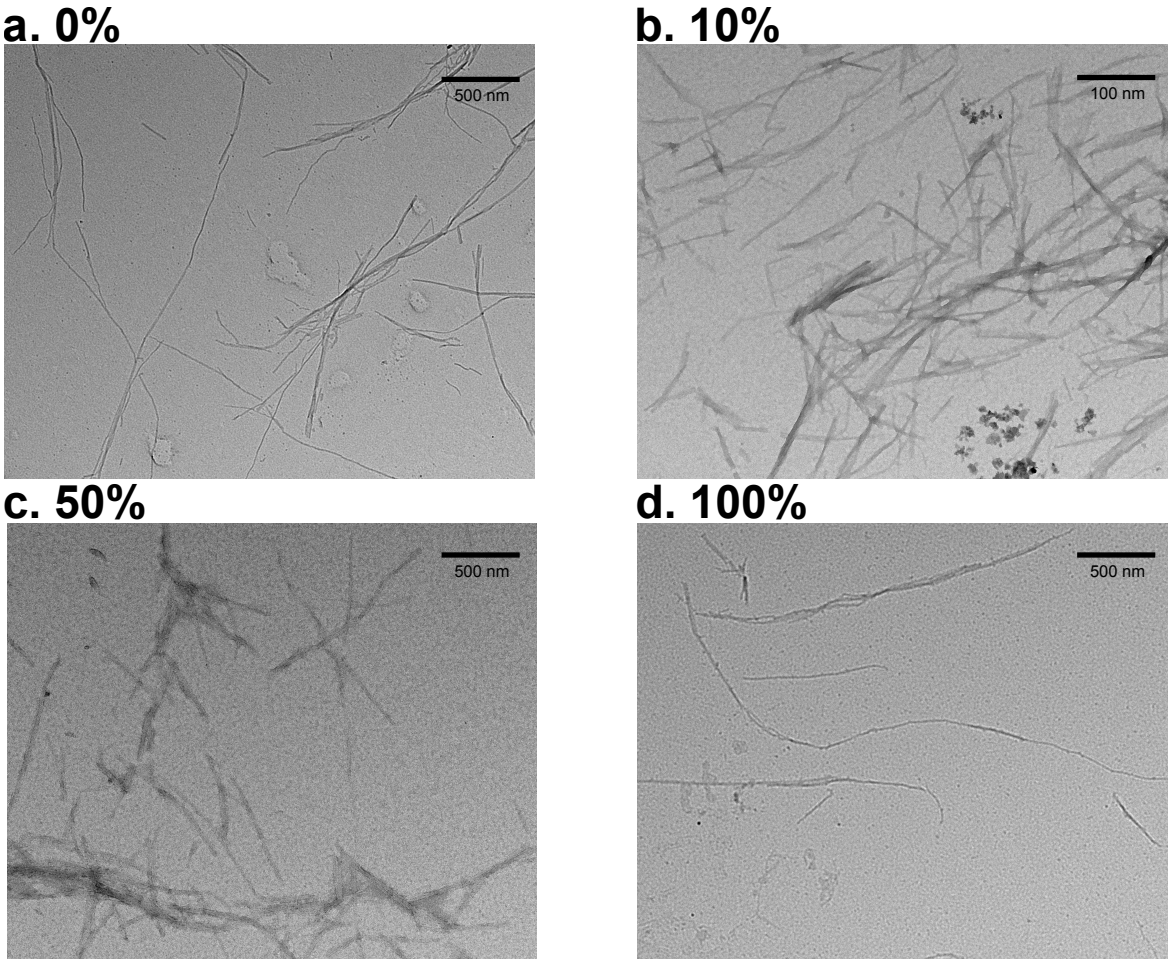

Fig. 6.6 TEM images of insulin fibrils with varying percentage of chaperone relative to insulin concentration a) 0 %, b) 10 %, c) 50 % and d) 100 %.

aggregates and result in an extended lag time, than the interaction with fibrils where it would affect the elongation rate.

Figure 6.6 shows the TEM images of the insulin fibrils in the absence and presence of the chaperones. The insulin fibrils in the absence of the chaperone are overall longer than the fibrils with aBC, but with increasing concentration of the chaperone the fibrils seem to form less clumps than with lower concentrations of the chaperone.

Previous studies with insulin [225], aSyn [223], and Aβ [224, 240] have shown that aBC prevents fibril growth by binding to the fibril ends. Some studies have shown that aBC can suppress the aggregation of aSyn from its earliest growth stages most likely by binding to partially folded monomers [241]. However, it has been unclear whether this molecular chaperone plays a role in the primary nucleation. The dynamic structure of the aBC oligomers varies strongly with solution conditions and, in this case, previous studies were conducted

under acidic pH where both insulin and the chaperone are charged and promote other forms of interactions rather than chaperone-fibrils ends only. The delay in the primary nucleation rate may suggest the chaperone either interacts with the monomeric insulin by assisting in its folding, or interacts with the intermediate oligomeric species, preventing the subsequent formation of the fibrillar species that increase the ThT signal.

6.3.3 Microdroplet experiments

Most of the previous mechanistic studies indicate that aBC plays a role in the elongation step [223–225, 240]. The data obtained from the kinetic measurements performed in this study suggest that the chaperone affect both, the primary nucleation and the elongation rate of insulin aggregation. Microdroplet experiments allow a direct observation of the rare nucleation events in each of the droplets, and thus could provide deeper mechanistic insights into the primary nucleation events. These experiments were challenging mainly because in order to analyse these data in an automated way, it was necessary to obtain droplets which are of monodisperse size in order to determine the reaction volume and surface effects. Moreover, it was also necessary that the droplets in the quartz capillary are in a monolayer to avoid false positives when analysing the fluorescence intensity of each droplet. In order to achieve these requirements, I modified the droplet device to produce larger droplets by using a channel width of 100 μm with flow rate of the aqueous phase of 100-200 μl/h and the flow rate of the oil phase at 2.5 times the flow rate of the aqueous phase. A schematic view of the microchip is presented in Figure 6.7 a. The wider channel produces larger droplets and by occupying a larger volume, they are more likely to be in a monolayer in the quartz capillary. The larger droplet diameter also reduces the aggregation time, because the number of monomers per droplet increases with droplet volume. The microdroplets were treated in the same conditions as in the bulk experiments, i.e. acidic pH and 60°C, and therefore they were trapped in a quartz capillary (Figure 6.7 c) to prevent evaporation over the incubation period. The automated stage of the epifluorescent microscope built by Dr Christopher Taylor shown in Figure 6.8, allows movement to change the position of the glass slide with the capillaries, making it possible to take images of the droplets along the full length of multiple capillaries with different chaperone concentrations in parallel. Usually each condition was repeated in 3-4 capillaries, and four different conditions (insulin and insulin mixed with increasing chaperone molar ratios) to obtain 12 to 16 capillaries to track in total. In the first control experiments aBC alone was also studied but never shown signs of aggregation (an indicative ThT signal was not observed).

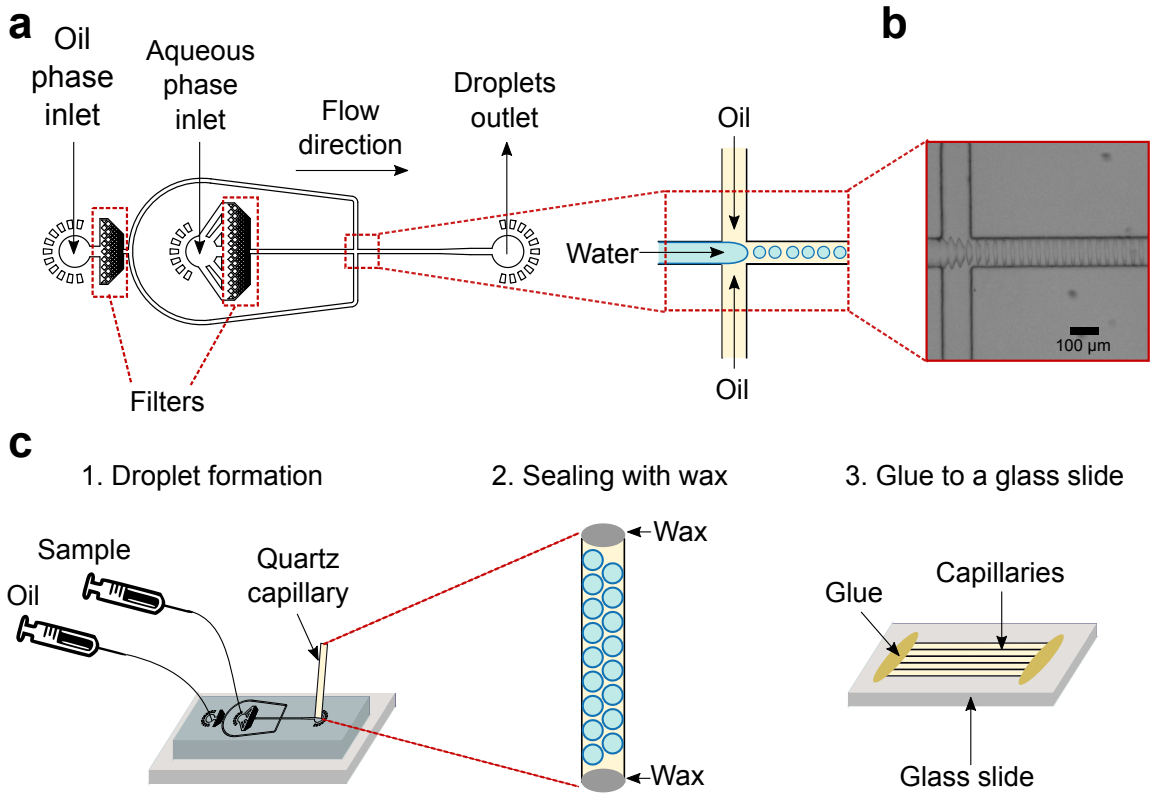

Fig. 6.7 Schematic description of the microdroplet production for kinetics tracking. a) The microfluidic device has two inlets, with the outer one for the oil phase and the inner one for the aqueous phase. The microdroplets are formed at the T-junction of the device and flow to the outlet. b) Brightfield image of the droplets production. c) The microdroplets are collected in a quartz capillary, which are sealed with wax and then glued to a glass slide, for observation under the epifluorescence microscope.

Another challenge presented during these studies was that due to confinement in small volumes, the experiment takes place over the course of four days, in which the droplets can move around in the capillary. Since the droplets are not completely immobilised, it is challenging to track the fluorescence intensity of each droplet over time in, an automated way. By aditionally taking brightfield images at each position, this mobile stage makes it possible to track the position of every droplet if they move from the original position, as well as identify if there is evaporation which can cause the droplets to shrink.

Microdroplets with different insulin concentrations were generated in order to determine the optimal concentration of insulin that aggregates within a reasonable amount of time (ideally less than 5 days). Figure 6.9 shows the effect of concentration and time on aggregation process, observed in microdroplets. Note that at a concentration of protein of 1744 μM (10 mg/ml), the aggregation happens within 30 h, and in principle this high concentration could

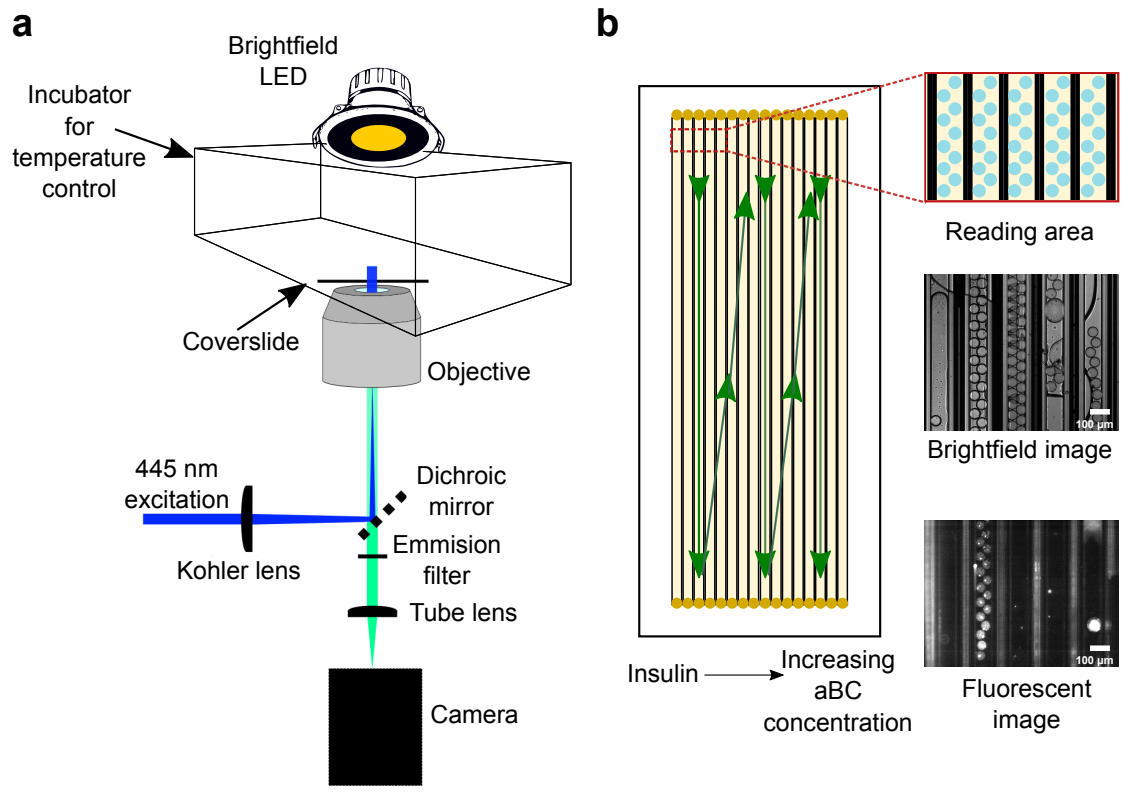

Fig. 6.8 Schematic illustration of the automatic stage used for imaging the droplets in the quartz capillaries. a) Epifluorescent setup built by Dr Christopher Taylor. Image provided by Dr Christopher Taylor. The glass slide with the capillaries is inside an incubator which enables control of the temperature and the brightfield and fluorescent images to be taken at different positions over time. b) A schematic of the reading area and examples of the brightfield and fluorescent images taken each frame. The green arrows indicate the movement of the automatic stage which allows the tracking the entire set capillaries, filled with different solutions of insulin and insulin with aBC.

be selected to have faster results. However, in practice this concentration of insulin showed that after addition of the chaperone, the aggregation rate was accelerated instead of delayed, even under bulk conditions. As described in Section 6.3.1, a mechanism was described for insulin within a range of concentrations from 70 to 349 μM, and for purposes of comparison, the experiments in microdroplets were conducted within the same concentration range.

The experiments of insulin in the presence of aBC seem to show that the chaperone accelerates the aggregation of the hormone even at low concentrations. Figure 6.10 shows the intensity map of four different capillaries tracked in the same experiment, each of them with the same insulin concentration (349 μM) but different molar ratios of aBC from 0 to 50%. Surprisingly, the last capillaries to aggregate were the ones that contain only insulin, and the first to aggregate are the ones with aBC at 10%. What is also interesting about

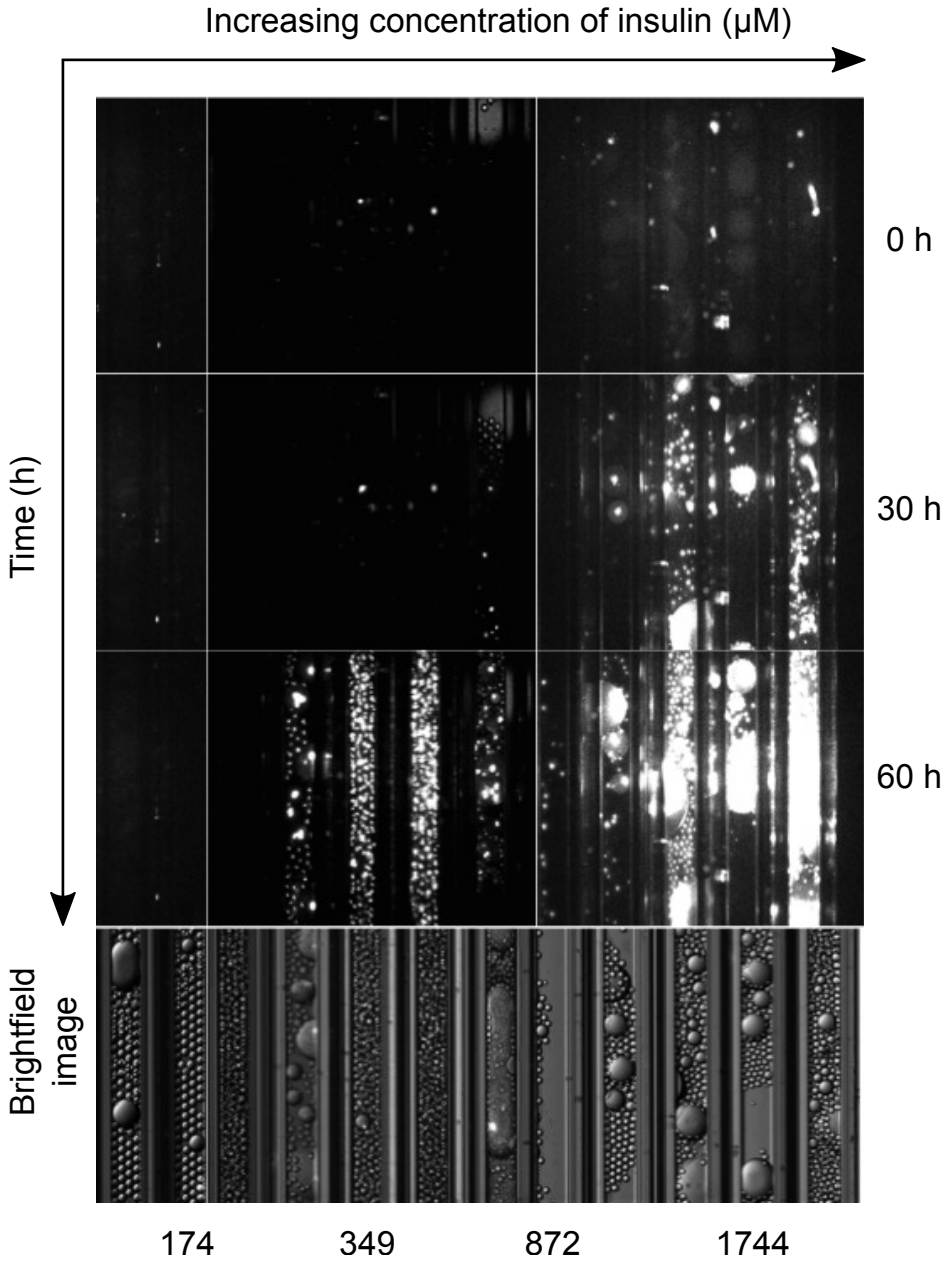

Fig. 6.9 Aggregation of insulin in microdroplets, at different monomer concentrations. Image sections of the capillaries containing microdroplets with different monomeric insulin concentrations from 174 to 1744 μM (x-axis), at different times (y-axis) monitored by ThT fluorescence. The experiment was conducted to select an adequate insulin concentration to test with aBC. While the highest concentration shows aggregation within 20 h, the lowest concentration (174 μM) has not aggregated at 60 h.

this experiment is the presence of a "propagation-like" behaviour, as the droplets seem to aggregate one after another, in all the capillaries.

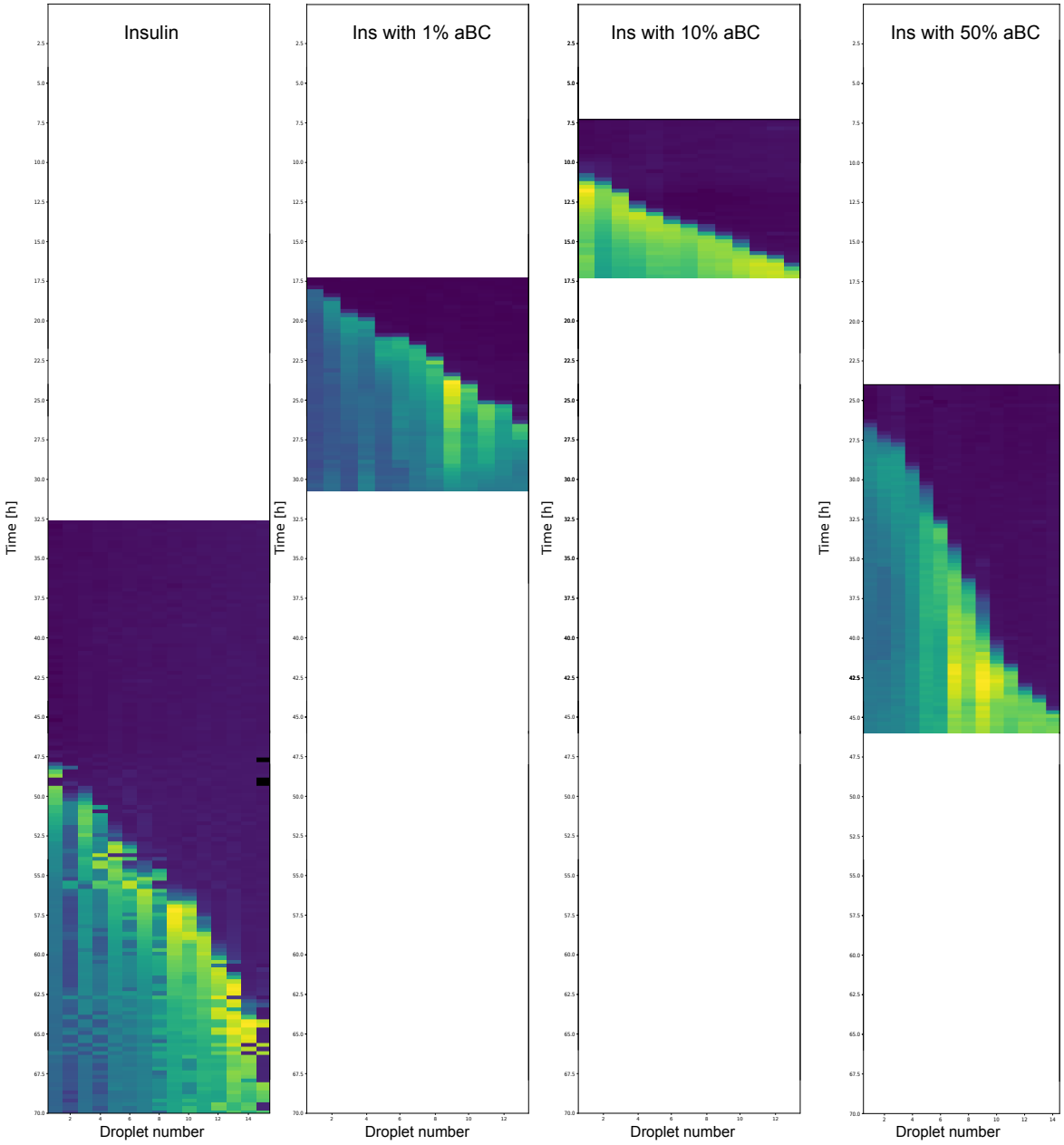

Fig. 6.10 Fluorescence intensity map of insulin aggregation in the absence and presence of aBC. Each of the maps represents a different capillary, from left to right: insulin, insulin with 1% aBC, insulin with 10% aBC and insulin with 50% aBC. The y-axis shows the time and the x-axis represents a different droplet. Note that the capillary with insulin alone is the last one to aggregate. While the capillaries with aBC aggregate faster, there is no trend that correlates with the concentration of the chaperone, and the capillary with insulin with 10% chaperone was the first one to aggregate. Note that there also seems to be propagation between the droplets, i.e. one droplet aggregates after another, each separated by 1-2 h. The intensity of the pixels represents the fluorescence intensity, which in some cases decreases mainly due to photobleaching.

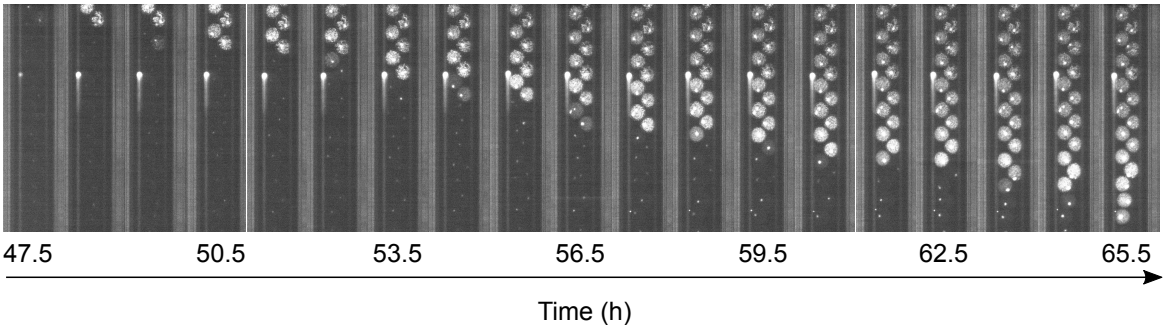

Fig. 6.11 The droplets show a "propagation-like" effect in one direction, one droplet aggregates after another over the course of one hour.

Figure 6.11 shows different frames of the capillary with insulin alone, which starts aggregating from the droplet in the top of the capillary and propagates to the adjacent one over the course of one hour.

The experiment with microdroplets should be validated, by perhaps testing higher concentrations of insulin with multiple molar ratios of aBC, from extremely low to high ratios. The fact that the chaperone seems to accelerate, rather than deacelerate aggregation in the microdroplets under these conditions could have a number of explanations. Firstly, the surface-to-volume ratio of the droplets is larger than in bulk, and therefore the surface interaction in these experiments may play an important role. In addition to the surface-to-volume ratio, the interface in the microdroplets is completely different to that in bulk, due the presence of the fluorinated oil as well as the fluorosurfactant that keeps the droplets stable for days. For these experiments, a concentration of 4%(w/v) was necessary to prevent the droplets from coalescing. Furthermore, in microdroplets there is no water-air interface. Finally, the extreme conditions at which the experiments were performed (pH 1.4 and 60°C) may affect the structure of the proteins after 20 h. Even though aBC does not show ThT fluorescence signal neither in bulk nor in microdroplets, the protein could still denature or dissociate to smaller fragments that, rather than delay aggregation, may accelerate by co-aggregating with insulin. Previous studies have shown that while aBC exists as large oligomeric aggregates at physiological pH, at acidic pH values below 3.4 the chaperone dissociates into denatured polypeptides [242]. Insulin can also undergo hydrolysis at acidic pH and high temperatures such as 105 °C [243, 244]. Further studies with SDS-PAGE and mass spectrometry, after the incubation of the droplets, could be performed to confirm the hydrolysis of either of the proteins in the microdroplets.

The "propagation-like" effect observed in the microdroplets as the intensity map shows in Figure 6.10, indicates that there is either a thermal propagation effect with the exothermic

heat of the aggregation process affecting the nearest droplets, or some of the aggregates are able to interact with the interface of the droplets, which favours the nucleation process in the adjacent one. What is extremely interesting in this case is that aggregation occurs in the same direction in all cases, from top to bottom of the capillary, even though the nucleation events of each capillary start at different times. One possibility is that there was air in one side of the capillaries and this created an air-water interface with one of the droplets, which propagates in one direction. Again, these experiments should be validated in order to make the nucleation events of the droplets independent, with a microfluidic array that traps the droplets and keeps them static to observe them during the incubation time [245]. These traps are usually fabricated in PDMS and the reason why such arrays were not used in this study is because PDMS is permeable to water [246], which would cause the droplets to shrink or even completely dry after a certain incubation time. This array could be optimised for the parallel incubation of multiple droplets at a time, and could be adapted for longer incubation times by placing a glass slide on top of the chamber before curing the PDMS, and by decreasing the incubation time with a higher concentration of protein and salt.

Overall, this experiment should be validated and if indeed the chaperone happens to accelerate the aggregation process of insulin in microdroplets, further experiments of protein stability under these conditions should be performed. The chaperone proamyloidogenic effect has been reported for clusterin [247] when the substrate protein is in a very large molar excess. The acceleration effect of α-Crystallin has also been reported for insulin aggregation in the presence of a reducing agent [248]. The effect of the oil with the fluorosurfactant should also be tested in a bulk experiment, by adding the oil on top of the sample in the microplate to see whether the change in the interface has an effect on the aggregation rate. But in general, this experiment should be optimised to track the full aggregation process in less than 24 h, perhaps with the addition of a high concentration of salt. The aggregation processes are extremely sensitive to changes in ionic strength as well as pH, and therefore these factors should be the same in each of the solutions to have the same conditions in each of the protein mixtures. If conditions were found where the aggregation process in the droplets occurs in less than 24 h, a microfluidic trap could be used instead of a quartz capillary. The use of the microfluidic trap would not only ensure that the nucleation events in each droplet are independent of each other, but also it would make the data analysis easier as so far the quartz capillary presents multiple disadvantages, such as droplet movement, air introduction and in some cases, false positives when the droplets are not in a monolayer.

6.4 Conclusions

Insulin fibrillation has been studied at acidic pH and 60° C, in which the acidic pH induces aggregation most likely by dissociation of native associations (e.g. dimer) and unfolds the monomer and makes it more aggregation-prone. In this case, the model which describes the aggregation of insulin under these conditions involves saturating elongation and fragmentation processes, which is in good agreement with previous studies of insulin. This has allowed for the study of the system in the presence of the chaperone aBC, by perturbation of the original system and simulations that determine which of the rate constants are the most affected. The nucleation rate (k_+) seems to be more notably affected by the chaperone, but the elongation rate could also be affected, although the predictions indicate that mostly primary nucleation is delayed.

The microdroplet experiments show that the chaperone may accelerate insulin self-assembly under these conditions, but further experiments should be conducted in order to validate or disprove these results. Nevertheless, the microfluidic device and automatic stage had been optimised to have an automated data analysis which can provide information on a larger set of data to study stochastic effects.

Chapter 7

Conclusions

7.1 Immuno Diffusional Sizing

The aim of this thesis was to develop and use novel microfluidic techniques to study the species and processes involved in amyloidogenic protein aggregation. I have optimised a microfluidic device for its use with immunoassays. By combining these two techniques, I have developed a powerful tool for studying disease-related proteins in biologically-relevant conditions. The method presented here, Immuno Diffusional Sizing, has been determined to be very sensitive and very specific due to the use of fluorescently-labelled antibodies. The low volume requirements of the microfluidic system, in addition to the low concentrations needed for IDS experiments, means that the technique developed is perhaps one of the sizing methods with the lowest sample consumption to date.

The key advantage of this method is its potential to be used with complex biological samples, such as brain homogenates, as in many cases purification of a target protein is not always easy. In this case, the developed platform was applied to the prion protein, which has been traditionally difficult to analyse. Nevertheless, the method is limited by the availability of specific antibodies for PrP^{Sc}, which made the experiments limited to the resistant form of the infectious prion, PrP^{res}. However, the size determined of PrP^{res} is substantially larger than the one of PrP^{C}, but smaller than the size of a fibril, which indicates this particle is a pre-fibrillar aggregate.

The developed technique has further been applied for a wide range of applications, not only for the direct measurement of amyloidogenic monomers and oligomers, but also shows great potential for sizing on-pathway oligomers, as well as post-translational modifications. As in the case of the prion, the main limitation for studying Aβ40 oligomers was the lack of an antibody pair specific for the aggregated forms of the peptide. Yet, in the case of aSyn, we

have demonstrated that the measurement of oligomers is substantially easier with such a pair, and has potential to study on-pathway oligomers as well as in biological fluids, such as CSF. The limitation on the availability of a TR-FRET pair can be overcome by using his-tagged proteins, because there are many anti-his tag pairs commercially available in the market.

Even though the hydrodynamic radius does not provide as detailed information as high-resolution techniques, such as NMR or X-Ray crystallography, it may be applied for determining the parameters of the aggregation state which can be obtained directly after an aggregation reaction for instance.

7.2 Towards TR-FRET on-chip detection

In this work, two different commercial immunoassays for human insulin were compared by varying different parameters such as antibody concentration, incubation time and temperature. Overall, alphaLISA performed better than TR-FRET in terms of sensitivity. However, the TR-FRET is still more suitable to adapt to on-chip assays, as it is a one-step assay. We have designed and implemented a platform to detect the TR-FRET within a microfluidic device, but no FRET signal was observed by imaging the microchannel with the camera and with the PMT. This may be resolved by performing time-resolved analysis, similar to the approach taken for the platereader experiments. The device suggested here is the one used for IDS, with H-filter geometry, but with modifications to add the antibody pair and mix it with each of the separated fractions to make the detection just after separation. A key advantage of such a device would be the reduction in the time-measurement. Nevertheless, calibration against at least two known concentrations should be performed simultaneously to avoid potential errors generated by the time dependency of the signal.

7.3 Chaperone interactions with insulin

The global kinetic analysis of the insulin data reveals that the hormone follows a mechanism of fragmentation with saturating elongation at relatively high concentrations up to 349 μM. By correctly describing the molecular mechanism of insulin assembly, I have been able to predict what happens when an inhibitor is present during the process of fibril growth. Previous studies have reported that the chaperone aBC plays an important role by suppressing fibril elongation, but a complete description of the role of aBC in primary nucleation has been absent. Adding the chaperone delays the self-assembly of insulin by preventing primary nucleation at acidic pH. The predictions with simulations show that this mechanism describes

the experimental data. It may occur by either interaction of the chaperone with the insulin monomer which prevents it from self-associating, or by interaction of aBC with the pre-fibrillar, oligomeric species and preventing their transition to mature fibrils.

The data obtained with microdroplets shows that the chaperone may have an acceleration rather than inhibition role in the process of insulin aggregation in small volumes, such as the ones of microdroplets. These conditions differ to those in bulk, not only by the volume and the volume-to-surface ratio, but also in the kind of interface as well as the number of nuclei available. While in bulk experiments the interface is water-air in the surface and water-polyestyrene in the sides and bottom of the microwells, in microdroplets the interface is mostly fluorinated oil and fluorosurfactant. The confinement of protein in small volumes significantly delays the rate of aggregation, which occurs within a couple of hours in bulk and in a minimum of three days in the droplets. This made the experiments with the chaperone quite challenging as finding conditions where the chaperone has a visible effect on the insulin self-assembly, but happens during a reasonable time-scale requires optimisation. Further experiments should be performed to confirm or disprove this effect.

7.4 Outlook

7.4.1 IDS

We have optimised and implemented a device suitable to separate molecules and collect them for analysis with immunochemistry.

A clear improvement to the IDS method would be to develop a correct optics setup to be able to perform the diffusion and the immunodetection on the same chip, which would not only save time but would also decrease the sample consumption and probably decrease the error in measurements. However, in some cases the immunoassays require either long incubation times or a pre-treatment before analysis with the antibodies. For example, in the TR-FRET assays to detect PrP^{C}, an overnight incubation stabilised significantly the signals and reduced the standard deviation of each sample. In the case of PrP^{res}, the detection was conducted with an ELISA assay, which requires multiple washing steps, as well as denaturing/re-folding steps that can only be performed off-chip. In these cases, a device that allows collection of a relatively large volume of sample is the preferred one. An interesting experiment with prions would be to determine the infectivity of the separated fractions, because it would provide information whether the larger or smaller species are the most infectious ones.

The device design also expands the application of separation to couple it with several techniques that would otherwise be difficult to perform on-chip. For example, it would be interesting to pre-separate a complex heterogeneous sample before analysis with mass spectrometry, and determine which species are in the high and low-diffusivity fractions. The separation of an heterogeneous sample could also be performed before analysis with AFM, for example, which would therefore allow to resolve which species are present in each of the fractions and if compare the size of them to the average radius provided by diffusional sizing.

In the Aβ40 experiments, the method was coupled to SEC in order to investigate the size of on-pathway oligomers. This separation technique would not be necessary with a FRET pair specific for the oligomers. However, with such a pair, IDS could be coupled to a second microfluidic device that worked as an "oligomer-generator". If the "oligomer-generator" is completely coated with fibrils, monomeric protein can be flowed through it to generate oligomers and by coupling it with IDS, information of the species' size could be obtained. aSyn might be an interesting system to test, because under certain solution conditions its mechanism of aggregation is predominantly by secondary nucleation, and it could be interesting to obtain the size of these secondary nuclei generated in a microfluidic reactor. Besides, the FRET pair for aggregated aSyn is commercially available and would not have interference from the monomeric protein that would be in excess to the oligomers.

Another improvement to this technique would be to couple it with a second separation method in order to resolve all the components in the mixture. For example, it would be interesting to couple it with electrophoretic separation to resolve the size distribution of the components rather than just measuring the average radius. But other separation techniques can be adapted to microfluidics, for example capillary electrophoresis or molecular-affinity extraction [249]. This would also help to perform better analysis of complex samples, such as blood. IDS could also be coupled with a pre-concentration technique, to detect low-concentration analytes, such as the amyloid oligomer species present in CSF.

7.4.2 Towards TR-FRET on-chip detection

The optics for TR-FRET on-chip were tested with a camera and PMT for detection and no FRET signal was observed. The main limitation could be that these readings are performed in a continuous way rather than in a time-resolved manner, as it has been performed in the platereader experiments. The system should be optimised to allow measurements in an automated manner, such as a) the filters of both emission channels are exchanged quickly, and b) the excitation is a pulse and the detection is made just after. In the setup described in

this work, the change of the emission filters was performed manually which could lead to errors when doing a proper measurement, the emission filters should be exchanged rapidly in the order of seconds. The time resolved measurement can be conducted in an automated way by developing a code that controls the excitation source (LED) and the detection system (camera/PMT). Such control could be developed with a script in python, for example. The excitation source could also be exchanged for a laser rather than a LED, to enhance sensitivity.

The microfluidic device suggested in this work for IDS with on-chip detection integrates two detection chambers for each of the separated fractions. The geometry of the chambers is designed in order to have a uniform signal in the whole detection area. The TR-FRET signal for insulin was observed in the platereader even after 5 minutes of mixing it with the antibodies, but in the microfluidic device it might be possible to detect immediately after mixing. A design than enhances mixing could also be implemented in the device to observe signal faster and this would open vast possibilities to study the kinetics of the antigen binding to antibodies.

7.4.3 Insights into the role of aBC in insulin aggregation

The microdroplets experiments have not yet confirmed if aBC indeed plays an important role in the primary nucleation rate. Further experiments could be performed to understand in detail the main interactions of aBC with the different species of insulin formed during the aggregation process. For example, it could be interesting to determine the binding constants of aBC with insulin monomers, oligomers and fibrils at the same pH conditions to determine which interaction is the strongest. Another possible experiment is the addition of a significant amount of seeds (above 40%), in which the role of primary nucleation can essentially be neglected, and then aBC would only inhibit the elongation rate. It would be interesting to prove if the delay of the chaperone is significantly affected or the main role of the chaperone is with pre-fibrillar species.

Further experiments should be performed in order to prove or disprove the acceleration effect of the chaperone on the microdroplets. It may even be possible that after a certain time, instead of denaturing, a fraction of either of the proteins is hydrolysed and the fragments co-aggregate and the effect of acceleration is mainly due to co-aggregating species. Experiments with SDS-PAGE and mass spectrometry could help to understand if indeed the proteins are hydrolysing or co-aggregating.

The “propagation-like” effect in the droplets could be avoided by doing the experiment in a microfluidic array that keeps the droplets spatially separated. If such a device is fabricated

with a glass slide on top of the channels, evaporation could be reduced and with concentrations of protein and salt high enough to observe the aggregation within a couple of hours, the data analysis of the droplets may even be easier than the current system of the quartz capillary.

In general, the concentrations and conditions used in this study could be optimised to reach aggregation within a couple of hours instead of days. This would avoid several drawbacks such as data analysis problems, and undesirable effects in the proteins like hydrolysis. It would also be interesting to apply the droplets to other proteins and inhibitors, for example with the Aβ peptide in the presence of small molecules which are specific for primary nucleation [21].

Appendix A

A.1 Calculation of Net FRET signal of the POM FRET labelled antibodies

PrP experiments were done with Eu-POM1 and APC-POM19 antibodies. The sample was measured in quadruplet wells. The Net-FRET of each well were obtained by backgroung substraction (P-value) with the following expressions:

$$\text{P-value} = \frac{\text{APC channel}}{\text{Eu channel}} \tag{A.1}$$

$$\text{APC channel} = Mean_{\text{APC alone}} - Mean_{\text{Detection buffer}} \tag{A.2}$$

$$\text{Eu channel} = Mean_{\text{Eu alone}} - Mean_{\text{Detection buffer}} \tag{A.3}$$

$$\text{Net FRET} = [\text{APC channel}] - P \times [\text{Eu channel}] \tag{A.4}$$

$$[\text{APC channel}] = Value - Mean_{\text{APC alone}} \tag{A.5}$$

$$[\text{Eu channel}] = Value - Mean_{\text{Detection buffer}} \tag{A.6}$$

A.2 RML-BH digestion conditions

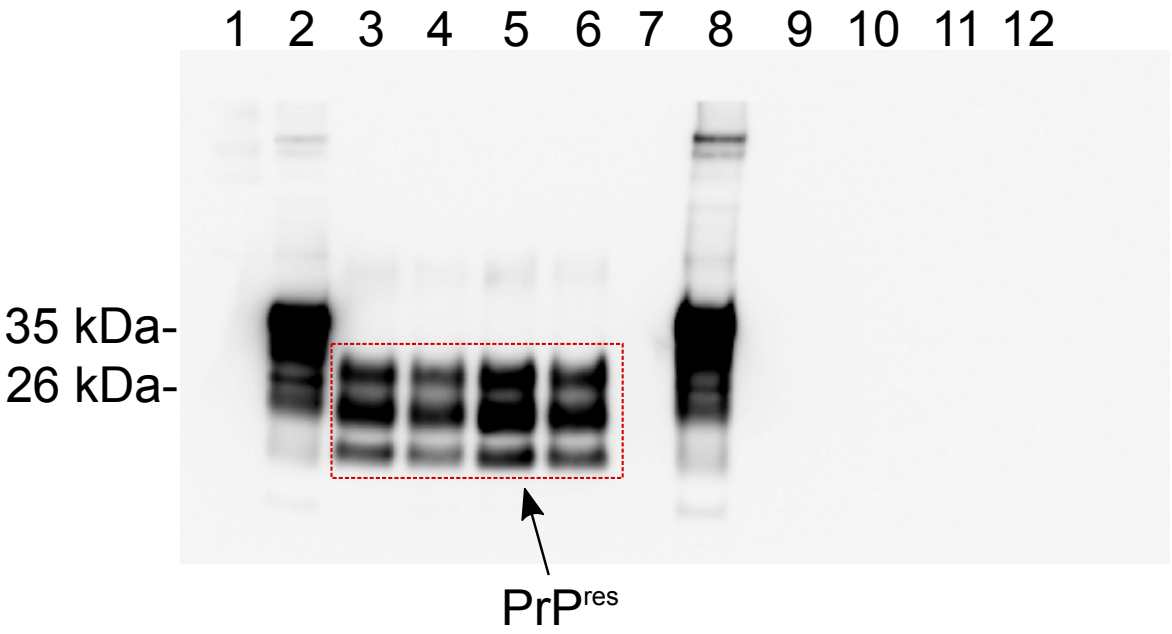

Fig. A.1 Western Blot of digested Tg20-RML and Tg20 BH at different PK concentrations and incubation times, details of the samples are shown in Table A.1. Detection antibodies are POM-1 pool in TopBlock 1%/PBS-T and HRP-Goat anti mouse IgG in TopBlock 1%. The selected fractions for the experiment were 3 and 4.

Gel position	1	2	3	4	5	6
Sample	Marker	Tg20 RML	Tg20 RML	Tg20 RML	Tg20 RML	Tg20 RML
10% BH/μl		3	17.5	17.5	17.5	17.5
PK conc/μg/ml		non	25	50	25	50
Inc. time/hrs		non	2	2	4	4
Gel position	7	8	9	10	11	12
Sample	Marker	Tg20	Tg20	Tg20	Tg20	Tg20
10% BH/μl		3	17.5	17.5	17.5	17.5
PK conc/μg/ml		non	25	50	25	50
Inc. time/hrs		non	2	2	4	4

Table A.1 Different conditions of Proteinase-K concentration and incubation times for RML BH digestion.

Appendix B

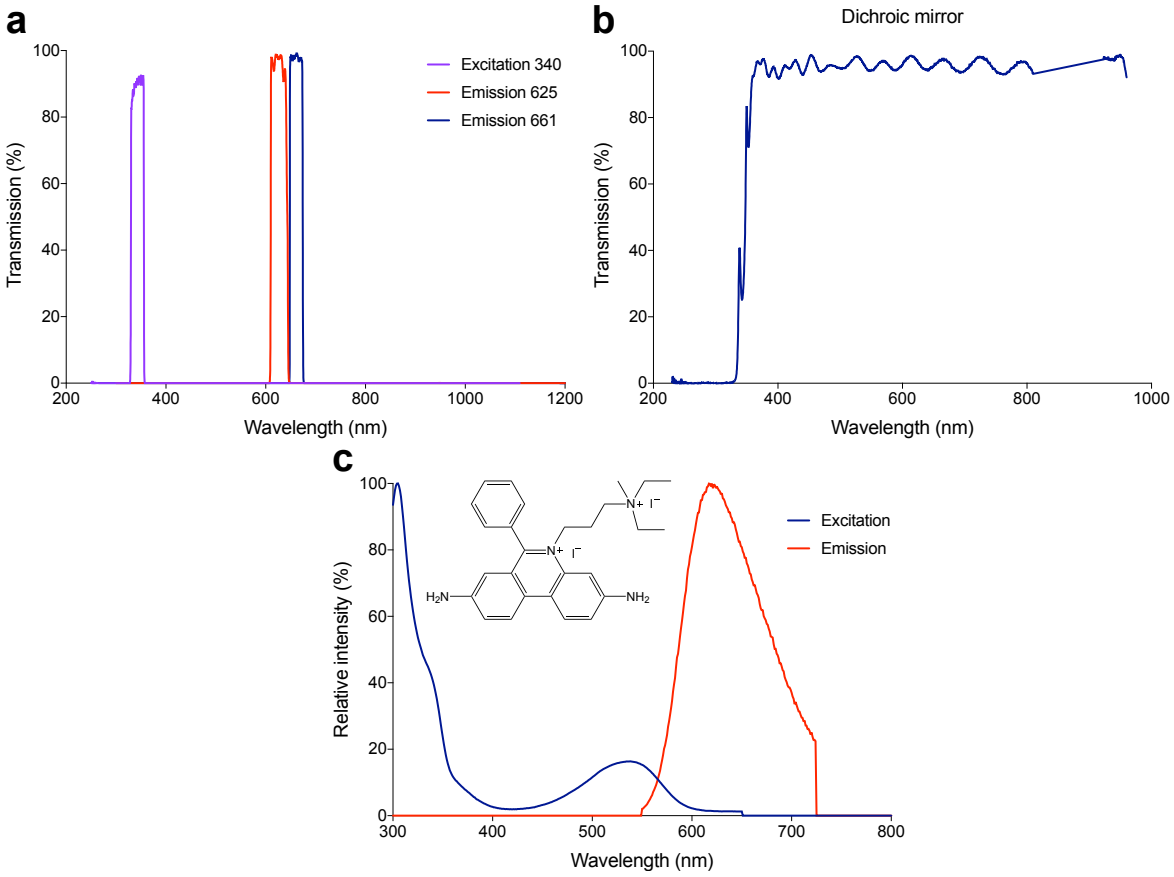

Fig. B.1 Spectra of the filters and calibration dye used to build a FRET setup. a) Excitation filter LP 341 nm, and singleband emission filters 625/15 nm and 661/25 nm, b) Dichroic mirror and c) propidium iodide excitation and emmision spectra.

References

[1] Dill, K. A., Ozkan, S. B., Shell, M. S. & Weikl, T. R. The protein folding problem. *Annu. Rev. Biophys.* **37**, 289–316 (2008).

[2] Baker, D. A surprising simplicity to protein folding. *Nature* **405**, 39–42 (2000).

[3] Zwanzig, R., Szabo, A. & Bagchi, B. Levinthal's paradox. *Proc. Natl. Acad. Sci.* **89**, 20–22 (1992).

[4] Creighton, T. E. Protein folding: An unfolding story. *Curr. Biol.* **5**, 353–356 (1995).

[5] Jahn, T. R. & Radford, S. E. Folding versus aggregation: Polypeptide conformations on competing pathways. *Arch. Biochem. Biophys.* **469**, 100–117 (2008).

[6] Zimmerman, S. B. & Trach, S. O. Estimation of macromolecule concentrations and excluded volume effects for the cytoplasm of Escherichia coli. *J. Mol. Biol.* **222**, 599–620 (1991).

[7] Ciryam, P., Kundra, R., Morimoto, R. I., Dobson, C. M. & Vendruscolo, M. Supersaturation is a major driving force for protein aggregation in neurodegenerative diseases. *Trends Pharmacol. Sci.* **36**, 72–77 (2015).

[8] Knowles, T. P. J., Vendruscolo, M. & Dobson, C. M. The amyloid state and its association with protein misfolding diseases. *Nat. Rev. Mol. Cell Biol.* **15** (2014).

[9] Hartl, F. U., Bracher, A. & Hayer-Hartl, M. Molecular chaperones in protein folding and proteostasis. *Nature* **475**, 324–332 (2011).

[10] Kim, Y. E., Hipp, M. S., Bracher, A., Hayer-Hartl, M. & Ulrich Hartl, F. Molecular chaperone functions in protein folding and proteostasis. *Annu. Rev. Biochem.* **82**, 323–355 (2013).

[11] Amm, I., Sommer, T. & Wolf, D. H. Protein quality control and elimination of protein waste: The role of the ubiquitin–proteasome system. *Biochim. Biophys. Acta - Mol. Cell Res.* **1843**, 182–196 (2014).

[12] Kenney, J. M., Knight, D., Wise, M. J. & Vollrath, F. Amyloidogenic nature of spider silk. *Eur. J. Biochem.* **269**, 4159–4163 (2002).

[13] Michaels, T. C. T., Liu, L. X., Meisl, G. & Knowles, T. P. J. Physical principles of filamentous protein self-assembly kinetics. *J. Phys. Condens. Matter* **29**, 153002 (2017).

[14] Chiti, F. & Dobson, C. M. Protein misfolding, amyloid formation, and human disease: a summary of progress over the last decade. *Annu. Rev. Biochem.* **86**, 27–68 (2017).

[15] Valastyan, J. S. & Lindquist, S. Mechanisms of protein-folding diseases at a glance. *Dis. Model. Mech.* **7**, 9–14 (2014).

[16] Ingram, V. M. Gene mutations in human hæmoglobin: the chemical difference between normal and sickle cell hæmoglobin. *Nature* **180**, 326–328 (1957).

[17] Alzheimer, A., Stelzmann, R. A., Schnitzlein, H. N. & Murtagh, F. R. An English translation of Alzheimer's 1907 paper, "Uber eine eigenartige Erkankung der Hirnrinde". *Clin. Anat.* **8**, 429–431 (1995).

[18] Masters, C. L. *et al.* Amyloid plaque core protein in Alzheimer disease and Down syndrome. *Proc. Natl. Acad. Sci.* **82**, 4245–4249 (1985).

[19] Castro, D. M., Dillon, C., Machnicki, G. & Allegri, R. F. The economic cost of Alzheimer's disease: Family or public health burden? *Dement. Neuropsychol.* **4**, 262–267 (2010).

[20] Aguzzi, A. & O'Connor, T. Protein aggregation diseases: pathogenicity and therapeutic perspectives. *Nat. Rev. Drug Discov.* **9**, 237–248 (2010).

[21] Habchi, J. *et al.* An anticancer drug suppresses the primary nucleation reaction that initiates the production of the toxic Aβ42 aggregates linked with Alzheimer's disease. *Sci. Adv.* **2** (2016).

[22] Vargas, J. Y., Grudina, C. & Zurzolo, C. The prion-like spreading of α-synuclein: From in vitro to in vivo models of Parkinson's disease. *Ageing Res. Rev.* **50**, 89–101 (2019).

[23] Polymeropoulos, M. H. *et al.* Mutation in the α-synuclein gene identified in families with Parkinson's disease. *Science* **276**, 2045–2047 (1997).

[24] Uversky, V. N., Oldfield, C. J. & Dunker, A. K. Intrinsically disordered proteins in human diseases: Introducing the D2 concept. *Annu. Rev. Biophys.* **37**, 215–246 (2008).

[25] Aguzzi, A. & Heikenwalder, M. Pathogenesis of prion diseases: current status and future outlook. *Nat. Rev. Microbiol.* **4**, 765–775 (2006).

[26] Bechtel, K. & Geschwind, M. D. Ethics in prion disease. *Prog. Neurobiol.* **110**, 29–44 (2013).

[27] Wille, H. & Requena, J. R. The structure of PrP^{Sc} prions. *Pathog.* **7**, 20 (2018).

[28] Weissmann, C. The state of the prion. *Nat. Rev. Microbiol.* **2**, 861–871 (2004).

[29] Aguzzi, A., Heikenwalder, M. & Miele, G. Progress and problems in the biology, diagnostics, and therapeutics of prion diseases. *J. Clin. Invest.* **114**, 153–160 (2004).

[30] Shikama, Y. *et al.* Localized amyloidosis at the site of repeated insulin injection in a diabetic patient. *Intern. Med.* **49**, 397–401 (2010).

[31] Chiti, F. & Dobson, C. M. Amyloid formation by globular proteins under native conditions. *Nat. Chem. Biol.* **5**, 15–22 (2008).

[32] Fitzpatrick, A. W. P. *et al.* Atomic structure and hierarchical assembly of a cross-β amyloid fibril. *Proc. Natl. Acad. Sci.* **110**, 5468–5473 (2013).

[33] Shewmaker, F., McGlinchey, R. P. & Wickner, R. B. Structural insights into functional and pathological amyloid. *J. Biol. Chem.* **286**, 16533–16540 (2011).

[34] Westermark, P. *et al.* Amyloid: Toward terminology clarification report from the nomenclature committee of the International Society of Amyloidosis. *Amyloid* **12**, 1–4 (2005).

[35] Surguchev, A. & Surguchov, A. Conformational diseases: Looking into the eyes. *Brain Res. Bull.* **81**, 12–24 (2010).

[36] Dahlgren, K. N. *et al.* Oligomeric and fibrillar species of amyloid-β peptides differentially affect neuronal viability. *J. Biol. Chem.* **277**, 32046–32053 (2002).

[37] Ingelsson, M. Alpha-Synuclein oligomers-Neurotoxic molecules in Parkinson's disease and other Lewy body disorders. *Front. Neurosci.* **10**, 408 (2016).

[38] Cukalevski, R. *et al.* The Aβ40 and Aβ42 peptides self-assemble into separate homomolecular fibrils in binary mixtures but cross-react during primary nucleation. *Chem. Sci.* 4215–4233 (2015).

[39] Oosawa, F. & Kasai, M. A theory of linear and helical aggregations of macromolecules. *J. Mol. Biol.* **4**, 10–21 (1962).

[40] Kashchiev, D. Growth probability and formation time of the individual Oosawa-Kasai protein fibril. *Phys. Rev. E* **98**, 12412 (2018).

[41] Ferrone, F. A., Ivanova, M. & Jasuja, R. Heterogeneous nucleation and crowding in sickle hemoglobin: An analytic approach. *Biophys. J.* **82**, 399–406 (2002).

[42] Knowles, T. P. J. *et al.* An analytical solution to the kinetics of breakable filament assembly. *Science* **326**, 1533–1537 (2009).

[43] Cohen, S. I. A., Vendruscolo, M., Dobson, C. M. & Knowles, T. P. J. From macroscopic measurements to microscopic mechanisms of protein aggregation. *J. Mol. Biol.* **421**, 160–171 (2012).

[44] Cohen, S. I. A. *et al.* Proliferation of amyloid-β 42 aggregates occurs through a secondary nucleation mechanism. *Proc. Natl. Acad. Sci.* **110**, 9758–9763 (2013).

[45] Cohen, S. I. A. *et al.* A molecular chaperone breaks the catalytic cycle that generates toxic Aβ oligomers. *Nat. Struct. Mol. Biol.* **22** (2015).

[46] Habchi, J. *et al.* Systematic development of small molecules to inhibit specific microscopic steps of Aβ42 aggregation in Alzheimer's disease. *Proc. Natl. Acad. Sci.* **114**, E200–E208 (2017).

[47] Khurana, R. *et al.* Mechanism of thioflavin T binding to amyloid fibrils. *J. Struct. Biol.* **151**, 229–238 (2005).

[48] Khurana, R., Uversky, V. N., Nielsen, L. & Fink, A. L. Is congo red an amyloid-specific dye? *J. Biol. Chem.* **276**, 22715–22721 (2001).

[49] Timperman, A. T., Khatib, K. & Sweedler, J. V. Wavelength-resolved fluorescence detection in capillary electrophoresis. *Anal. Chem.* **67**, 139–144 (1995).

[50] Challa, P. K. *et al.* Real-time intrinsic fluorescence visualization and sizing of proteins and protein complexes in microfluidic devices. *Anal. Chem.* **90**, 3849–3855 (2018).

[51] Haass, C. & Selkoe, D. J. Soluble protein oligomers in neurodegeneration: lessons from the Alzheimer's amyloid β-peptide. *Nat. Rev. Mol. Cell Biol.* **8**, 101–112 (2007).

[52] Benilova, I., Karran, E. & De Strooper, B. The toxic Aβ oligomer and Alzheimer's disease: an emperor in need of clothes. *Nat. Neurosci.* **15**, 349–357 (2012).

[53] Silveira, J. R. *et al.* The most infectious prion protein particles. *Nature* **437**, 257–261 (2005).

[54] Campioni, S. *et al.* A causative link between the structure of aberrant protein oligomers and their toxicity. *Nat. Chem. Biol.* **6**, 140–147 (2010).

[55] Lindgren, M. & Hammarström, P. Amyloid oligomers: spectroscopic characterization of amyloidogenic protein states. *FEBS J.* **277**, 1380–1388 (2010).

[56] Bemporad, F. & Chiti, F. Protein misfolded oligomers: Experimental approaches, mechanism of Formation, and structure-toxicity relationships. *Chem. Biol.* **19**, 315–327 (2012).

[57] Mannini, B. *et al.* Toxicity of protein oligomers is rationalized by a function combining size and surface hydrophobicity. *ACS Chem. Biol.* **9**, 2309–2317 (2014).

[58] Olzscha, H. *et al.* Amyloid-like aggregates sequester numerous metastable proteins with essential cellular functions. *Cell* **144**, 67–78 (2011).

[59] Lashuel, H. A. & Lansbury, P. T. Are amyloid diseases caused by protein aggregates that mimic bacterial pore-forming toxins? *Q. Rev. Biophys.* **39**, 167–201 (2006).

[60] Bucciantini, M. *et al.* Inherent toxicity of aggregates implies a common mechanism for protein misfolding diseases. *Nature* **416**, 507–511 (2002).

[61] Treusch, S., Cyr, D. M. & Lindquist, S. Amyloid deposits: Protection against toxic protein species? *Cell Cycle* **8**, 1668–1674 (2009).

[62] Pleyer, C., Flesche, J. & Saeed, F. Lysozyme amyloidosis – a case report and review of the literature . *Clin. Nephrol. Case Stud.* **3**, 42–45 (2015).

[63] Michaels, T. C. T. *et al.* Chemical kinetics for bridging molecular mechanisms and macroscopic measurements of amyloid fibril formation. *Annu. Rev. Phys. Chem.* **69**, 273–298 (2018).

[64] Törnquist, M. *et al.* Secondary nucleation in amyloid formation. *Chem. Commun.* **54**, 8667–8684 (2018).

[65] Tosatto, L. *et al.* Single-molecule FRET studies on alpha-synuclein oligomerization of Parkinson's disease genetically related mutants. *Sci. Rep.* **5**, 16696 (2015).

[66] Acharya, K. R. & Lloyd, M. D. The advantages and limitations of protein crystal structures. *Trends Pharmacol. Sci.* **26**, 10–14 (2005).

[67] Yu, H. Extending the size limit of protein nuclear magnetic resonance. *Proc. Natl. Acad. Sci.* **96**, 332–334 (1999).

[68] Frueh, D. P., Goodrich, A., Mishra, S. & Nichols, S. NMR methods for structural studies of large monomeric and multimeric proteins. *Curr. Opin. Struct. Biol.* **23**, 734–739 (2013).

[69] Aebersold, R. & Mann, M. Mass spectrometry-based proteomics. *Nature* **422**, 198–207 (2003).

[70] Bai, X.-C., McMullan, G. & Scheres, S. H. W. How cryo-EM is revolutionizing structural biology. *Trends Biochem. Sci.* **40**, 49–57 (2015).

[71] Cheng, Y., Glaeser, R. M. & Nogales, E. How cryo-EM became so hot. *Cell* **171**, 1229–1231 (2017).

[72] Renaud, J.-P. *et al.* Cryo-EM in drug discovery: achievements, limitations and prospects. *Nat. Rev. Drug Discov.* **17**, 471–492 (2018).

[73] Fitzpatrick, A. W. P. *et al.* Cryo-EM structures of tau filaments from Alzheimer's disease. *Nature* **547**, 185–190 (2017).

[74] Gallagher-Jones, M. *et al.* Sub-ångström cryo-EM structure of a prion protofibril reveals a polar clasp. *Nat. Struct. Mol. Biol.* **25**, 131–134 (2018).

[75] Weber, K. & Osborn, M. The reliability of molecular weight determinations by dodecyl sulfate-polyacrylamide gel electrophoresis. *J. Biol. Chem.* **244**, 4406–4412 (1969).

[76] Kresge, N., Simoni, R. D. & Hill, R. L. SDS-PAGE to determine the molecular weight of proteins: the work of Klaus Weber and Mary Osborn. *J. Biol. Chem.* **281**, e19 (2006).

[77] Pujol-Pina, R. *et al.* SDS-PAGE analysis of Aβ oligomers is disserving research into Alzheimer's disease: appealing for ESI-IM-MS. *Sci. Rep.* **5**, 14809 (2015).

[78] Bitan, G., Fradinger, E. A., Spring, S. M. & Teplow, D. B. Neurotoxic protein oligomers — what you see is not always what you get. *Amyloid* **12**, 88–95 (2005).

[79] Arndt, C., Koristka, S., Bartsch, H. & Bachmann, M. Native polyacrylamide gels BT - Protein electrophoresis: methods and protocols. 49–53 (Humana Press, Totowa, NJ, 2012).

[80] Folta-Stogniew, E. Oligomeric states of proteins determined by Size-Exclusion Chromatography coupled with light scattering, absorbance, and refractive index detectors BT - New and emerging proteomic techniques. *Meth. Mol. Biol.* 97–112 (2006).

[81] Muneeruddin, K., Thomas, J. J., Salinas, P. A. & Kaltashov, I. A. Characterization of small protein aggregates and oligomers using Size Exclusion Chromatography with online detection by native electrospray ionization mass spectrometry. *Anal. Chem.* **86**, 10692–10699 (2014).

[82] Hong, P., Koza, S. & Bouvier, E. S. P. A review Size exclusion chromatography for the analysis of protein biotherapeutics and their aggregates. *J. Liq. Chromatogr. Relat. Technol.* **35**, 2923–2950 (2012).

[83] Du, X. *et al.* Insights into protein–ligand interactions: Mechanisms, models, and methods. *Int. J. Mol. Sci.* **17**, 144 (2016).

[84] Wolff, M. *et al.* Quantitative thermophoretic study of disease-related protein aggregates. *Sci. Rep.* **6**, 22829 (2016).

[85] Lebowitz, J., Lewis, M. S. & Schuck, P. Modern analytical ultracentrifugation in protein science: A tutorial review. *Protein Sci.* **11**, 2067–2079 (2009).

[86] Laue, T. M. & Stafford III, W. F. Modern applications of analytical ultracentrifugation. *Annu. Rev. Biophys. Biomol. Struct.* **28**, 75–100 (1999).

[87] Hassan, P. A., Rana, S. & Verma, G. Making sense of brownian motion: colloid characterization by dynamic light scattering. *Langmuir* **31**, 3–12 (2015).

[88] Whitesides, G. M. The origins and the future of microfluidics. *Nature* **442**, 368–373 (2006).

[89] Velve-Casquillas, G., Le Berre, M., Piel, M. & Tran, P. T. Microfluidic tools for cell biological research. *Nano Today* **5**, 28–47 (2010).

[90] Streets, A. M. & Huang, Y. Chip in a lab: Microfluidics for next generation life science research. *Biomicrofluidics* **7**, 11302 (2013).

[91] Haeberle, S. & Zengerle, R. Microfluidic platforms for lab-on-a-chip applications. *Lab Chip* **7**, 1094–1110 (2007).

[92] Charmet, J., Arosio, P. & Knowles, T. P. J. Microfluidics for protein biophysics. *J. Mol. Biol.* **430**, 565–580 (2018).

[93] Klein, A. M. *et al.* Droplet barcoding for single-cell transcriptomics applied to embryonic stem cells. *Cell* **161**, 1187–1201 (2015).

[94] Yu, J. *et al.* Microfluidics-based single-cell functional proteomics for fundamental and applied biomedical applications. *Annu. Rev. Anal. Chem.* **7**, 275–295 (2014).

[95] Squires, T. M. & Quake, S. R. Microfluidics: Fluid physics at the nanoliter scale. *Rev. Mod. Phys.* **77**, 977–1026 (2005).

[96] Duffy, D. C., McDonald, J. C., Schueller, O. J. A. & Whitesides, G. M. Rapid prototyping of microfluidic systems in poly(dimethylsiloxane). *Anal. Chem.* **70**, 4974–4984 (1998).

[97] Challa, P. K., Kartanas, T., Charmet, J. & Knowles, T. P. J. Microfluidic devices fabricated using fast wafer-scale LED-lithography patterning. *Biomicrofluidics* **11**, 14113 (2017).

[98] Tan, S. H., Nguyen, N.-T., Chua, Y. C. & Kang, T. G. Oxygen plasma treatment for reducing hydrophobicity of a sealed polydimethylsiloxane microchannel. *Biomicrofluidics* **4**, 32204 (2010).

[99] Ahmad, A., Uversky, V. N., Hong, D. & Fink, A. L. Early events in the fibrillation of monomeric insulin. *J. Biol. Chem.* **280**, 42669–42675 (2005).

[100] Bloom, C. R. *et al.* Ligand binding to wild-type and E-B13Q mutant insulins: a three-state allosteric model system showing half-site reactivity. *J. Mol. Biol.* **245**, 324–330 (1995).

[101] Zahn, R., von Schroetter, C. & Wüthrich, K. Human prion proteins expressed in Escherichia coli and purified by high-affinity column refolding. *FEBS Lett.* **417**, 400–404 (1997).

[102] Lysek, D. A. & Wüthrich, K. Prion protein interaction with the C-terminal SH3 domain of Grb2 studied using NMR and optical spectroscopy. *Biochemistry* **43**, 10393–10399 (2004).

[103] Hornemann, S., Christen, B., von Schroetter, C., Pérez, D. R. & Wüthrich, K. Prion protein library of recombinant constructs for structural biology. *FEBS J.* **276**, 2359–2367 (2009).

[104] Polymenidou, M. *et al.* The POM monoclonals: a comprehensive set of antibodies to non-overlapping prion protein epitopes. *PLoS One* **3**, e3872 (2008).

[105] Ballmer, B. A. *et al.* Modifiers of prion protein biogenesis and recycling identified by a highly-parallel endocytosis kinetics assay. *J. Biol. Chem.* **293**, 8356–8368 (2017).

[106] Fischer, M. *et al.* Prion protein (PrP) with amino-proximal deletions restoring susceptibility of PrP knockout mice to scrapie. *EMBO J.* **15**, 1255–1264 (1996).

[107] Mannini, B. *et al.* Stabilization and characterization of cytotoxic Aβ40 oligomers isolated from an aggregation reaction in the presence of zinc ions. *ACS Chem. Neurosci.* 2959–2971 (2018).

[108] Chen, S. W. *et al.* Structural characterization of toxic oligomers that are kinetically trapped during α-synuclein fibril formation. *Proc. Natl. Acad. Sci.* **112**, E1994–E2003 (2015).

[109] Meisl, G. *et al.* Molecular mechanisms of protein aggregation from global fitting of kinetic models. *Nat. Protoc.* **11**, 252–272 (2016).

[110] Pfammatter, M. *et al.* Absolute quantification of amyloid propagons by digital microfluidics. *Anal. Chem.* **89**, 12306–12313 (2017).

[111] Arosio, P. *et al.* Microfluidic diffusion analysis of the sizes and interactions of proteins under native solution conditions. *ACS Nano* **10**, 333–341 (2016).

[112] Yates, E. V. *et al.* Latent analysis of unmodified biomolecules and their complexes in solution with attomole detection sensitivity. *Nat. Chem.* **7**, 802–809 (2015).

[113] Brody, J. P. & Yager, P. Diffusion-based extraction in a microfabricated device. *Sensors Actuators A Phys.* **58**, 13–18 (1997).

[114] Kamholz, A. E. & Yager, P. Theoretical analysis of molecular diffusion in pressure-driven laminar flow in microfluidic channels. *Biophys. J.* **80**, 155–160 (2001).

[115] Kamholz, A. E., Schilling, E. A. & Yager, P. Optical measurement of transverse molecular diffusion in a microchannel. *Biophys. J.* **80**, 1967–1972 (2001).

[116] Hatch, A. *et al.* A rapid diffusion immunoassay in a T-sensor. *Nat. Biotech.* **19**, 461–465 (2001).

[117] Culbertson, C. T., Jacobson, S. C. & Michael Ramsey, J. Diffusion coefficient measurements in microfluidic devices. *Talanta* **56**, 365–373 (2002).

[118] Hatch, A., Garcia, E. & Yager, P. Diffusion-based analysis of molecular interactions in microfluidic devices. *Proc. IEEE* **92**, 126–139 (2004).

[119] Arosio, P., Hu, K., Aprile, F. A., Müller, T. & Knowles, T. P. J. Microfluidic diffusion viscometer for rapid analysis of complex solutions. *Anal. Chem.* **88** (2016).

[120] Zhang, Y. *et al.* Protein aggregate-ligand binding assays based on microfluidic diffusional separation. *ChemBioChem* **17**, 1920–1924 (2016).

[121] Toseland, C. P. Fluorescent labeling and modification of proteins. *J. Chem. Biol.* **6**, 85–95 (2013).

[122] Yin, L. *et al.* How does fluorescent labeling affect the binding kinetics of proteins with intact cells? *Biosens. Bioelectron.* **66**, 412–416 (2015).

[123] Jacobson, S. C., Hergenroder, R., Koutny, L. B. & Ramsey, J. M. High-speed separations on a microchip. *Anal. Chem.* **66**, 1114–1118 (1994).

[124] Zhang, Y. *et al.* On-chip measurements of protein unfolding from direct observations of micron-scale diffusion. *Chem. Sci.* **9**, 3503–3507 (2018).

[125] Roth, M. Fluorescence reaction for amino acids. *Anal. Chem.* **43**, 880–882 (1971).

[126] Lee, K. S. & Drescher, D. G. Fluorometric amino-acid analysis with o-phthaldialdehyde (OPA). *Int. J. Biochem.* **9**, 457–467 (1978).

[127] Müller, T. *et al.* Particle-based simulations of steady-state mass transport at high Peclet numbers. *Int. J. Nonlinear Sci. Numer. Simul.* **17**, 175–183 (2015).

[128] Periasamy, A. Fluorescence resonance energy transfer microscopy: a mini review. *J. Biomed. Opt.* **6**, 287–292 (2001).

[129] Degorce, F. *et al.* HTRF: A technology tailored for drug discovery. A review of theoretical aspects and recent applications. *Curr. Chem. Genomics* **3**, 22–32 (2009).

[130] Cui, X. *et al.* TR-FRET assays of Huntingtin protein fragments reveal temperature and PolyQ length-dependent conformational changes. *Sci. Rep.* **4**, 5601 (2014).

[131] Einhorn, L. & Krapfenbauer, K. HTRF: a technology tailored for biomarker determination-novel analytical detection system suitable for detection of specific autoimmune antibodies as biomarkers in nanogram level in different body fluids. *EPMA J.* **6**, 23 (2015).

[132] Tate, J. & Ward, G. Interferences in Immunoassay. *Clin. Biochem. Rev.* **25**, 105–120 (2004).

[133] Glickman, J. F. *et al.* A comparison of ALPHAScreen, TR-FRET, and TRF as assay methods for FXR nuclear receptors. *J. Biomol. Screen.* **7**, 3–10 (2002).

[134] Piston, D. W. & Kremers, G.-J. Fluorescent protein FRET: the good, the bad and the ugly. *Trends Biochem. Sci.* **32**, 407–414 (2007).

[135] Blundell, T. L. *et al.* The structure and biology of insulin. *Biochem. J.* **125**, 50P–51P (1971).

[136] Jensen, S. S., Jensen, H., Cornett, C., Møller, E. H. & Østergaard, J. Insulin diffusion and self-association characterized by real-time UV imaging and Taylor dispersion analysis. *J. Pharm. Biomed. Anal.* **92**, 203–210 (2014).

[137] Oliva, A., Fariña, J. & Llabrés, M. Development of two high-performance liquid chromatographic methods for the analysis and characterization of insulin and its degradation products in pharmaceutical preparations. *J. Chromatogr. B Biomed. Sci. Appl.* **749**, 25–34 (2000).

[138] Grassia, P. S., Hinch, E. J. & Nitsche, L. C. Computer simulations of Brownian motion of complex systems. *J. Fluid Mech.* **282**, 373–403 (1995).

[139] Kubo, R. Brownian motion and nonequilibrium statistical mechanics. *Science* **123**, 330–334 (1986).

[140] Oh, K. W., Lee, K., Ahn, B. & Furlani, E. P. Design of pressure-driven microfluidic networks using electric circuit analogy. *Lab Chip* **12**, 515–545 (2012).

[141] Bromberg, L., Rashba-Step, J. & Scott, T. Insulin particle formation in supersaturated aqueous solutions of poly(ethylene glycol). *Biophys. J.* **89**, 3424–3433 (2005).

[142] Zeng, W., Jacobi, I., Beck, D. J., Li, S. & Stone, H. A. Characterization of syringe-pump-driven induced pressure fluctuations in elastic microchannels. *Lab Chip* **15**, 1110–1115 (2015).

[143] Aguzzi, A. Beyond the prion principle. *Nature* **459**, 924–925 (2009).

[144] Prusiner, S. B. Novel proteinaceous infectious particles cause scrapie. *Science* **216**, 136–144 (1982).

[145] Imran, M. & Mahmood, S. An overview of human prion diseases. *Virol. J.* **8**, 559 (2011).

[146] Acevedo-Morantes, Y. C. & Wille, H. The structure of human prions: From biology to structural models. Considerations and pitfalls. *Viruses* **6**, 3875–3892 (2014).

[147] Fournier, J.-G., Escaig-Haye, F. & Grigoriev, V. Ultrastructural localization of prion proteins: Physiological and pathological implications. *Microsc. Res. Tech.* **50**, 76–88 (2000).

[148] Riesner, D. Biochemistry and structure of prp^{C} and prp^{Sc}. *Br. Med. Bull.* **66**, 21–33 (2003).

[149] Alper, T., Cramp, W. A., Haig, D. A. & Clarke, M. C. Does the agent of Scrapie replicate without nucleic acid ? *Nature* **214**, 764–766 (1967).

[150] Griffith, J. S. Nature of the Scrapie agent: self-replication and Scrapie. *Nature* **215**, 1043–1044 (1967).

[151] Wulf, M.-A., Senatore, A. & Aguzzi, A. The biological function of the cellular prion protein: an update. *BMC Biol.* **15**, 34–47 (2017).

[152] Soto, C. & Castilla, J. The controversial protein-only hypothesis of prion propagation. *Nat. Med.* **10**, S63–S67 (2004).

[153] Kimberlin, R. H. Scrapie agent: prions or virinos? *Nature* **297**, 107–108 (1982).

[154] Vázquez-Fernández, E. *et al.* The structural architecture of an infectious mammalian prion using electron cryomicroscopy. *PLOS Pathog.* **12**, e1005835 (2016).

[155] Sonati, T. *et al.* The toxicity of antiprion antibodies is mediated by the flexible tail of the prion protein. *Nature* **501**, 102–106 (2013).

[156] Glabe, C. G. Structural classification of toxic amyloid oligomers. *J. Biol. Chem.* **283**, 29639–29643 (2008).

[157] Van Der Kant, R. & Goldstein, L. S. Cellular functions of the amyloid precursor protein from development to dementia. *Dev. Cell* **32**, 502–515 (2015).

[158] Müller, U. C., Deller, T. & Korte, M. Not just amyloid: physiological functions of the amyloid precursor protein family. *Nat. Rev. Neurosci.* **18**, 281 (2017).

[159] Selkoe, D. J. Alzheimer's disease: genes, proteins, and therapy. *Physiol. Rev.* **81**, 741–766 (2001).

[160] Burdick, D. *et al.* Assembly and aggregation properties of synthetic Alzheimer's A4/β amyloid peptide analogs. *J. Biol. Chem.* **267**, 546–554 (1992).

[161] Baumketner, A. *et al.* Amyloid β-protein monomer structure: A computational and experimental study. *Protein Sci.* **15**, 420–428 (2009).

[162] Hardy, J. A. & Higgins, G. A. Alzheimer's disease: the amyloid cascade hypothesis. *Science* **256**, 184–185 (1992).

[163] Rosenblum, W. I. Why Alzheimer trials fail: removing soluble oligomeric beta amyloid is essential, inconsistent, and difficult. *Neurobiol. Aging* **35**, 969–974 (2014).

[164] Kotler, S. A. *et al.* High-resolution NMR characterization of low abundance oligomers of amyloid-β without purification. *Sci. Rep.* **5**, 11811 (2015).

[165] Hane, F. & Leonenko, Z. Effect of metals on kinetic pathways of amyloid-β aggregation. *Biomolecules* **4**, 101–116 (2014).

[166] Bush, A. I. The metallobiology of Alzheimer's disease. *Trends Neurosci.* **26**, 207–214 (2003).

[167] Chen, P., Miah, M. R. & Aschner, M. Metals and neurodegeneration. *F1000Research* **5** (2016).

[168] Bolognin, S. *et al.* Aluminum, copper, iron and zinc differentially alter amyloid-Aβ1–42 aggregation and toxicity. *Int. J. Biochem. Cell Biol.* **43**, 877–885 (2011).

[169] Abelein, A., Gräslund, A. & Danielsson, J. Zinc as chaperone-mimicking agent for retardation of amyloid β peptide fibril formation. *Proc. Natl. Acad. Sci.* **112**, 5407 – 5412 (2015).

[170] Branch, T., Barahona, M., Dodson, C. A. & Ying, L. Kinetic analysis reveals the identity of Aβ-Metal complex responsible for the initial aggregation of Aβ in the synapse. *ACS Chem. Neurosci.* **8**, 1970–1979 (2017).

[171] Tomljenovic, L. Aluminum and Alzheimer's disease: after a century of controversy, is there a plausible link? *J. Alzheimers. Dis.* **23**, 567–598 (2011).

[172] Lovell, M. A., Robertson, J. D., Teesdale, W. J., Campbell, J. L. & Markesbery, W. R. Copper, iron and zinc in Alzheimer's disease senile plaques. *J. Neurol. Sci.* **158**, 47–52 (1998).

[173] Lane, D. J. R., Ayton, S. & Bush, A. I. Iron and Alzheimer's disease: An update on emerging mechanisms. *J. Alzheimers. Dis.* **64**, S379–S395 (2018).

[174] Goedert, M. Alpha-synuclein and neurodegenerative diseases. *Nat. Rev. Neurosci.* **2**, 492–501 (2001).

[175] Dunker, A. K., Silman, I., Uversky, V. N. & Sussman, J. L. Function and structure of inherently disordered proteins. *Curr. Opin. Struct. Biol.* **18**, 756–764 (2008).

[176] Burré, J. The Synaptic Function of α-Synuclein. *J. Parkinsons. Dis.* **5**, 699–713 (2015).

[177] Koichi, W., Kunikazu, T., Fumiaki, M. & Hitoshi, T. The Lewy body in Parkinson's disease: Molecules implicated in the formation and degradation of α-synuclein aggregates. *Neuropathology* **27**, 494–506 (2007).

[178] Flagmeier, P. *et al.* Mutations associated with familial Parkinson's disease alter the initiation and amplification steps of α-synuclein aggregation. *Proc. Natl. Acad. Sci. U. S. A.* **113**, 10328–10333 (2016).

[179] Barrett, P. J. & Timothy Greenamyre, J. Post-translational modification of α-synuclein in Parkinson's disease. *Brain Res.* **1628**, 247–253 (2015).

[180] Schmid, A. W., Fauvet, B., Moniatte, M. & Lashuel, H. A. Alpha-synuclein post-translational modifications as potential biomarkers for Parkinson disease and other synucleinopathies. *Mol. & Cell. Proteomics* **12**, 3543–3558 (2013).

[181] Beyer, K. & Ariza, A. Alpha-Synuclein post-translational modification and alternative splicing as a trigger for neurodegeneration. *Mol. Neurobiol.* **47**, 509–524 (2013).

[182] Iljina, M. *et al.* Kinetic model of the aggregation of alpha-synuclein provides insights into prion-like spreading. *Proc. Natl. Acad. Sci. U. S. A.* **113**, E1206–1215 (2016).

[183] Buell, A. K. *et al.* Solution conditions determine the relative importance of nucleation and growth processes in α-synuclein aggregation. *Proc. Natl. Acad. Sci.* **111**, 7671–7676 (2014).

[184] Galvagnion, C. *et al.* Lipid vesicles trigger α-synuclein aggregation by stimulating primary nucleation. *Nat. Chem. Biol.* **11**, 229–234 (2015).

[185] Fusco, G. *et al.* Direct observation of the three regions in α-synuclein that determine its membrane-bound behaviour. *Nat. Commun.* **5**, 3827 (2014).

[186] Fusco, G. *et al.* Structural basis of membrane disruption and cellular toxicity by α-synuclein oligomers. *Science* **358**, 1440–1443 (2017).

[187] Bartels, T., Choi, J. G. & Selkoe, D. J. α-Synuclein occurs physiologically as a helically folded tetramer that resists aggregation. *Nature* **477**, 107–110 (2011).

[188] Burré, J. *et al.* Properties of native brain α-synuclein. *Nature* **498**, E4–E6 (2013).

[189] Janezic, S. *et al.* Deficits in dopaminergic transmission precede neuron loss and dysfunction in a new Parkinson model. *Proc. Natl. Acad. Sci.* **110**, E4016–E4025 (2013).

[190] Nag, S. *et al.* Nature of the amyloid-β monomer and the monomer-oligomer equilibrium. *J. Biol. Chem.* **286**, 13827–13833 (2011).

[191] Granata, D. *et al.* The inverted free energy landscape of an intrinsically disordered peptide by simulations and experiments. *Sci. Rep.* **5**, 15449 (2015).

[192] Michaels, T. C. T., Lazell, H. W., Arosio, P. & Knowles, T. P. J. Dynamics of protein aggregation and oligomer formation governed by secondary nucleation. *J. Chem. Phys.* **143**, 54901 (2015).

[193] Hölttä, M. *et al.* Evaluating Amyloid-β oligomers in cerebrospinal fluid as a biomarker for Alzheimer's disease. *PLoS One* **8**, e66381 (2013).

[194] Paleologou, K. E. *et al.* Phosphorylation at Ser-129 but not the phosphomimics S129E/D inhibits the fibrillation of α-Synuclein. *J. Biol. Chem.* **283**, 16895–16905 (2008).

[195] Vashist, S. K. & Luong, J. H. T. chap. Lab-on-a-Chip (LOC) Immunoassays, 415–431 (Academic Press, 2018).

[196] Barbosa, A. I. & Reis, N. M. A critical insight into the development pipeline of microfluidic immunoassay devices for the sensitive quantitation of protein biomarkers at the point of care. *Analyst* **142**, 858–882 (2017).

[197] Varghese, S. S., Zhu, Y., Davis, T. J. & Trowell, S. C. FRET for lab-on-a-chip devices - current trends and future prospects. *Lab Chip* **10**, 1355–1364 (2010).

[198] Saraheimo, S. *et al.* Time-resolved FRET -Based approach for antibody detection – A new serodiagnostic concept. *PLoS One* **8**, e62739 (2013).

[199] Sahoo, H. & Schwille, P. FRET and FCS - friends or foes? *ChemPhysChem* **12**, 532–541 (2011).

[200] Knox, R. S. Förster's resonance excitation transfer theory: not just a formula. *J. Biomed. Opt.* **17**, 11003–11007 (2012).

[201] Wu, P. G. & Brand, L. Resonance energy transfer: Methods and applications. *Anal. Biochem.* **218**, 1–13 (1994).

[202] Ma, L., Yang, F. & Zheng, J. Application of fluorescence resonance energy transfer in protein studies. *J. Mol. Struct.* **1077**, 87–100 (2014).

[203] Ullman, E. F. *et al.* Luminescent oxygen channeling immunoassay: measurement of particle binding kinetics by chemiluminescence. *Proc. Natl. Acad. Sci.* **91**, 5426–5430 (1994).

[204] Yasgar, A., Jadhav, A., Simeonov, A. & Coussens, N. P. AlphaScreen-based assays: Ultra-high-throughput screening for small-molecule inhibitors of challenging enzymes and protein-protein Interactions. *Methods Mol. Biol.* **1439**, 77–98 (2016).

[205] Tak For Yu, Z. *et al.* Rapid, automated, parallel quantitative immunoassays using highly integrated microfluidics and AlphaLISA. *Sci. Rep.* **5**, 11339 (2015).

[206] Merchant, K. A., Best, R. B., Louis, J. M., Gopich, I. V. & Eaton, W. A. Characterizing the unfolded states of proteins using single-molecule FRET spectroscopy and molecular simulations. *Proc. Natl. Acad. Sci.* **104**, 1528 – 1533 (2007).

[207] Dittrich, P. S. & Manz, A. Single-molecule fluorescence detection in microfluidic channels—the Holy Grail in μTAS? *Anal. Bioanal. Chem.* **382**, 1771–1782 (2005).

[208] Muchowski, P. J. & Wacker, J. L. Modulation of neurodegeneration by molecular chaperones. *Nat. Rev. Neurosci.* **6**, 11–22 (2005).

[209] Ellis, R. Macromolecular crowding: obvious but underappreciated. *Trends Biochem. Sci.* **26**, 597–604 (2001).

[210] Mannini, B. & Chiti, F. Chaperones as suppressors of protein misfolded oligomer toxicity **10**, 98 (2017).

[211] Kregel, K. C. Invited Review: Heat shock proteins: modifying factors in physiological stress responses and acquired thermotolerance. *J. Appl. Physiol.* **92**, 2177–2186 (2002).

[212] Feder, M. E. & Hofmann, G. E. Heat-shock proteins, molecular chaperones, and the stress response: Evolutionary and ecological physiology. *Annu. Rev. Physiol.* **61**, 243–282 (1999).

[213] Arosio, P. *et al.* Kinetic analysis reveals the diversity of microscopic mechanisms through which molecular chaperones suppress amyloid formation. *Nat. Commun.* **7**, 10948 (2016).

[214] Arosio, P., Meisl, G., Andreasen, M. & Knowles, T. P. J. Preventing peptide and protein misbehavior. *Proc. Natl. Acad. Sci.* **112**, 5267 – 5268 (2015).

[215] Horwitz, J. Alpha-crystallin. *Exp. Eye Res.* **76**, 145–153 (2003).

[216] Andley, U. P. Crystallins in the eye: Function and pathology. *Prog. Retin. Eye Res.* **26**, 78–98 (2007).

[217] Arrigo, A.-P. *et al.* Hsp27 (HspB1) and αB-crystallin (HspB5) as therapeutic targets. *FEBS Lett.* **581**, 3665–3674 (2007).

[218] Hochberg, G. K. A. & Benesch, J. L. P. Dynamical structure of αB-crystallin. *Prog. Biophys. Mol. Biol.* **115**, 11–20 (2014).

[219] Horwitz, J. The function of alpha-crystallin in vision. *Semin. Cell Dev. Biol.* **11**, 53–60 (2000).

[220] Liu, L., Ghosh, J. G., Clark, J. I. & Jiang, S. Studies of αB crystallin subunit dynamics by surface plasmon resonance. *Anal. Biochem.* **350**, 186–195 (2006).

[221] Jehle, S. *et al.* Solid-state NMR and SAXS studies provide a structural basis for the activation of αB-crystallin oligomers. *Nat. Struct. & Mol. Biol.* **17**, 1037–1042 (2010).

[222] Reddy, G. B., Das, K. P., Petrash, J. M. & Surewicz, W. K. Temperature-dependent chaperone activity and structural properties of human αA- and αB-crystallins. *J. Biol. Chem.* **275**, 4565–4570 (2000).

[223] Waudby, C. A. *et al.* The interaction of αB-Crystallin with mature α-Synuclein amyloid fibrils inhibits their elongation. *Biophys. J.* **98**, 843–851 (2010).

[224] Shammas, S. L. *et al.* Binding of the molecular chaperone αB-crystallin to Aβ amyloid fibrils inhibits fibril elongation. *Biophys. J.* **101**, 1681–1689 (2011).

[225] Knowles, T. P. J. *et al.* Kinetics and thermodynamics of amyloid formation from direct measurements of fluctuations in fibril mass. *Proc. Natl. Acad. Sci.* **104**, 10016 – 10021 (2007).

[226] O'Sullivan, C. K. & Guilbault, G. G. Commercial quartz crystal microbalances – theory and applications. *Biosens. Bioelectron.* **14**, 663–670 (1999).

[227] Stoy, J. *et al.* Insulin gene mutations as a cause of permanent neonatal diabetes. *Proc. Natl. Acad. Sci.* **104**, 15040–15044 (2007).

[228] Bell, G. I. *et al.* Nucleotide sequence of a cDNA clone encoding human preproinsulin. *Nature* **282**, 525–527 (1979).

[229] Bryant, C. *et al.* Acid stabilization of insulin. *Biochemistry* **32**, 8075–8082 (1993).

[230] Attri, A. K., Fernández, C. & Minton, A. P. pH-dependent self-association of zinc-free insulin characterized by concentration-gradient static light scattering. *Biophys. Chem.* **148**, 28–33 (2010).

[231] Li, S. & Leblanc, R. M. Aggregation of insulin at the interface. *J. Phys. Chem. B* **118**, 1181–1188 (2014).

[232] Ivanova, M. I., Sievers, S. A., Sawaya, M. R., Wall, J. S. & Eisenberg, D. Molecular basis for insulin fibril assembly. *Proc. Natl. Acad. Sci.* **106**, 18990 – 18995 (2009).

[233] Devlin, G. L. *et al.* The component polypeptide chains of bovine insulin nucleate or inhibit aggregation of the parent protein in a conformation-dependent manner. *J. Mol. Biol.* **360**, 497–509 (2006).

[234] Nielsen, L. *et al.* Effect of environmental factors on the kinetics of insulin fibril formation: elucidation of the molecular mechanism. *Biochemistry* **40**, 6036–6046 (2001).

[235] Sulatskaya, A. I. *et al.* Investigation of the kinetics of insulin amyloid fibrils formation. *Cell tissue biol.* **8**, 186–191 (2014).

[236] Smith, J. F., Knowles, T. P. J., Dobson, C. M., MacPhee, C. E. & Welland, M. E. Characterization of the nanoscale properties of individual amyloid fibrils. *Proc. Natl. Acad. Sci.* **103**, 15806 – 15811 (2006).

[237] Levin, A. *et al.* Elastic instability-mediated actuation by a supra-molecular polymer. *Nat. Phys.* **12**, 926–930 (2016).

[238] Knowles, T. P. J. *et al.* Observation of spatial propagation of amyloid assembly from single nuclei. *Proc. Natl. Acad. Sci.* **108**, 14746 – 14751 (2011).

[239] Morris, R. J. *et al.* Mechanistic and environmental control of the prevalence and lifetime of amyloid oligomers. *Nat. Commun.* **4**, 1891 (2013).

[240] Raman, B. *et al.* αB-crystallin, a small heat-shock protein, prevents the amyloid fibril growth of an amyloid β-peptide and β2-microglobulin. *Biochem. J.* **392**, 573–581 (2005).

[241] Rekas, A., Jankova, L., Thorn, D. C., Cappai, R. & Carver, J. A. Monitoring the prevention of amyloid fibril formation by α-crystallin. *FEBS J.* **274**, 6290–6304 (2007).

[242] Stevens, A. & Augusteyn, R. C. Acid-induced dissociation of alpha A- and alpha B-crystallin homopolymers. *Biophys. J.* **65**, 1648–1655 (1993).

[243] Grannis, G. F. The hydrolysis of insulin and human serum albumin in dilute hydrochloric acid. *Arch. Biochem. Biophys.* **91**, 255–265 (1960).

[244] Brange, J., Langkj\sgmaeligr, L., Havelund, S. & Vølund, A. Chemical stability of insulin. 1. Hydrolytic degradation during storage of pharmaceutical preparations. *Pharm. Res.* **9**, 715–726 (1992).

[245] Huebner, A. *et al.* Static microdroplet arrays: a microfluidic device for droplet trapping, incubation and release for enzymatic and cell-based assays. *Lab Chip* **9**, 692–698 (2009).

[246] Zhang, Y., Ishida, M., Kazoe, Y., Sato, Y. & Miki, N. Water-vapor permeability control of PDMS by the dispersion of collagen powder. *IEEJ Trans. Electr. Electron. Eng.* **4**, 442–449 (2009).

[247] Yerbury, J. J. *et al.* The extracellular chaperone clusterin influences amyloid formation and toxicity by interacting with prefibrillar structures. *FASEB J.* **21**, 2312–2322 (2007).

[248] Bumagina, Z., Gurvits, B., Artemova, N., Muranov, K. & Kurganov, B. Paradoxical acceleration of dithiothreitol-induced aggregation of insulin in the presence of a chaperone. *Int. J. Mol. Sci.* **11**, 4556–4579 (2010).

[249] Sonker, M., Sahore, V. & Woolley, A. T. Recent advances in microfluidic sample preparation and separation techniques for molecular biomarker analysis: A critical review. *Anal. Chim. Acta* **986**, 1–11 (2017).